



HAL
open science

Self-assembly into functional amyloids of *Aspergillus fumigatus* hydrophobins

Borja Rodriguez de Francisco

► **To cite this version:**

Borja Rodriguez de Francisco. Self-assembly into functional amyloids of *Aspergillus fumigatus* hydrophobins. Cell Behavior [q-bio.CB]. Sorbonne Université, 2019. English. NNT : 2019SORUS332 . tel-03139847

HAL Id: tel-03139847

<https://theses.hal.science/tel-03139847>

Submitted on 12 Feb 2021

HAL is a multi-disciplinary open access archive for the deposit and dissemination of scientific research documents, whether they are published or not. The documents may come from teaching and research institutions in France or abroad, or from public or private research centers.

L'archive ouverte pluridisciplinaire **HAL**, est destinée au dépôt et à la diffusion de documents scientifiques de niveau recherche, publiés ou non, émanant des établissements d'enseignement et de recherche français ou étrangers, des laboratoires publics ou privés.

Sorbonne Université

Institut Pasteur

Ecole Doctorale Complexité du vivant

Biological NMR Technological Platform

**Self-assembly into functional amyloids of *Aspergillus
fumigatus* hydrophobins**

Par **Borja Rodríguez de Francisco**

Thèse de Doctorat de Biochimie et Biologie Structurale

Dirigée par Dr. Iñaki Guijarro

Présentée et soutenue publiquement le 13 décembre 2019

Devant un jury composé de :

Bertrand Friguet
Cristina Sizon
André Matagne
Olivier Lequin
Thierry Fontaine
Iñaki Guijarro

Président
Rapporteur
Rapporteur
Examineur
Examineur
Directeur de thèse

Preface

This dissertation is submitted to the Ecole Doctorale Complexité du Vivant accredited by the Sorbonne University.

The work presented here has been carried out at the Institut Pasteur (CNRS UMR 3528), within the Biological NMR Technological Platform under the supervision of Dr. Iñaki Guijarro.

I was granted with a 3 years doctoral fellowship from the Institut Pasteur University International PhD Program (PPU). This program has received funding from the European Union's Horizon 2020 research and innovation program under the Marie Skłodowska-Curie grant agreement No. 665807. The last three months I was funded by the French National Research Agency (ANR FUNHYDRO ANR-16- CE110020-01) awarded to Dr. I. Guijarro. The work was funded by the ANR (ANR-16- sCE110020-01) and the 800 MHz NMR spectrometer used in this work was partially funded by the Région Ile de France (SESAME 2014 NMRCHR grant no 4014526).

Acknowledgments

This doctoral dissertation would not have been possible without the contribution of several people to whom I would like to express my appreciation to:

First of all, I would like to express my sincere gratitude to my supervisor Dr. Iñaki Guijarro for his continuous support during my PhD. His guidance and constant feed-back, not only professionally but also personally, made it possible for me to work on a challenging topic that was of great interest to me.

I am also very grateful to Dr. Isabel Valsecchi for always being concerned and providing me with her assistance through my project.

I would like to thank the Thesis Advisory Committee Members for their valuable assistance, insightful comments and encouragements.

I very much appreciated the Structural Bioinformatics Unit and Biological NMR platform for always willing to help me. Many thanks to Dr. Muriel Delepierre and Dr. Michael Nilges for their generous support working in their Units. Furthermore, I would like to thank Dr. Bruno Vitorge for his support and technical help, Dr. Aracelys López Castilla for her valuable comments, Dr. Nadia Izadi-Pruneyre who profoundly believes in my abilities, and all the office members, Dr. Sebastian Brier, Dr. Florence Cordier, Dr. Catherine Simenel, Dr. Benjamin Bardiaux and all students in the group who have been a big support during this time.

I would like to recognize the help that I received from Dr. Gérard Péhau-Arnaudet for his assistance during the electron microscopy experiments.

Also, I sincerely acknowledge my collaborators Dr. Antoine Loquet, Dr. Vincent Duprès, Dr. Frank Lafont, Dr. Vishu Amanianda Dr. Anne Beauvais and Dr. Jean-Paul Latgé for their constructive suggestions. Sven van Teeffelen for allowing me to use their instruments. Also, I would like to extend my sincere thanks to Dr. Margaret Sunde and Dr. Chi L.L. Pham for their invaluable contributions and experience to our collaborative work.

Besides, I would like to thank my friends in Institute Pasteur, for always making me feel very welcome. To the PPU family, it was a pleasure coming to work every day with you there. I would also like to extend my deepest gratitude to the STAPA association and members, my personal growth would not have been possible without the support of this fantastic team, and to every friend that has been close during these years in good and bad times.

Finally, I am indebted to all my family and friends, for their unconditional love and concern and for putting your faith on me and urging me to do better. To my mum, for her advice, love and care. To my dad, for his support in every decision I made and being a model for me. To my sister, for always being concerned, and to all my friends in Madrid, Grajal de Campos and abroad, for having incited me to achieved my goals.

I have no valuable words to express my thanks. I am extremely grateful to every person that made my PhD stage one of the best periods of my personal and professional career.

Résumé

Les hydrophobines sont des protéines fongiques qui s'assemblent aux interfaces hydrophobes/hydrophiles ou air-eau (IHH) pour former des fibres amyloïdes fonctionnelles qui s'organisent en couches dont le caractère amphiphile détermine leurs fonctions. Les spores du champignon pathogène opportuniste *Aspergillus fumigatus* sont couvertes d'une couche de bâtonnets constitués de fibres amyloïdes formés par l'hydrophobine RodA. Ce revêtement hydrophobe facilite la dispersion des spores et les rend inertes vis à vis du système immunitaire humain. Deux proches homologues de RodA, RodB et RodC, sont aussi présents dans la paroi cellulaire des spores. Nous avons réalisé une étude comparative de l'auto-assemblage de ces trois protéines avec un accent particulier sur RodC. Nous avons montré que RodA-C nécessitent d'une interface IHH pour s'assembler en fibres et mis en évidence l'importance de la nature de l'interface dans la morphologie de leurs assemblages. Nous avons observé une auto-inhibition de la fibrillation avec la concentration et montré que celle-ci est due à la saturation de l'interface air-eau. En étudiant l'effet de mutations ponctuelles sur les cinétiques de fibrillation de RodC, nous avons établi des similitudes et des différences par rapport aux régions importantes pour la formation de fibres pour RodC et RodA, étudiée au préalable. La transition du monomère à l'état amyloïde est accompagnée d'une perte de régions désordonnées et un gain de feuillets β intermoléculaires en accord avec les analyses par mutagenèse dirigée, qui indiquent que des résidus hydrophobes dans des régions flexibles du monomère sont impliqués dans le squelette β -croisé des fibres.

Mots clés: amyloïdes fonctionnels, hydrophobine, bâtonnets, *Aspergillus fumigatus*, assemblage de protéines, biophysique.

Abstract

Hydrophobins are fungal proteins that spontaneously self-assemble at hydrophobic/hydrophilic or air/water interfaces to form functional amyloids that associate laterally into layers. The amphiphilic character of these layers is at the origin of the hydrophobin biological roles. The spores of the airborne fungal pathogen *Aspergillus fumigatus* are covered by an amyloid layer with rodlet morphology made up by the RodA hydrophobin. This hydrophobic coat facilitates air-dispersal of the spores and renders these inert relative to the human immune system. Two close homologs of RodA, named RodB and RodC, are also present in the spore cell wall. We have performed a comparative study on the self-assembly of the three proteins with particular emphasis on RodC. We have shown that RodA-C require an interface to form amyloids and revealed the importance of the nature of the interface in determining the morphology of hydrophobin assemblies. We have observed that the fibrillation of RodA-C is auto-inhibited (slower at higher concentrations) and shown that this phenomenon can be explained by saturation of the air-water interface. The analysis of the effect of single point mutations on the fibrillation kinetics of RodC revealed the regions that are important for fiber formation, which showed differences and similarities relative to the previously studied RodA. The transition from monomers to amyloids is accompanied by a loss of unordered regions and a gain in intermolecular β -sheets, in agreement with the mutational analyses of RodA and RodC that indicated that hydrophobic residues in flexible loops are involved in the cross- β core of the fibers.

Keywords: functional amyloid, hydrophobin, rodlet, *Aspergillus fumigatus*, protein assembly, biophysics.

Table of contents

Preface	i
Acknowledgments	ii
Résumé	iv
Abstract	v
Table of contents	vi
Index of figures	ix
Index of tables	xii
Abbreviations	xiii
1 Introduction	15
1.1 Overview	15
1.2 The Fungal Kingdom	16
1.3 Fungal diseases in humans	17
1.4 Aspergillosis.....	18
1.5 <i>Aspergillus fumigatus</i>	19
1.5.1 Biology.....	20
1.5.2 Fungal Cell Wall	21
1.5.3 <i>Aspergillus fumigatus</i> Cell Wall	22
1.6 Pathobiology.....	24

1.7	Amyloid fibers.....	25
1.7.1	Functional and non-functional amyloids	29
1.7.2	How does the amyloid state form?.....	31
1.8	Hydrophobins	34
1.8.1	General aspects	34
1.8.2	Biological functions	39
1.8.3	Applications	40
1.8.4	<i>Aspergillus fumigatus</i> hydrophobins.....	40
1.9	Project description.....	45
2	Materials & Methods	47
2.1	Proteins and peptides studied	47
2.2	Plasmid design.....	48
2.3	Expression and purification.....	49
2.4	Solution nuclear magnetic resonance spectroscopy	50
2.4.1	Assignment principle	50
2.4.2	Assignment of NMR backbone chemical shifts of RodC.....	54
2.4.3	Secondary structure calculation	54
2.5	Amyloid formation followed by ThT fluorescence.....	55
2.5.1	Effect of RodC point mutations on the fibrillation process	56
2.5.2	Effects of cell wall components on amyloid formation	57
2.6	Synchrotron radiation circular dichroism spectroscopy of hydrophobins	58

2.7	Fourier-transform infrared spectroscopy.....	58
2.8	Transmission electron microscopy.....	60
2.9	Atomic force microscopy.....	60
3	Results & Discussion	62
3.1	Chapter 1: Manuscript. Probing structural changes during self-assembly of surface-active hydrophobin proteins that form functional amyloids in fungi.....	62
3.1.1	Introduction.....	62
3.1.2	Framework and objective.....	62
	Manuscript.....	62
3.2	Chapter 2: Hydrophobin self-assembly.....	90
3.2.1	Introduction.....	90
3.2.2	<i>A. fumigatus</i> Class I hydrophobins form <i>bona fide</i> amyloids.....	90
3.2.3	Solution and ssNMR.....	94
3.2.4	Self-assembly kinetics of Rod hydrophobins	99
3.2.5	Effects of major fungal cell wall components on RodC self-assembly.....	124
4	Conclusions & perspectives.....	128
5	Bibliography	132

Index of figures

Fig. 1. <i>Aspergillus</i> morphology.	19
Fig. 2. <i>A. fumigatus</i> life cycle.	20
Fig. 3. Image of different fungal cell walls (extracted from Gow, Latgé, & Munro, 2017). ..	22
Fig. 4. <i>A. fumigatus</i> conidia.	24
Fig. 5. Amyloid fiber features.....	26
Fig. 6. Examples of high-resolution structures of amyloid fibers from the PDB database.	27
Fig. 7. Amyloid morphology and structure diagram.	28
Fig. 8. Examples of stacked β -strands.	29
Fig. 9. Comparison of the secondary structure of the globular (native) and amyloid forms of an all- β protein.....	31
Fig. 10. Protein aggregation landscapes. Adapted from Landreh <i>et al.</i> , 2016.....	32
Fig. 11. Amyloid fibril formation kinetics plot.	32
Fig. 12. Microscopic processes underlying amyloid formation.	33
Fig. 13. Hydrophobin pattern of cysteines.....	35
Fig. 14. Alignment of Class I and Class II of some commonly studied hydrophobins.	35
Fig. 15. Rodlets images seeing under AFM.	36
Fig. 16. Class I and Class II hydrophobins cartoon and surface representations showing the structure and electrostatic potential, respectively.	37
Fig. 17. Proposed simple model of <i>in vitro</i> Class I hydrophobin aggregation.	38
Fig. 18. RodA-C sequence and hydropathy profiles comparison.	41
Fig. 19. Alignment of <i>A. fumigatus</i> hydrophobins.	42
Fig. 20. RodA solution structure.....	44
Fig. 21. RodC sequence.	48
Fig. 22. Fusion protein design for hydrophobin production.....	48

Fig. 23. HSQC experiment.	51
Fig. 24. Complementary pairs of triple resonance experiments for backbone assignment.	52
Fig. 25. Example of contiguous spin systems assignment with a set of two complementary sequences.	53
Fig. 26. Amyloid formation followed by ThT fluorescence.....	56
Fig. 27. RodC sequence with the single point mutations.	57
Fig. 28. Fourier-transform infrared spectroscopy example spectrum.....	59
Fig. 29. AFM of RodA-C self-assemblies.	91
Fig. 30. Negative stain TEM of RodA-C self-assemblies.	92
Fig. 31. RodA-C XR fiber diffraction	93
Fig. 32. ^1H - ^{15}N HSQC spectra of RodA (25 °C), RodB (25 °C) and a SOFAST experiment for RodC (45 °C).	95
Fig. 33. RCI as a function of residue number.....	96
Fig. 34. Carbon CP-MAS (left) and INEPT (right) experiments of RodA, RodB and RodC.	97
Fig. 35. Carbon-carbon PDSM spectra of RodA-C amyloids.....	98
Fig. 36. RodA-C amyloid formation monitored by ThT fluorescence kinetics.....	100
Fig. 37. Lag phase time and half-time of amyloid fibril formation.....	100
Fig. 38. TEM of RodA- and RodC-monomer samples.....	102
Fig. 39. Influence of an AWI on RodA-C fiber formation.....	103
Fig. 40. RodC fiber formation kinetics at different protein concentrations.....	104
Fig. 41. RodC fiber formation kinetics experiments at 40 °C.	107
Fig. 42. RodA-C fibrillation kinetics under native and reducing conditions.....	108
Fig. 43. Concentration dependence of RodC fibrillation kinetics under reducing conditions.....	109
Fig. 44. Concentration dependence of RodC fibrillation under reducing conditions.....	110

Fig. 45. Comparison of the kinetics of reduced RodC in the presence or absence of an AWI.....	111
Fig. 46. RodC single-point mutations' position.....	112
Fig. 47. RodC single-point mutants' purity and foldedness.....	114
Fig. 48. RodC single-point mutant self-assembly kinetics – Comparison.	115
Fig. 49. RodC single-point mutant self-assembly kinetics – Individual kinetic traces	117
Fig. 50. RodC single-point mutant self-assembly kinetics – Lag phase.....	118
Fig. 51. RodC single-point mutant self-assembly kinetics – Growth phase half-time.	118
Fig. 52. RodC single-point mutants' kinetics – Lag phase and secondary structure.....	120
Fig. 53. RodC quadruple point mutants' SOFAST- ¹⁵ N HMQC experiments.	121
Fig. 54. RodC quadruple-point mutant self-assembly kinetics.....	122
Fig. 55. RodC-derived peptides seen by TEM.	123
Fig. 56. Effect of different major fungal cell wall components on the lag phase of RodC fibrillation kinetics.....	126
Fig. 57. RodC fibrillation kinetics in the presence of increasing concentrations of melanin.....	127

Index of tables

Table 1. Most common fungal diseases	18
Table 2. Examples of functional amyloids that can be found in nature.	31
Table 3. Rod hydrophobins.	47
Table 4. RodC point mutants and peptides.	47

Abbreviations

AFM	Atomic force microscopy
AIDS	Acquired Immunodeficiency Syndrome
ATR	Attenuated total reflection
AWI	Air-water interface
CP-MAS	Cross polarization – magic angle spinning experiment
DSS	Sodium salt of 4,4-dimethyl-4-silapentane-1-sulfonic acid
DTT	Dithiothreitol
ECM	Extracellular matrix
FT-IR	Fourier-transform infrared spectroscopy
HHI	Hydrophilic:hydrophobic interface
HOPG	Highly Ordered Pyrolytic Graphite
HMQC	Heteronuclear multiple quantum correlation
HSQC	Heteronuclear Single Quantum Coherence
IA	Invasive pulmonary aspergillosis
INEPT	Insensitive nuclei enhanced by polarization transfer
IPTG	Isopropyl β -D-1-thiogalactopyranoside
LB	Luria-Bertani broth
MCW	Major cell wall
NMR:	Nuclear magnetic resonance
PAMPs	Pathogen-associated molecular patterns
PDS	Proton-driven spin diffusion
RCI	Random coil index
SOFAST	band-selective optimized flip-angle short-transient experiment
SRCD	Synchrotron radiation circular dichroism
TEM	Transmission electron microscopy
TFA	Trifluoroacetic acid
ThT	Thioflavin T
ssNMR	Solid-state NMR

WT	Wild-type
XR	X-ray

Introduction

1 Introduction

1.1 Overview

Amyloids are defined as proteinaceous fibers that share a skeleton with the so-called cross- β structure. Since their first description by Virchow in 1854 (Sipe and Cohen, 2000) on abnormal brain tissues, amyloid fibers have been linked to disease. Indeed, over 60 pathologies associated to proteins that irreversibly misfold into an amyloid form have been described (Chiti & Dobson, 2017). However, in the late 90s, a number of proteins that are not associated to any disease, were shown to form amyloids under appropriate (Gujarro *et al.*, 1998; Chiti *et al.*, 1999), indicating that the amyloid structure was not restricted to some disease-related proteins. These findings ultimately lead to the generic amyloid hypothesis (Dobson, 1999; Stefani and Dobson, 2003) and to the recognition that protein sequences have in general evolved to avoid this self-propagating fold. Concomitantly, however, in the 90s, proteins that adopt an amyloid structure to perform their function were discovered (Fowler *et al.*, 2005; Maji *et al.*, 2009; Otzen and Riek, 2019). Nowadays, it is clear that many proteins have evolved to fold into amyloids to perform their biological function.

My PhD work was devoted to characterize the assembly of one of the first examples of functional amyloids, namely fungal proteins from the hydrophobin family, and in particular hydrophobins produced by the opportunistic pathogen *A. fumigatus*.

In this introduction, I will first present general aspects of the fungal kingdom, such as its diversity, ecological and biotechnological importance, as well as the impact of fungi in public health, particularly focusing on aspergillosis. Then, I will address, in more detail, the biology and pathobiology of *A. fumigatus* and describe the cell wall organelle, which is of utmost importance for pathogen-host interactions. The outer layer of the cell wall of *A. fumigatus* spores consists of amyloid fibers formed by a hydrophobin protein called RodA. This layer is at the forefront of the interactions of the spores with their environment.

I will then describe hydrophobins, small fungal proteins unique to filamentous fungi. These proteins show remarkable physicochemical properties upon which rely their biological functions and possible biotechnological applications. Hydrophobins spontaneously auto-associate at air-water (AWI) or hydrophobic-hydrophilic interfaces (HHI) to form amphipathic layers. I will expose what it is known about the monomeric soluble form, the mechanism of

INTRODUCTION

auto-association and the structure of the assemblies. Finally, I will focus on *A. fumigatus* hydrophobins and introduce the objectives and questions that we posed during this work on their mechanism of self-assembly and structure.

1.2 The Fungal Kingdom

The Fungal Kingdom is one of the largest and more diverse group of organisms on Earth. Last estimates suggest that there are between 2.2 and 3.8 million species, and only the 8% is named (Hawksworth and Lücking, 2017). Fungi appeared on Earth more than 890 million years ago and have colonized almost every part of the globe. Fungi can indeed live in aquatic or terrestrial environments and play important roles in diverse ecosystems. These organisms have evolved into three major ecological roles: saprobes, mutualistic symbionts and parasites. As saprobes, fungi are the main decomposers of the complex components of plant debris, e.g. cellulose and lignin, and some animal debris, e.g. chitin and keratin, thus being important players in the carbon and nitrogen cycles. Fungi are also very important in mutualistic symbioses with plants (mycorrhizae) and algae (lichens) where fungi exchange nitrogen, phosphorus and minerals for carbohydrates or aminoacids from the photobiont. Finally, fungi are important pathogens with an important ecological function clearing unfit individuals and favoring evolution (Kendrick, 2001; Harrison, 2005).

In addition, fungi have many applications. Since ancient times, humans have made wine or beer with yeasts, leavened bread or collected edible mushrooms. Nowadays, fungi are a very important source of antibiotics and enzymes used in biotechnology. To give but one example, the antibiotic penicillin, produced by *Penicillium* spp, discovered by Alexander Fleming almost one hundred years ago, has saved hundreds millions of lives (Gaynes, 2017).

However, fungi can also be harmful to other living organisms. Fungi can be plant pathogens, for example, *Magnaporthe oryzae* causes the most destructive disease on rice worldwide, while *Fusarium graminearum* infects all cereal species and *Ustilago maydis* is the major corn parasite (Dean *et al.*, 2012). Animals can also suffer from fungal infections; *Batrachochytrium dendrobatidis*, that causes chytridiomycosis in amphibians, is responsible of a mass amphibian extinction and decline worldwide (Scheele *et al.*, 2019). In humans, recent estimates indicate that every year fungi affect more than a billion people, of which 11.5 million suffer from life-threatening infections and more than 1.5 million die (Tudela and Denning, 2017). Together, the three major fungal pathogens, namely *Candida albicans*, *Cryptococcus neoformans* and *A.*

INTRODUCTION

fumigatus, kill as many people as the major infectious disease (tuberculosis, 1.5-1.7 million) and more than HIV (770 000) or malaria (430 000; WHO, Global Health Observatory, 2018 data).

1.3 Fungal diseases in humans

There is a broad range of fungi (> 600) infecting humans causing diseases that can be from mild to lethal. Mycosis can affect the skin, nails, hair, the eyes, mucosas, lungs, and can develop into systemic diseases. Severe fungal infections are due to opportunistic pathogens that infect immunosuppressed people and are most of the time associated to other diseases or medical conditions such as asthma, leukemia, organ transplants, AIDS or immunosuppressive corticosteroid therapies. Despite the number of deaths and the increase in severe mycosis, fungal infections remain neglected by public health authorities (Bongomin *et al.*, 2017).

The table below summarizes the most important fungal infections (Table 1).

Most common fungal diseases	
Fungal nail infections	Caused by many different environmental species of fungi (yeasts or molds). Easy to cure with common antimycotics.
Dermatophytosis	Fungal infection of the skin caused by <i>Trichophyton</i> , <i>Microsporum</i> or <i>Epidermophyton</i> spp. Very common and not very dangerous for the patient. Easy to cure with common antimycotics.
Vaginal candidiasis	Caused by the yeast <i>Candida</i> that normally lives inside the body but can cause an opportunistic vaginal infection. In the United States, it is the second most common type of vaginal infection after bacterial vaginosis.
Fungal diseases that affect people who live in or travel to certain areas	
Blastomycosis	Caused by <i>Blastomyces</i> spp. Originated in North America. Symptoms are very similar to those of flu. Most people will need treatment with antifungal medication.
Coccidioidomycosis or Valley fever	Caused by <i>Coccidioides</i> spp. Endemic in North America. People who get sick will get better on their own within weeks to months but some people will need antifungal medication.
Cryptococcosis by <i>Cryptococcus gattii</i>	Happens in tropical and sub-tropical regions and can produce a severe lung infection that will need antifungal medication treatment.
Histoplasmosis	<i>Histoplasma</i> is the infectious agent and it is worldwide, very severe and will need antifungal medication for months.

INTRODUCTION

Paracoccidioidomycosis	Usually happens in rural areas with the presence of <i>Paracoccidioides</i> spp. It can be treated with azole antifungals.
Fungal diseases that affect people with weakened immune systems	
Aspergillosis	Worldwide mycosis caused by <i>Aspergillus</i> spp. People with weakened immune system or lung diseases are at a higher risk of developing fatal health problems.
Invasive candidiasis	Serious infection caused by <i>Candida</i> spp. that affects the blood, heart, brain, eyes, bones, or other parts of the body.
Cryptococcosis	Strong disease provoked by <i>Cryptococcus neoformans</i> . It affects the lungs or the central nervous system and can lead to cryptococcal meningitis.
Mucormycosis	Caused by different mucormycetes, mainly affects people with weakened immune systems. It is not a life-threatening disease but needs antifungal medication.
<i>Pneumocystis pneumonia</i>	Caused by the fungus <i>Pneumocystis jirovecii</i> . It was very important in the late 1980s when around 75% of people living with AIDS developed this type of pneumonia.
Sporotrichosis	Caused by the fungus <i>Sporothrix</i> spp. It can be cutaneous, pulmonary or disseminated. These infections are not life-threatening but must be treated with prescription of antifungal medication for several months.

Table 1. Most common fungal diseases

Adapted from the Center for Disease Control and Prevention (CDC) (accessed June 4, 2019) and (Fausto, Rodrigues and Coelho, 2019).

1.4 Aspergillosis

Aspergillosis are diseases caused by species belonging to the genus *Aspergillus*. This genus comprises more than 300 species but only 20 of them are pathogenic to humans. Among them, *A. fumigatus* is the most important species, it causes approximately 90% of the aspergillosis cases (Latgé, 1999; Margalit and Kavanagh, 2015), followed by *A. flavus*, *A. niger* and *A. terreus* (Cadena, Thompson and Patterson, 2016).

A. fumigatus is a major airborne fungal pathogen that infects the lungs. The spectrum of aspergillosis is very broad and comprises several clinical entities: allergic bronchopulmonary aspergillosis, chronic pulmonary aspergillosis syndromes and invasive pulmonary aspergillosis (IA) (Cadena, Thompson and Patterson, 2016).

Recent estimates indicate that more than 250 000 people die every year from of invasive aspergillosis and that 5 million people suffer from allergic bronchopulmonary aspergillosis

INTRODUCTION

(Bongomin *et al.*, 2017). However, the difficulties in diagnosis suggest that these numbers could be under estimated by a factor of two. In the case of invasive aspergillosis, the mortality ratio varies between 30 and 95%. It is related to the degree of immunosuppression, the geographic region, socioeconomic conditions and cultural habits (Brown *et al.*, 2012; Krappmann, 2016). In the absence of treatment with antifungal drugs, the mortality rate can be 100%.

1.5 *Aspergillus fumigatus*

Aspergillus spp. are filamentous fungi that belong to the *phylum* Ascomycota, characterized by the production of sexual spores inside closed compartments called asci. *Aspergillus* spp., like many other filamentous fungi spend most, if not all of their life, in an asexual form and reproduce through asexual spores called conidia held on aerial structures called conidiophores.

The name *Aspergillus* was coined in 1729 by Pier Antonio Micheli to describe the asexual form of the conidiophores that resembled an aspergillum (Fig. 1), a liturgical device used to sprinkle holy water.

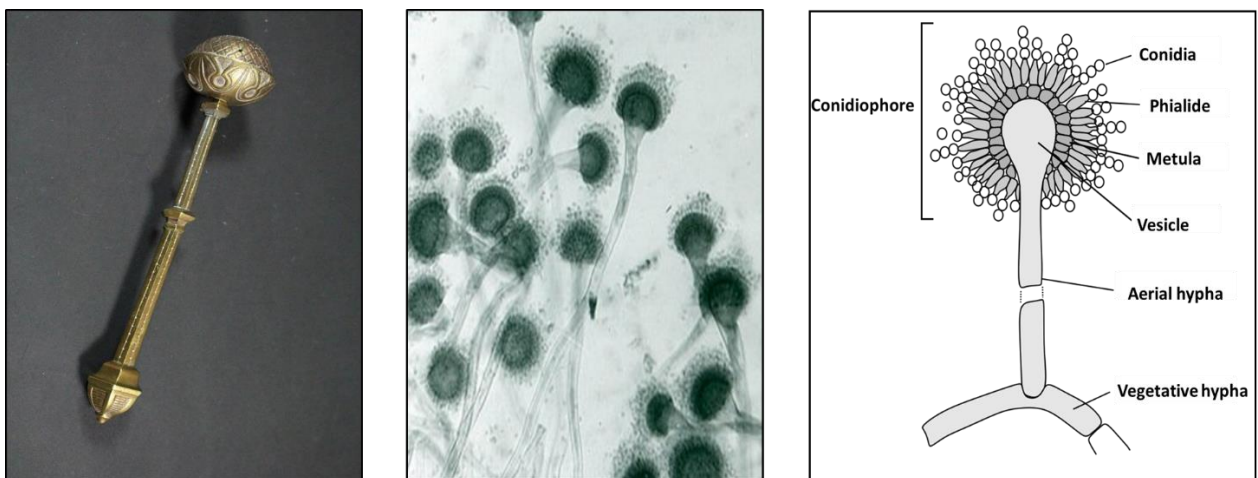


Fig. 1. *Aspergillus* morphology.

Left: Aspergillum (source Wikipedia). Middle, *Aspergillus* sp. (source: CDC's webpage) and right, *Aspergillus* sp. morphological diagram (adapted from Pinterest). Conidia are located on the conidiophore and are held by specialized cells called phialides.

The genus *Aspergillus* contains ~350 species, of which around 20 species are pathogenic. Among these, *A. fumigatus* causes approximately 90% of the aspergillosis cases (Latgé, 1999; Margalit and Kavanagh, 2015).

INTRODUCTION

1.5.1 Biology

A. fumigatus is a thermotolerant and saprophytic fungus that lives in the soil worldwide playing an important role in the carbon and nitrogen cycle (Willger, Grahl and Cramer, 2009). This species lives in its asexual form during the whole life cycle (Fig. 2).

This mold thrives in moist substrates where it sporulates abundantly leading to high concentration of its conidia in air (*ca.* 1-100 conidia/m³): it has been estimated that on average, an adult inhales more than 100 conidia per day. The conidia globular form, small size < 3 μm and hydrophobicity, allow them to efficiently disperse in the air and reach lung alveoli (> 10 μm) (Kwon-Chung and Sugui, 2013).

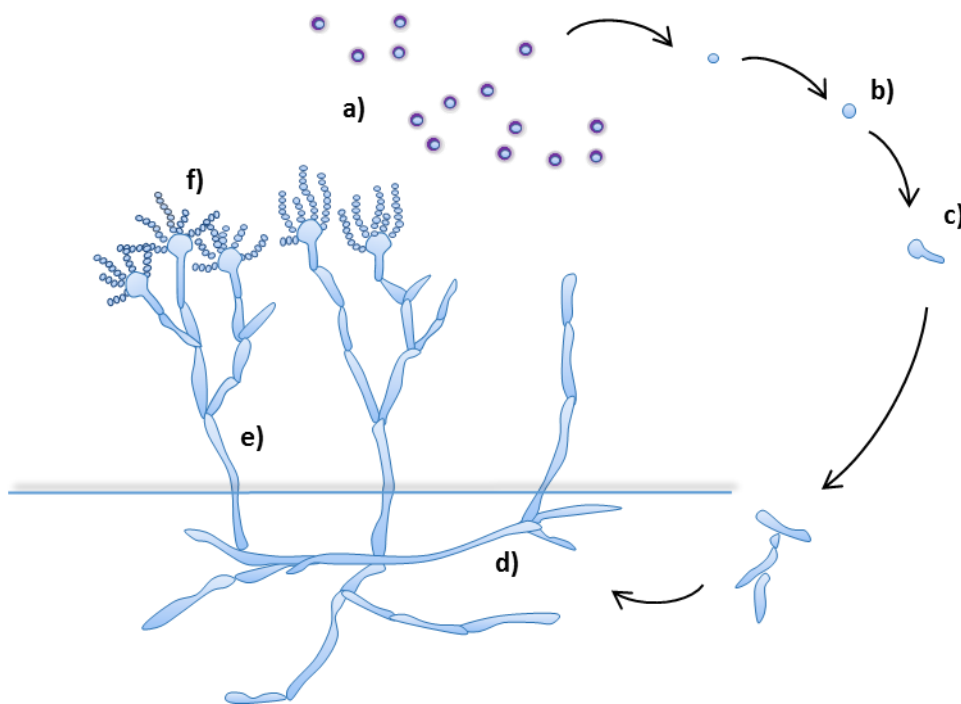


Fig. 2. *A. fumigatus* life cycle.

a) Asexual hydrophobic spores (conidia) are dispersed by the air, **b)** when dormant conidia find a convenient place to grow, these swallow, the metabolism is activated and conidia germinate. **c)** Germinating conidia. **d)** Development of the mycelia formed by the fungal cells (called hyphae). **e)** Cells emerge from the substrate to form aerial hyphae and the reproductive structures (conidiophores). **f)** The conidiophores contain substructures named phialides, from which the new dormant conidia emerge *via* evagination, closing the life cycle.

1.5.2 Fungal Cell Wall

In contrast with animal cells, fungal cells are enveloped by a thick cell wall that endows extraordinary properties to the hyphae and spores. The fungal cell wall is indeed an essential dynamic organelle that can change its composition and structure depending on environmental conditions and the life cycle. It is the interface between the fungus and its environment, including possible interactions with their hosts. It is an armor that protects fungi against chemical or physical stress. Its strength and rigidity allows fungi to resist to turgor pressures as high as 20 times the atmospheric pressure (Money, 2001) and penetrate solid substrates or host cells, as well as to grow and differentiate into complex shapes.

Although the fungal cell wall is a complex organelle that changes overtime and between species, most fungal cell walls have a common core of covalently branched β -(1,3)-glucan and chitin [β -(1,4) N-acetylglucosamine]. These polysaccharides form a scaffold that surrounds the cell. In many species, β -(1,6)-glucan is branched to β -(1,3)-glucan. The rest of the cell wall carbohydrate composition and the nature of the carbohydrates attached to the core can be quite different between fungal species as can be observed in Fig. 3, which shows some examples of cell wall from different fungal pathogens. (Gow, Latgé and Munro, 2017).

In addition to the different polysaccharides, that normally comprise 90% of the cell wall mass, the fungal cell wall contains enzymes specialized in carbohydrate synthesis and remodeling. Chitin and glucan synthases are embedded in membrane while the remodeling enzymes, such as glycohydrolases, glycosidases or transglycosidases are anchored to the plasma membrane through a GPI-anchor (glycosyl-phosphatidyl inositol).

INTRODUCTION

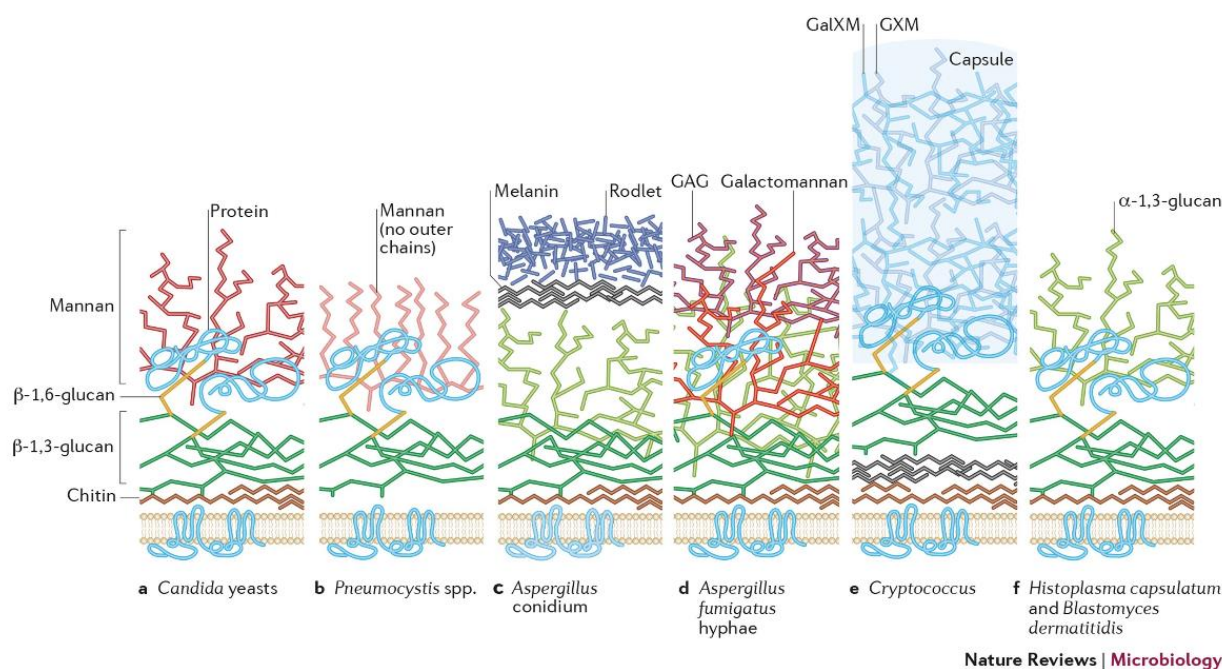


Fig. 3. Image of different fungal cell walls (extracted from Gow, Latgé, & Munro, 2017).

1.5.3 *Aspergillus fumigatus* Cell Wall

The hyphal and conidial morphotypes display different structural organizations based on the same fibrillar core. Most of what is known on the composition of *A. fumigatus* cell wall comes from the chemical and enzymatic analysis of extracted material of wild type and mutant strains from the laboratory of J. -P. Latgé at the Institut Pasteur. The extracted material is fractionated into alkali soluble and alkali insoluble fractions. The fibrillar core is alkali-insoluble and is composed of β -(1,6) branched β -(1,3)-glucan (4% branching) cross-linked to chitin through β -(1,4) bonds. Chitosan, β -(1,3)/ β -(1,4)-glucan and β -(1,5)-galacto- α -(1-2)- and α -(1-6)-mannan are covalently bound to branched β -(1,3)-glucan. The alkali-soluble fraction is amorphous and mainly composed of linear chains of α -(1-3)-glucan with intra-chains of α -(1-4)-glucan linked to glucose units (Latgé and Beauvais, 2014).

Relative to conidia, hyphae contain two additional polysaccharides: galactomannan (GA) and galactosaminogalactan (GAG). GA, which is used as biomarker for the detection of invasive aspergillosis, is composed of a main chain of α -mannoside and short side-chains of galactofuranose residues (Fontaine, 2017). GAG is a heteropolysaccharide composed of α -(1,4) linked galactose and N-acetylgalactosamine. Because of its importance in virulence and pathogenesis, GAG is considered nowadays as a potential novel drug target (Speth *et al.*, 2019).

INTRODUCTION

Although absent in wild-type conidia, it has recently been established by Valsecchi *et al.*, 2019a that GA and GAG can appear in conidia as a result of remodeling when key-polysaccharide synthases are mutated.

Because conidia are the infectious form of the mold, they have attracted much interest for many years (Carrion *et al.*, 2013; Margalit and Kavanagh, 2015; Croft *et al.*, 2016; Latgé, 2017). In addition to GA and GAG, the main difference between hyphae and conidial cell walls is the presence of a layer of the black pigment melanin that is covered by an outer hydrophobic proteinaceous layer with rodlet morphology. Both the melanin and the rodlet layers disappear upon swelling and germination.

The melanin layer protects the fungus against UV radiation, reactive oxygen species and inhibits host-cell phagocytosis, cytokine production and apoptosis (Langfelder *et al.*, 2003). *A. fumigatus* melanin is of the “DHN” type, formed from 1,8-dihydroxynaphthalene (DHN), which is synthesized from the precursors acetyl-coA or malonyl-coA. Although the intracellular synthesis pathway of DHN is known, its polymerization and oxidation to form melanin, as well as melanin structure and degradation, are still poorly understood (Eisenman and Casadevall, 2012).

The rodlet layer, which covers the conidial surface, confers hydrophobicity to the conidia, thus facilitating dispersion and rendering conidia waterproof. Besides, it protects conidia from desiccation.

It is made up of the RodA protein (UniProtKB accession number B0Y4B10 and *A. fumigatus* Genome Database number AFUA_5G09580) that belongs to the hydrophobin family. This protein self-assembles into amyloids fibers with a characteristic rodlet morphology (Fig. 4). Moreover, this rodlet layer masks the pathogen-associated molecular patterns rendering the conidia inert relative to the immune system (Aimanianda *et al.*, 2009). Indeed, while the conidia covered with RodA rodlets do not trigger any response from the innate and adaptive immune systems, conidia lacking this mask (deletion mutants of the *rodA* gene, germinating conidia or conidia treated with concentrated acids to extract RodA) do elicit a response.

INTRODUCTION

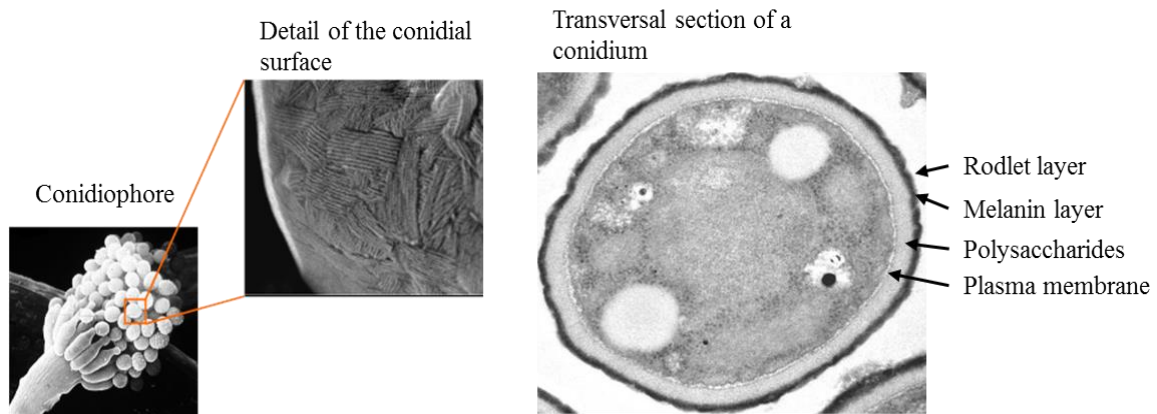


Fig. 4. *A. fumigatus* conidia.

Left, *A. fumigatus* conidiophore and SEM (scanning electron micrograph) detail of the conidial surface. Right, transversal section of a conidia TEM micrograph (credits: *Aspergillus* Unit).

1.6 Pathobiology

The airborne conidia are the infectious form of the mold. Although the majority of conidia are expelled mechanically by the mucociliary transport some conidia bypass the mucociliary clearance and penetrate the lung alveoli (Krappmann, 2016). Conidia attach to the extracellular matrix on the surface of the airway epithelial cells (either at bronchial or alveolar level) of the lower respiratory tract, in a process that is not very well understood. During the process, the rodlet and melanin layers hide the immunogenic cell wall polysaccharides avoiding an inflammatory response. The interaction between the conidium and the lung cells results in clearance by healthy individuals whereas in susceptible people it results in infection. In immunocompetent host, clearance of inhaled conidia is highly coordinated by the immune response that eliminates pathogens while preventing inflammatory lung damage. Intracellular swelling leading to germination, which occurs in macrophage phagosomes, is concomitant to the removal of the rodlet layer and the emergence of cell wall pathogen-associated molecular patterns (PAMPs), including β -glucans and other immunostimulatory polysaccharides and subsequent activation of Dectin-1 and other C-type lectin receptor's signaling pathways. These signaling pathways trigger an adaptive immune response that normally ends up in fungal killing (Brown, 2006; Latgé, Beauvais and Chamilos, 2017). In contrast, in immunocompromised individuals, *A. fumigatus* evades the debilitated immune system, conidia swell and germinate in the macrophages' phagosomes leading to a colonization of the lung parenchyma (Croft *et al.*, 2016).

INTRODUCTION

As mentioned before, in addition to its biological role, the RodA amyloid rodlet layer provides immune inertness to the spores of *A. fumigatus*. This functional amyloid coat mediates initial host-fungal interactions and protects the spores from the innate immune system. Nevertheless, the RodA coat is not a virulence factor. Although RodA reduces killing by macrophages and helps the fungus to resist against NETosis (neutrophil extracellular traps), its removal does not influence pathogenicity (Thau *et al.*, 1994; Paris *et al.*, 2003). Spores from other fungal species within the *phylum* Ascomycota are covered with an amyloid rodlet layer as well. It has been shown that the hydrophobin coat is also immunologically inert for other pathogenic (*A. flavus*), allergenic (*Cladosporium cladosporioides*), edible (*P. camemberti*) or toxic fungi (*P. verrucosum*). Although the amyloid coat might present an advantage for pathogenic fungi infection, it has also beneficial effects for humans by hiding the allergenic components of the cell wall and preventing allergies and asthma (Bayry *et al.*, 2014). The immune inertness of this functional amyloids contrasts with the observation that amyloids from several disease-related proteins are immunogenic and induce inflammatory responses and the hypothesis that the cross- β structure triggers the inflammatory response (Gustot *et al.*, 2015).

1.7 Amyloid fibers

Amyloid fibers are formed by soluble proteins that self-assemble into insoluble aggregates that are resistant to disaggregation and rich in β -structure.

The name “amyloids” was coined by Virchow in 1854 to describe some deposits that appeared in brain tissue and could be stained with iodine and sulphuric acid. The staining properties of the deposits were starch-like and he inferred that these consisted of carbohydrates. Some years later, in 1859, Friedrich and Kekulé, from the high nitrogen contained in liver tissue infiltrated with amyloids, suggested that the deposits were made of proteins (Friedreich and Kekulé, 1859; Sipe, 1992). Over a century later, Glenner and Eanes discovered that amyloid fibers exhibited an X-ray (XR) diffraction signature (Fig. 5) known as the “cross- β arrangement” (Eanes and Glenner, 1968). Today, a protein is considered to be in an amyloid state when it forms long fibers with the cross- β structure. Amyloids can be revealed using reporter dyes such as Congo red or thioflavin T (ThT) (Chiti and Dobson, 2006; Eisenberg and Jucker, 2012).

INTRODUCTION

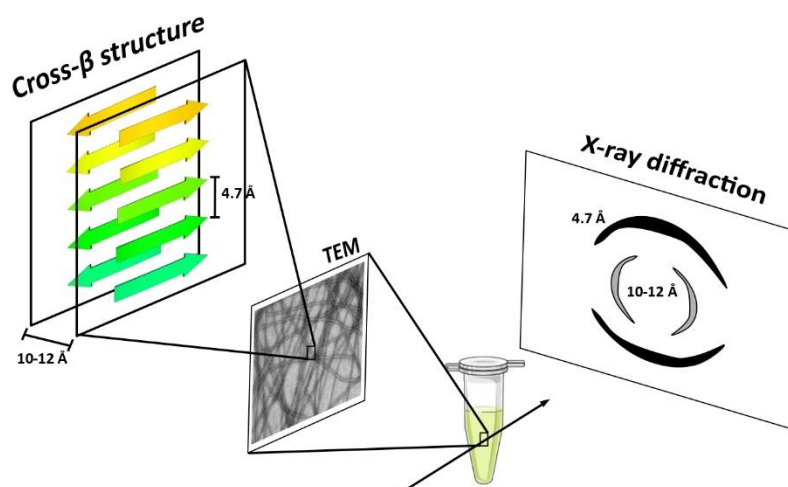


Fig. 5. Amyloid fiber features.

Amyloids are long and unbranched fibers when seen by electron microscopy. When amyloids are observed with XR, a characteristic cross- β diffraction pattern with two reflections is observed, one at 10-12 Å that corresponds to the inter-sheet space while the 4.7 Å reflection corresponds to the inter-strand space in the direction of hydrogen bonding. When the fibers are aligned, the XR reflections appear as arcs (like in the diagram). For unaligned fibers, the reflections are ring-shaped.

The structure of these type of fibers is very difficult to study by well-established techniques such as XR crystallography or solution NMR spectroscopy, mostly because of their non-crystalline and insoluble character. More recently, ssNMR and cryo-EM techniques have generated substantial advances in structural information and some amyloid structures have been determined (Fig. 6) (Loquet *et al.*, 2018; Fitzpatrick and Saibil, 2019; Röder *et al.*, 2019). On the one hand, the main advantage of using ssNMR over cryo-EM is the capacity to work with biological assemblies that show micro heterogeneities (in otherwise homogeneous and reproducible samples) that are a big problem on cryo-EM, although recent advances in cryo-EM image recording, processing and analysis are helping to deal with this problem. On the other hand, ssNMR needs large amounts of labelled protein samples due to its low sensitivity and requires long-time for data analysis.

INTRODUCTION

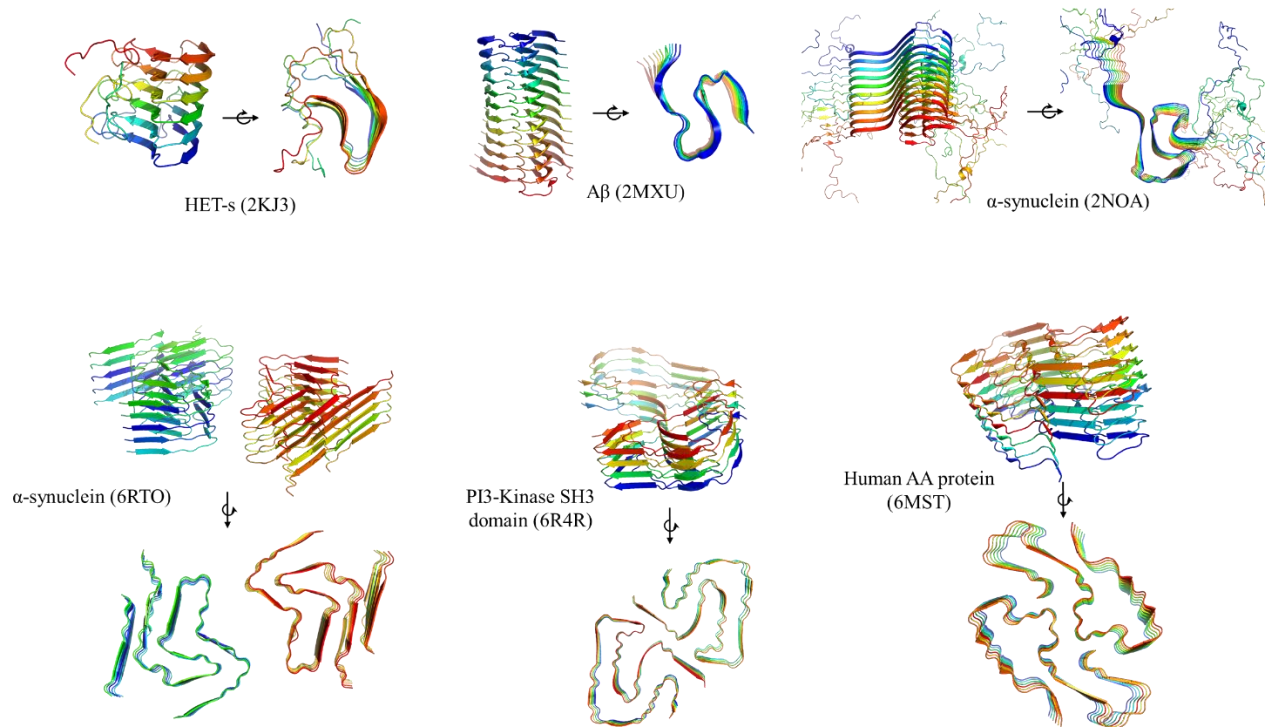


Fig. 6. Examples of high-resolution structures of amyloid fibers from the PDB database.

Top, ssNMR structures; bottom, cryo-EM structures with resolution below 4 Å.

Amyloids are composed of an ordered arrangement of thousands of copies of the same peptide or protein showing a repetitive structure. Under EM, the long unbranched fibers have a diameter between 6–12 nm. Protein or long peptide amyloids show structures that are more complex than it was anticipated from the study of short peptides but are still based on very flat β -sheets (Fig. 7). The low angle observed between strands usually leads to fibers with a helical rotation about their central axis showing a long pitch.

INTRODUCTION

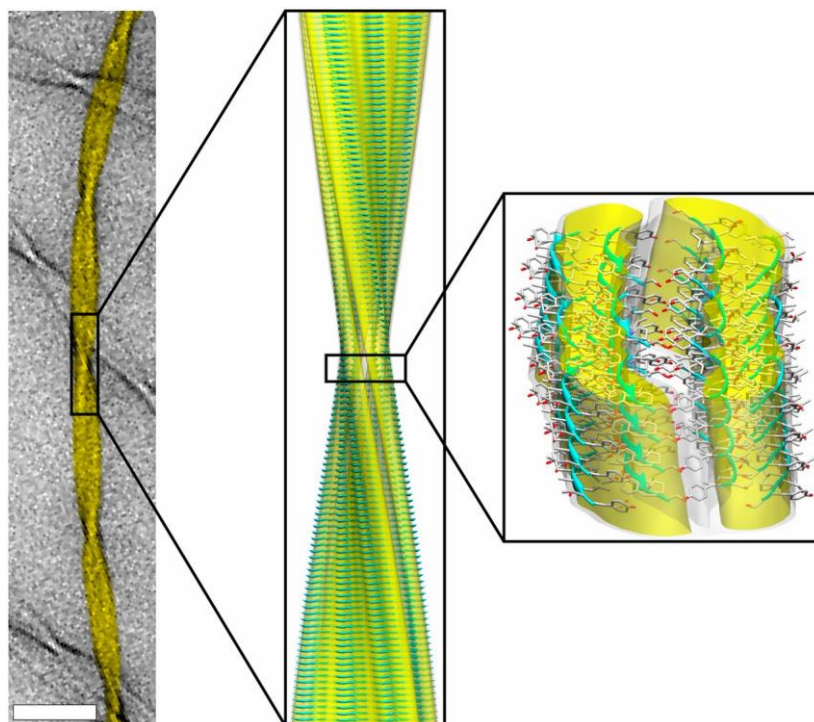


Fig. 7. Amyloid morphology and structure diagram.

Left, image of a fiber (11 residue peptide from transthyretin) taken using TEM. Center, ssNMR structure of the triplet fiber fitted into the cryo-EM reconstruction. Right, fiber surface and the constituent β -sheets. Adapted from Fitzpatrick *et al.*, 2013.

In amyloids, hydrophobic residues are mainly packed within the fiber core while hydrophilic and charged residues point towards the solvent (Fig. 8, left). This arrangement is kept between the strands of all the subunits to maintain the charge balance constant and stable. The high number of backbone hydrogen bonds and of hydrophobic interactions between complementary side chains are at the origin of the high stability and strength of amyloid fibers. It has been shown that the large network of intermolecular hydrogen bonds can confer to amyloids a mechanical strength comparable to that of steel (Lonescu-Zanetti *et al.*, 1999; Knowles *et al.*, 2007; Mankar *et al.*, 2011). Interactions like amide side chain hydrogen bonds observed for glutamine and asparagine residues (Nelson *et al.*, 2005), π stacking between aromatics (Gazit, 2002) or other steric zippers also significantly contribute to the stability of amyloids (Sawaya *et al.*, 2007).

INTRODUCTION

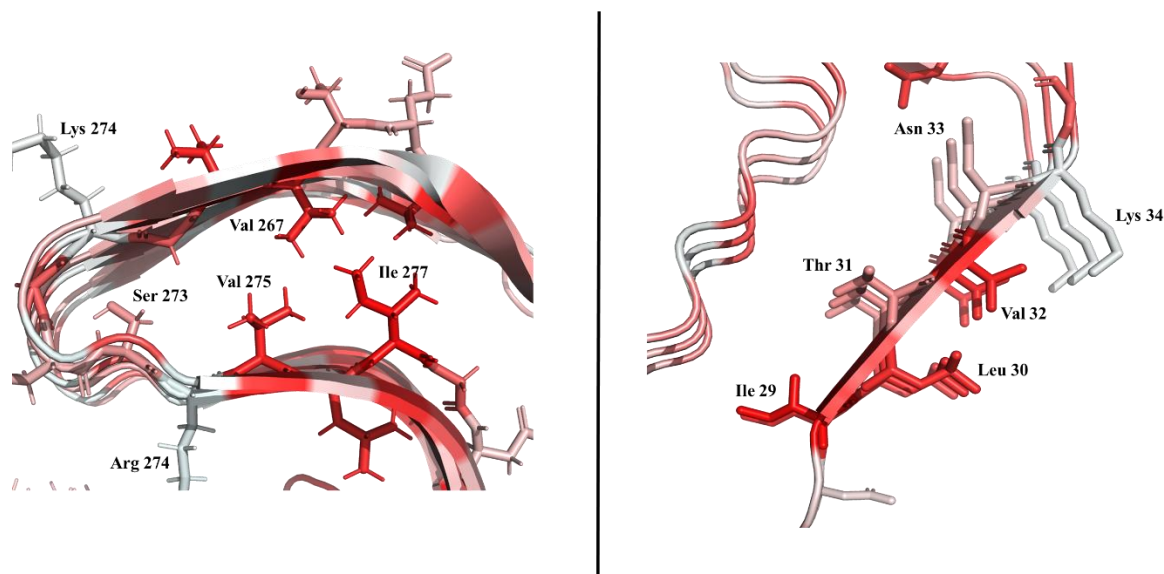


Fig. 8. Examples of stacked β -strands.

Left, HET-S (2KJ3) detail. Right, PI3-Kinase SH3 Domain (6R4R). Aminoacids are colored by hydrophobicity using PyMOL, the redder the more hydrophobic is the residue.

1.7.1 Functional and non-functional amyloids

Amyloids have been (and still are) historically related to disease. To date, there are 36 extracellular fibril proteins and 7 intracellular protein-based inclusions associated to amyloids diseases, including Alzheimer's, type II diabetes and Parkinson's (Chiti & Dobson, 2017). The societal impact of these generically called protein misfolding diseases is huge and their prevalence is ever increasing with the ageing of population and life style. Alzheimer's, type II diabetes and Parkinson's affect nowadays more than 500 million people and numbers keep increasing. Only in the US, it is estimated that the treatment of Alzheimer's costs more than 200 US billion dollars (Dobson, 2017).

The long time interest in amyloids is due to the importance of associated diseases and was further stimulated by the demonstration by the Prusiner's group that infectious diseases such as human (as Creutzfeldt Jacob or kuru) or bovine/ovine spongiform encephalopathies (mad cow disease, scrapie) were caused and propagated by proteins with an aberrant fold, the prions (Prusiner, 1998). The believe that the amyloid fold was unique to some proteins involved in disease was first challenged by a serendipitous finding that an SH3 domain (unrelated to any disease) under acidic conditions that destabilized the native fold could form amyloids and the

INTRODUCTION

demonstration led by the Dobson's group that under appropriate conditions many if not all normally globular proteins could self-assemble into amyloid fibers (Guijarro *et al.*, 1998; Chiti *et al.*, 1999). These findings stimulated research to understand how protein evolution had managed to limit/avoid this highly stable and self-propagating fold. Besides chaperons and cellular mechanisms (localization, synthesis regulation and degradation), some of the solutions to avoid irreversible formation of amyloids are encoded in the sequence of proteins (for instance, folding to hide aggregation prone sequences).

Concomitantly, proteins that adopt an amyloid fibrillar form to perform their biological function began to be discovered. Nowadays, described functional amyloids probably outnumber disease-related amyloids and new functional amyloids keep being reported. Functional amyloids have indeed been found in the three domains of life, Bacteria, Archaea and Eukaryotes, including humans. Amyloids can play important physiological roles (table 2), which can be structural, templating, storage, adhesion, biofilm and extracellular matrix formation, regulatory, etc. The role of several functional amyloids can also be to power-off the function of the soluble form of the protein.

Species	Organism type	Protein	Function
<i>Mycobacterium tuberculosis</i>	Bacteria	MTP	Adhesion, biofilm formation and cell-cell communication
<i>Escherichia coli</i>	Bacteria	Curli	Adhesion and biofilm formation
<i>Bacillus subtilis</i>	Bacteria	TasA	Colony biofilm formation
<i>Methanosaeta thermophila</i> and <i>Methanospirillum hungatei</i>	Archaea (methanogens)	MspA (major sheath protein A)	Part of cell wall (tubular sheaths) and possibly gas vesicles
<i>Aspergillus fumigatus</i>	Fungi	RodA	Surface attachment, aerial hyphae formation and surface tension modification
<i>Saccharomyces cerevisiae</i>	Fungi	Ure2p	Nitrogen catabolism (soluble protein)
Mouse, fish and silk moth	Animals	ZP proteins (ZP1-ZP3)	Formation of the amyloid matrix around the oocyte

INTRODUCTION

All mammals	Animals	Pmel17	Template during melanin synthesis in melanosomes
<i>Hevea brasiliensis</i>	Plants	REF (Rubber elongation factor)	Component of latex

Table 2. Examples of functional amyloids that can be found in nature.

Extracted from Otzen & Riek, 2019; Pham, Kwan, & Sunde, 2014.

1.7.2 How does the amyloid state form?

The amyloid state can be adopted by globular proteins with a variety of folds and secondary structure topology, by intrinsically disordered proteins (e.g. α -synuclein) or short peptides. Irrespective of the initial structure of the protein, and of whether amyloids arise from misfolding (disease related) or folding (functional) events, protein amyloids share a common cross- β structure, suggesting that some common features must exist in the process of amyloid formation. Amyloid formation implies important conformational changes, even in the case of globular all- β sheet proteins (Fig. 9).

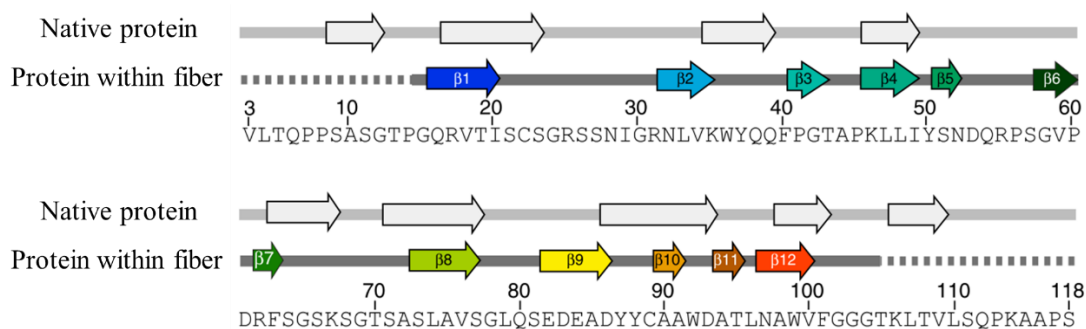


Fig. 9. Comparison of the secondary structure of the globular (native) and amyloid forms of an all- β protein.

Position of the β -strands in the fiber protein and in the natively folded of the immunoglobulin light chains (PDB 1BJM). Reproduced and modified from Radamaker *et al.*, 2019.

The high number of hydrogen bonds involved in the cross- β structure, the inter β -sheet side chain packing, possible intra β -sheet side-chain hydrogen bonds (Q/N) or aromatic rings π -

INTRODUCTION

stacking interactions render the amyloid state highly stable (more stable than the native globular fold or unfolded forms) and hence thermodynamically very favorable (Gazit, 2002; Baldwin *et al.*, 2011; Buell *et al.*, 2012). However, the energy barrier(s) to form amyloids can be very high (Fig. 10). The formation of amyloid fibers is an aggregation process that is thereby concentration dependent. It is also a nucleated phenomenon. First, for stable globular proteins, some destabilizing condition (such as pH, temperature or a destabilizing mutation) must favor unfolding or partial unfolding to permit conformational modifications to occur and allow the protein to exit the kinetically-trapped native meta-stable conformation. Then, oligomerization/conformational modification events must occur to form a nucleus that is competent to readily self-assemble into a cross- β structure. In vitro, amyloid fiber formation kinetics are usually monitored by the fluorescence of an amyloid reporter dye. The observed kinetics show a sigmoidal shape that is characteristic of nucleated phenomena (Fig. 11).

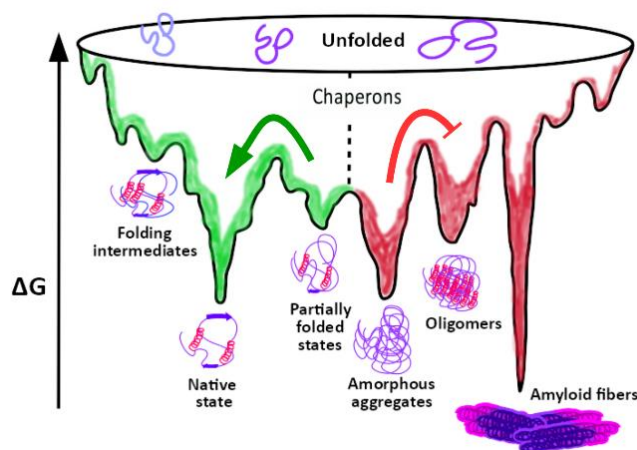


Fig. 10. Protein aggregation landscapes. Adapted from Landreh *et al.*, 2016.

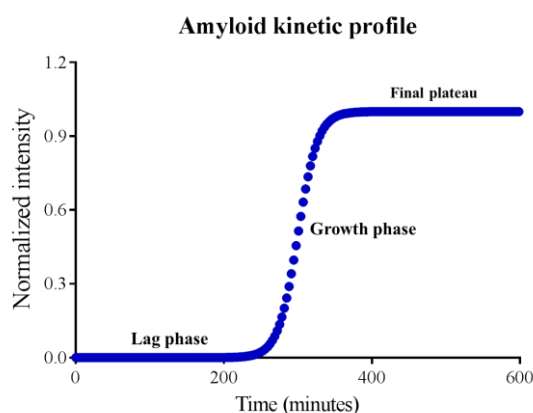


Fig. 11. Amyloid fibril formation kinetics plot.

INTRODUCTION

The fluorescence intensity reveals the appearance of the cross- β structure at the core of the fibers. The sigmoidal curve can be divided in three stages: the lag phase, the growth phase and a final plateau.

During the lag phase, soluble monomers form nuclei consisting of oligomers. The process that governs this phase is primary nucleation, in which monomers constantly interchange with forming nuclei (Fig. 12). At some point, the primary nucleation process leads to a critical concentration of nuclei from which fibers can form during the growth phase that is usually dominated by elongation and can have significant contributions from fragmentation and secondary nucleation processes. It can be an extremely rapid process in which monomers are added to the existing fibers. Fragmentation of fibers increases the number of sites at which monomers can incorporate to the fibers. Secondary nucleation is a self-catalytic process in which the surface of an existing fiber serves as a template to incoming monomers to form new fibers. This secondary nucleation mechanism is monomer concentration dependent and can dramatically accelerate fiber formation. After some time, the majority of the monomers are in the amyloid final form and speed decreases, it is the final stage, the final plateau, also called stationary phase, but still different processes such as fragmentation, elongation, secondary nucleation or exchange with monomers are happening (Arosio, Knowles and Linse, 2015; Meisl *et al.*, 2016).

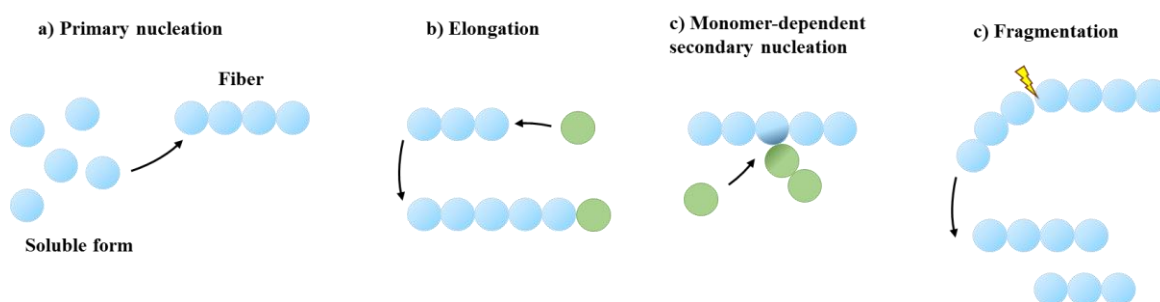


Fig. 12. Microscopic processes underlying amyloid formation.

Primary nucleation from monomers in solution (a), elongation (growth) by monomers addition to existing aggregates (b), surface catalyzed secondary nucleation from monomers on the fiber surface (c) and fragmentation (d) (adapted from Arosio *et al.*, 2015).

Understanding the mechanism of amyloidogenesis is very important both, in the case of disease-related amyloids and of functional amyloids. In the case of amyloid-related diseases, shedding light on amyloidogenesis and the intermediates involved is actually more important than understanding the structure of the fibers, because small aggregates seem to be at the origin

INTRODUCTION

of toxicity (Gustot *et al.*, 2015). Also, disease-related proteins show different polymorphs with distinct physical properties that can lead to a broad spectrum of disease phenotypes (Fitzpatrick and Saibil, 2019). Moreover, understanding the auto-association process might help in finding drugs to avoid protein aggregation (Gustot *et al.*, 2015). In the case of functional amyloids, understanding the mechanism of fibrillation and conformational plasticity of proteins to acquire their functional form is interesting *per se* and can provide useful information for amyloid related diseases. Perhaps, one of the main differences between proteins that aggregate into fibrils under abnormal conditions or have evolved to form amyloids, is the fiber polymorphism. Although in both cases, fiber structure is related to the influence of the environment, functional amyloids tend to show less polymorphism under controlled conditions (Tycko, 2015).

Therefore, the knowledge on how amyloid self-assemble is of vital importance to better understand amyloid-related diseases and important to understand how functional amyloids fold to perform their role in biological systems.

1.8 Hydrophobins

1.8.1 General aspects

Hydrophobins are surface-active proteins of low molecular weight (6-15 KDa) characterized by a conserved pattern of eight cysteine residues. These proteins are unique to filamentous fungi.

Hydrophobins were discovered by Wessels and co-workers in the early 1990s when studying gene expression during the development of the *Schizophyllum commune* fruiting body (J. Wessels *et al.*, 1991). Later studies showed that these proteins are surface-active proteins that spontaneously self-assemble at hydrophilic/hydrophobic surfaces into amphipathic layers or films with rodlet morphology resembling those previously reported in the 1960s by Hess and co-workers on the surface of *Penicillium* and *Aspergillus* conidia (Hess, Sassen and Remsen, 1968; Hess and Stocks, 1969; J. J. G. H. J. Wessels *et al.*, 1991; Wessels, 2000; Wösten, 2001). The proof that the hydrophobin layer covering fungal spores was hydrophobic came from the observation that a mutant of *Neurospora crassa* lacking the gene of the Eas hydrophobin is hydrophilic (Dempsey and Beever, 1979). The protein was named EAS, after the 'EASy wettable' phenotype observed for the mutant.

INTRODUCTION

Hydrophobins show, in general, very little conservation except for the idiosyncratic pattern of eight cysteine residues that form four disulfide bridges. These cysteines are interconnected as shown below (Fig. 13).

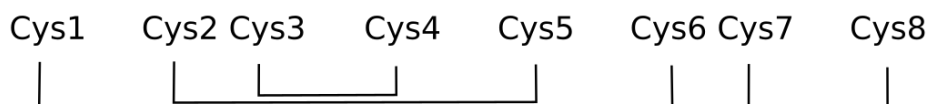


Fig. 13. Hydrophobin pattern of cysteines.

Eight cysteine (C) residues form four disulfide bonds with the same pattern (C1–C6, C2–C5, C3–C4, C7–C8). Cysteines C2-C3 and C6-C7 are contiguous in the sequence.

Based on their sequence, hydropathy pattern, solubility and structure formed upon self-assembly, hydrophobins are divided in two major classes, the Class I and Class II. Class I hydrophobins typically display low conservation and very variable inter-cysteine spacing whereas Class II are more conserved and show less inter-cysteine-spacing variability (Fig. 14). The hydropathy profile of hydrophobins also varies between classes I and II.

Class I

```

PRI2  SQCNNG--SIQCCNSSMTQDRGNLQIAQGVLLGG----LLGGLLGLGGLLDLVDLNLALIGVQCSP----ISIVG-----NANTCTQ-QTVCCSNNNFNG-----LIA--LG-CTPINI
ABH1  SQCDVG--EIHCCDTQQT-----PDHTSAAASG----LLGVPINLG-----AFLGFDCPTP----ISVLG----VGGNCAA-QPVCCTGNQFTA-----LINA-LD-CSPVNV
HCF1  GTCAVGS-QISCCPTNSS-----GSD-----ILGNV-----LGGSCLLDN---VSLISSLN----SNCPAGNTFCCPS-NQDG-----TLNINVS-CIPVSA
MPG1  QKCGAEK-VVSCCNSKELK-NSKSGAE-----IPIDV-----LSGECKNIPINILTINQLI--PINNFCSD-TVSCCSGEQIG-----LVN--IQ-CTPILS
SC4   QACNSG--PVQCCNETTT--VANAQ-KQGLLGG----LLGVVVGVP-----ITGLVGLNCSP----ISVVGV---LTGNSCTA-QTVCCDHVTQNG-----LVN--VG-CTPISL
EAS  NTCSIDDYKPYCCQSMSSG-----PAGSPGLLN----LIPVDSLAS-----LGC-----VVG----VIGSQCGA-SVRCCCKDDVTNTGNSFLIINA-AN-CVA---
RodA  EKCGDQA-QLSCCNKATYAG-DVTDIDEGILAGTLKNLIGGGS-----GTEGLGLFNQCCKSLDLQIPIIGIPIQLDLVNQKCKQ-NIACCQNSPSDASG--SLIGLGLP-CIALGS
  
```

Class II

```

HCF6  CP---ALDTPLCCQADVLGVLDLTCCEAPSDD-TSVSNFEAACATTG-LTARCCCLP-LLGEALLCTTP-----
HFBI  CPPG-LFSNPQCCATQVLGLIGLDCRVPSQNVYDGTDFRNVCAKTGAQ-PLCCVAP-VAGQALLCQTVAGA--
HFBI  CPTG-LFSNPLCCATNVLDLIGVDCKTPTIAVDTGAIFQAHCASKGSK-PLCCVAP-VADQALLCQKAIGTF-
CFTHI CPAG-LYSNPQCCATDVLGVADLDCKNPSSAPMSGDNFKSICNAVQQQ-ARCCVLP-VAGQAVLCQDSIN--
HYD4 CPDGLLIGTPQCCSLDLGVLSGECSSPSKTPNSAKEFQEICAASGQK-ARCCFLSEVFTLGFACQKPVGVTA
CU    CTGL-LQKSPCCNTDILGVANLDCHGPPSVPTSPSQFASCVADGGRSARCCFLS-LLGLALVCTDPVGI--
  
```

Fig. 14. Alignment of Class I and Class II of some commonly studied hydrophobins.

The highly variable N and C terminal parts of the sequences have been cropped. The conserved eight cysteine residues are highlighted in blue. The UniprotKB accession number and species of the aligned protein sequences are: PRI2 (Q9Y8F0) *Cyclocybe cylindracea*; ABH1 (P49072) *Agaricus bisporus*; HCF1 (Q00367) *Passalora fulva*; MPG1 (P52751) *Magnaporthe oryzae*; SC4 (P16934) *Schizophyllum commune*; EAS (Q04571) *Neurospora crassa*; RodA (B0Y4B10) *A. fumigatus*; HCF6 (Q9C2X0) *Passalora fulva*; HFBI (P52754) *Trichoderma reesei*; HFBI (P79073) *Trichoderma*

INTRODUCTION

reesei; CFTHI (Q9UVI4) *Claviceps fusiformis*; HYD4 (Q6YF29) *Gibberella moniliformis* and CU (Q06153) *Ophiostoma ulmi*.

Class I hydrophobins form rodlet layers displaying the hallmarks of amyloid fibers and are extremely robust, requiring treatment with concentrated acids (e.g. neat TFA, 50% HF, 50% formic acid) to induce disassembly. On the other hand, Class II hydrophobins form non-fibrillar amorphous aggregates that can be solubilized in organic solvents or detergents at high temperature and do not show amyloid characteristics (Kwan *et al.*, 2006; Kordts *et al.*, 2018).

The morphology of the films formed by Class I and II hydrophobins also differs: while Class I hydrophobins form very ordered rodlets, Class II hydrophobins generally form amorphous films (Fig. 15).

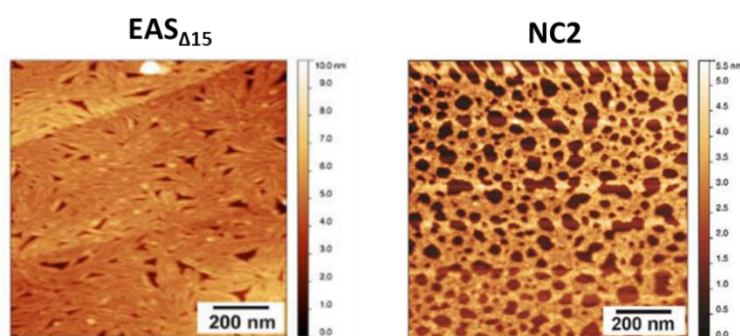


Fig. 15. Rodlets images seen under AFM.

AFM images of films formed on HOPG (highly oriented pyrolytic graphite) by EAS_{Δ15} (Class I) and NC2 (Class II) from *Neurospora crassa* (reproduced from Lo *et al.*, 2014).

Based on bioinformatics, a third class (Class III) of hydrophobins with intermediate or different characteristics has been proposed. Putative hydrophobins from Class III have an intermediate hydrophobicity profiles and/or inter-cysteine spacings and can display more cysteine residues, lack one of them, lack secretion signal peptides or have very long N or C-terminal tails (Jensen *et al.*, 2010; Littlejohn, Hooley and Cox, 2012). It should be mentioned that to the best of our knowledge, no Class III hydrophobin has been studied so far.

Hydrophobins are secreted by fungi as soluble proteins. Several structures of the soluble form of hydrophobins that auto-associate to form amphipathic layers have been described. The structures show a common central β -barrel or semi- β -barrel topology organized around the four disulfide bridges. Two of the disulfide bridges are located inside the β -sheet core linking β -strands, whereas the other two link this core to external structural elements. In Class II

INTRODUCTION

hydrophobins, the central β -sheets generally form a β -barrel, whereas this core is a semi- β -barrel in most of Class I structures. In addition to the core, hydrophobins display flexible loops and α -helical elements (Fig. 16). The diversity of hydrophobin sequences is reflected in the differences in structure shown by hydrophobins.

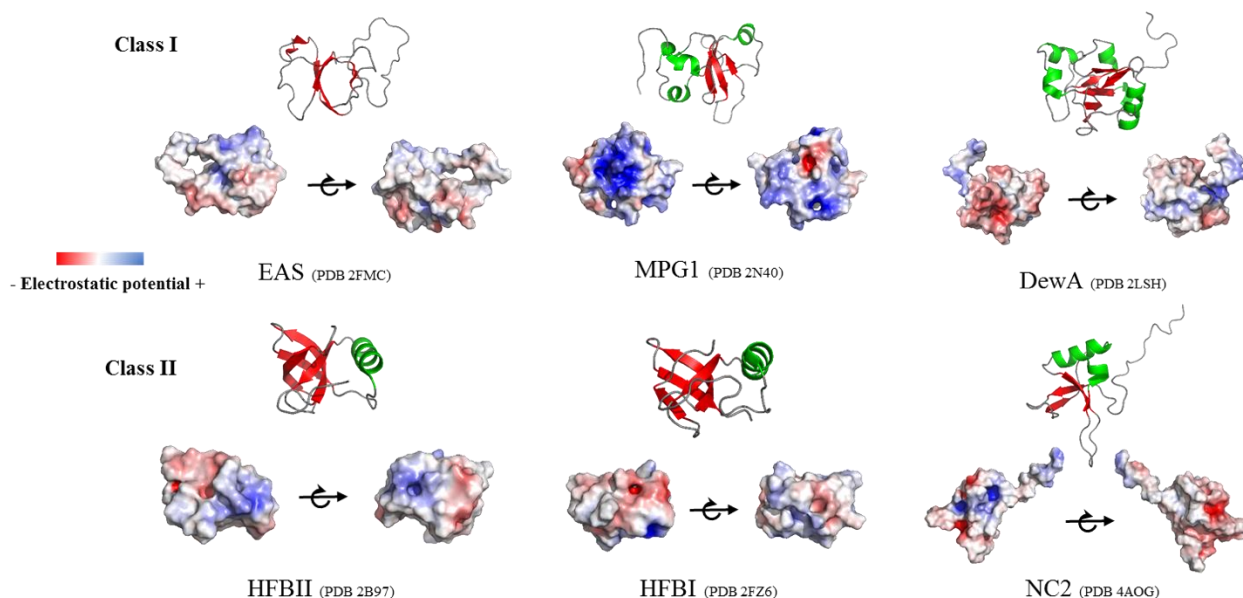


Fig. 16. Class I and Class II hydrophobins cartoon and surface representations showing the structure and electrostatic potential, respectively.

EAS (2FMC) from *Neurospora crassa*, MPG1 (2N40) from *Magnaporthe oryzae*, DewA (2LSH) from *Aspergillus nidulans*, HFBII (2B97) from *Trichoderma reesei*, HFBI (2FZ6) from *Trichoderma reesei* and NC2 (4AOG) from *Neurospora crassa*. β -sheets are colored in red and α -helices in green. The PyMOL plugin APBS was used to display electrostatic potentials.

Despite their structural differences, hydrophobins show two other common features in addition to the central rigid core. First, the N-terminal region upstream cysteine C1 and the loop regions between cysteines C3-C4, C5-C6 and C7-C8 are highly flexible (Pille *et al.*, 2015). Second, the monomers display hydrophobic and charged patches at their surface or are amphipathic (Fig. 16). This amphipathic character enables the proteins to migrate to the AIW or HHI (Fig. 17), where the monomers undergo conformational changes triggered by the physical properties of the interface and assemble into amyloid or amorphous layers. Studying the effect of surfactants (ionic, non-ionic) and alcohols on the auto-association of the hydrophobins DewA and EAS, it has been shown that surface tension is the driving force to address hydrophobins

INTRODUCTION

to the surface and that a minimal surface tension (which can be different for each hydrophobin) is required to self-assemble at an AWI (Morris *et al.*, 2011; Pham *et al.*, 2016; Sunde, Pham and Kwan, 2017).

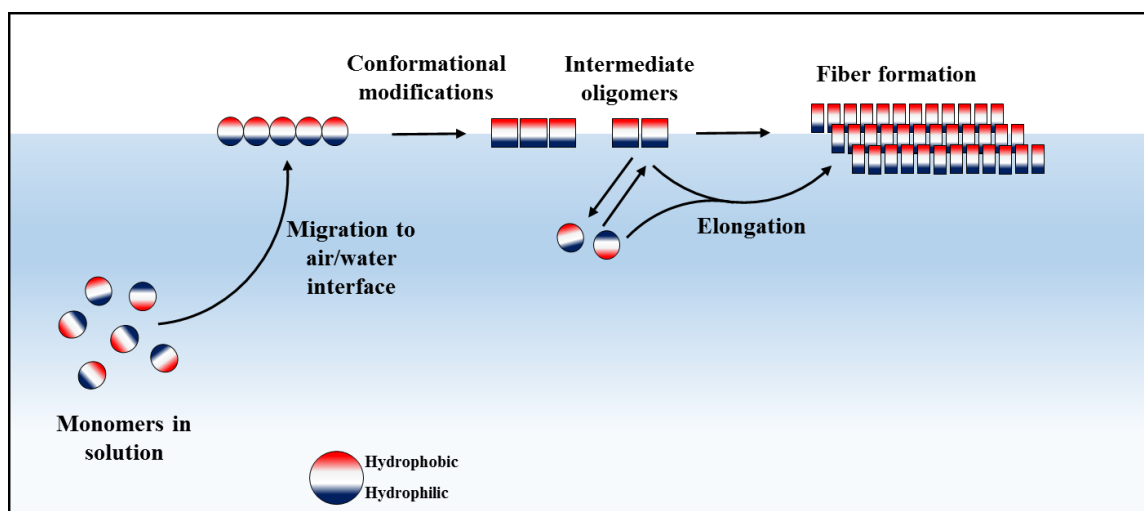


Fig. 17. Proposed simple model of *in vitro* Class I hydrophobin aggregation.

The monomers with surface exposed hydrophobic regions reach the AWI or HHI, undergo conformational changes and associate into oligomeric nuclei that can readily convert into amyloid fibers that laterally associate into layers.

Aggregation of hydrophobins can follow a complex mechanism. For instance, the Class I hydrophobin SC3 assembles to the rodlet state *via* two intermediates. The first is an α -helical state that is formed upon binding to an hydrophobic solid, the second is an amorphous β -sheet state formed at the AWT, which after some hours spontaneously, acquires the rodlet morphology (de Vocht *et al.*, 2002).

Because hydrophobin amyloids are self-propagating structures, different mechanisms have been described to regulate or limit aggregation of the monomers that could be harmful for the fungal cells. DewA, a protein found in the spores of *A. nidulans*, populates two conformers (with the same disulfide bridges) in solution that are amyloidogenic. While both conformers readily form amyloids at high concentrations, one of them forms off-pathway dimers thus reducing the rate of self-assembly into amyloids (Morris, Kwan and Sunde, 2013).

In silico studies with EAS have suggested that large flexible loops may inhibit aggregation in solution because of the high cost of reducing their conformational entropy and only in the presence of an anisotropic surface providing surface tension (that can be seen as a force that counterbalances conformational entropy) the protein can self-assemble (De Simone *et al.*,

INTRODUCTION

2012). Based on the relative rates of the reduced and oxidized forms of SC3, it has also been proposed that the idiosyncratic S-S bonds of hydrophobins can reduce the rate of fiber formation and that they represent a mechanism to avoid fast deleterious aggregation within cells (De Vocht *et al.*, 2000).

Although Class I hydrophobin self-assembly can differ from one hydrophobin to another, these proteins share common characteristics. Within very variable structures, the central β -barrel or half-barrel core and the amphipathic character of the monomer allowing it to reach the HHI have been observed for all the monomeric proteins studied. Also, it has been shown for some hydrophobins that an HHI is required to trigger the conformational changes that lead to self-assembly, although some hydrophobins like SC3 or Vmh2 can form nanorods or amyloids in bulk solution, respectively (Zykwinska *et al.*, 2014; Gravagnuolo *et al.*, 2016).

1.8.2 Biological functions

The function of hydrophobins relies upon the physicochemical characteristics of the layers they form. One of the best studied hydrophobin is SC3, a protein produced by *Schizophyllum commune* when conditions are optimum to generate aerial hyphae to form the fruiting body and reproduce. The main role of SC3 is to cover the surface of the aerial hyphae and allow these structures to reduce the surface tension of water and breach the AWI. *S. commune* SC3 deletion mutants are not able to form aerial structures but addition of recombinant SC3 to the medium complements the deletion and allows the fungus to form aerial structures. These observation indicated the critical role of SC3 in the correct development of the fungus (Wösten, 2001). Similarly, hydrophobins (hypA) have been found in the “portobello mushroom”, the edible *Agaricus bisporus*. Here, hydrophobins reduce wetting and help mediate resilience to environmental stresses (Lugones *et al.*, 1996). We can appreciate this edible layer when cleaning in the kitchen the mushroom’s cap, a very smooth semi-waterproof layer that covers it.

Hydrophobins can help on dispersion too. Indeed, the hydrophobic character of the hydrophobin coat that covers the spores facilitates air dispersal. Moreover, this coat provides resistance to desiccation and wetting, while warranting gas exchange.

Hydrophobins can play an important role in attachment, especially in the case of plant pathogens. For example, the hydrophobin CU from *Ophiostoma ulmi* that causes the Dutch elm disease, participates during the attachment of the fungus to the plant at the first stages of the

INTRODUCTION

infection. Similarly, MPG1 produced by *Magnaporthe grisea*, the main parasite of rice cultivars is used by the fungus to attach to the leaf surface (Dean *et al.*, 2012). Other roles have been described for hydrophobins in plant-fungi or insect-fungi interactions (reviewed in Bayry *et al.*, 2012).

1.8.3 Applications

Like their biological roles, the foreseen applications of hydrophobins mainly rely on their remarkable physicochemical properties. Their high surfactant activity, their capacity to cover surfaces and invert their polarity (hydrophobic into hydrophilic and vice versa), their stability and, mechanical and chemical resistance make these proteins interesting candidates for applications in biotechnology. For example, their potential as emulsifying agents, hydrophobin-based nanoparticles for hydrophobic drug delivery, in electro-chemical biosensing applications, cell immobilization, or protein purification tags, has been investigated (Bayry *et al.*, 2012; Berger and Sallada, 2019). Recently, Winandy *et al.*, 2019 have used DewA and HFBI to coat stones or concrete for conservation of architectural heritage. They have shown that coating with a hydrophobin layer confers an effect similar to “Gore-tex”, a waterproof material consisting of Teflon® fibers that is permeable to air and widely used to make fabrics.

The immunological inertness of hydrophobins (Aimanianda *et al.*, 2009) coupled to their capability to form highly stable membranes make them attractive candidates for orthopedic implant coatings. In this sense, Boeuf *et al.*, 2012 have shown that coating with DewA enhanced mesenchymal stem adhesion without interfering with their functionality and preventing bacteria cell attachment and infection. Coating of allergenic/immunogenic proteins with immunologically inert hydrophobins has also been proposed (Bayry *et al.*, 2012). Nonetheless, large-scale applications of hydrophobins might be difficult to implement due to the production cost of recombinant proteins and might be reserved to high-added value applications and will require an optimization of the production.

1.8.4 *Aspergillus fumigatus* hydrophobins

In addition to RodA that coats *A. fumigatus* spores, facilitating dispersion, rendering the spore's waterproof, preventing desiccation, helping the conidia to reach the lung alveoli and masking the immunogenic components of the cell wall from the immune system, *A. fumigatus* genome codes for 6 other hydrophobins (RodB-RodG).

INTRODUCTION

RodA, RodB and RodC are Class I hydrophobins. The three proteins are present in the conidial cell wall (Pham *et al.*, 2018; Valsecchi *et al.*, 2018; Valsecchi *et al.*, 2019b) and are close homologs sharing ~ 40% sequence identity. Correspondingly, these proteins show very similar hydrophobicity profiles (Fig. 18).

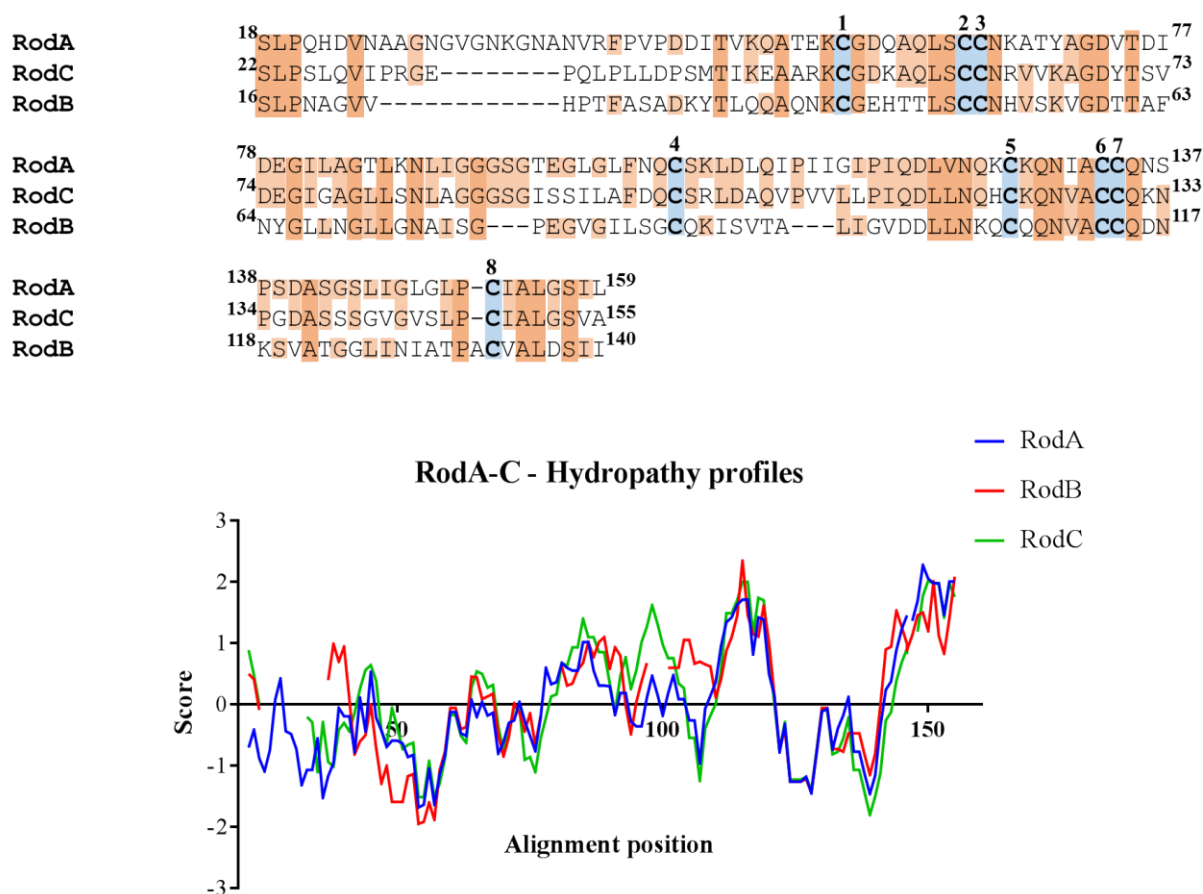


Fig. 18. RodA-C sequence and hydrophathy profiles comparison.

Top, RodA, RodB and RodC ClustalW2 (Thompson, Higgins and Gibson, 1994) alignment with color coded similarities (the darker the color the higher the similarity). Bottom, hydrophathy profiles alignment (Kyte and Doolittle, 1982). RodD is a strange hydrophobin (its classification is controversial) characterized by the absence of a secretion signal, a long C-terminal tail and a different hydrophathy profile. RodE has three additional cysteine residues and a typical Class I hydrophathy profile and is considered as class I hydrophobins. RodF contains an extra-cysteine residue in the N-terminal region and its hydrophathy profile fits the Class I hydrophobins type. RodG shows a class I hydrophobicity pattern, but a short C5–C6 region for Class I or Class II hydrophobins and an unusually long C3–C4 region for a Class II hydrophobin, thus its consideration as hydrophobin is controversial (Fig. 19).

INTRODUCTION

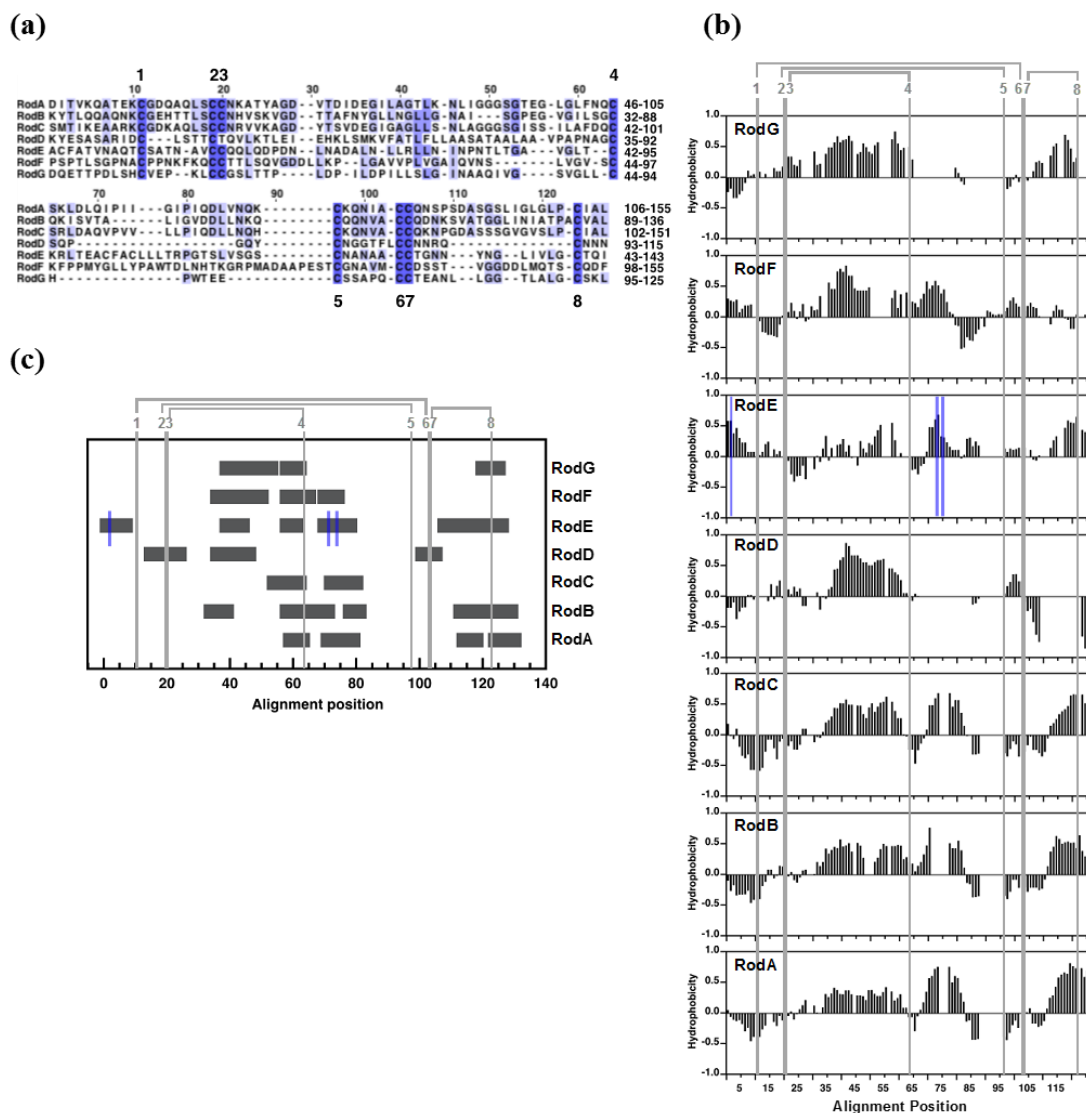


Fig. 19. Alignment of *A. fumigatus* hydrophobins.

(a) Sequence; (b) hydrophobicity profiles; (c): amyloidogenicity predicted with amyIpred2 (Tsolis *et al.*, 2013). Alignments only include the regions with the hydrophobin idiosyncratic Cys-residues motif. The positions of hydrophobin Cys-residues are labeled in their order of appearance from 1 to 8 throughout this work. The disulfide topology is shown in grey. In (a), the alignment position is shown on top and sequence numbering on the right; the intensity of the blue color reflects the degree of identity. In (b, c), the position of the three extra Cys-residues of RodE is indicated. Reproduced from (Valsecchi *et al.*, 2018) with the consent of the authors.

Analysis of the expression of the 7 hydrophobins in sporulating conidia, vegetative growth (planktonic or biofilm) and in an invasive aspergillosis mice model indicated that, except RodG that is only barely expressed in biofilms, all the hydrophobin genes are significantly expressed in some condition (Valsecchi *et al.* 2018).

INTRODUCTION

In an attempt to understand the function of *A. fumigatus* hydrophobins, Valsecchi *et al.* (2018) recently obtained and characterized the phenotype, immunogenicity and virulence of multiple Rod-deletion mutants. The genes for RodB to RodG were sequentially disrupted to obtain deletion mutants $\Delta rodB$, $\Delta rodBC$, ..., and $\Delta rodBCDEFG$. This work indicated that only RodA was responsible for the rodlet layer covering the spores, its hydrophobicity, immunological inertness, and had an effect on *in vitro* virulence and resistance to chemical or physical stress. Although the role of hydrophobins RodB to RodG remains unknown, the fact that the corresponding genes are differentially expressed under different conditions and that the RodB and RodC proteins have been detected on spores, suggests that these hydrophobins play a yet unidentified role in the fungus biology.

The most studied *A. fumigatus* hydrophobin is RodA. Collaborative work of five laboratories on wild-type and mutant RodA combining biophysical (solution NMR, electron microscopy [EM], atomic force microscopy [AFM], fluorescence of amyloid binding dyes), biochemical and immunological strategies and coupling *in vitro/in vivo* studies has provided novel results: (i) native recombinant RodA self-assembles *in vitro* into rodlet layers with a similar morphology to the one observed on the surface of the spores; (ii) the determination of the native disulfide bond pairing of the protein extracted from spores by NMR (iii) the structure and dynamics of the soluble form of RodA; (iv) the integrity of the native disulfide bridges is required to form well-ordered rodlet layers *in vitro* and *in vivo*; (v) valuable insights into the mechanism of rodlet formation and the identification of two amyloidogenic residues that may be involved in the cross- β spine of the amyloid fibers; (vi) correlation between *in vitro* and *in vivo* rodlet formation kinetics for WT and mutant RodA; (vii) immunological characterization of *A. fumigatus* RodA mutants (cysteine and slow-self-assembling mutants), mutant proteins and different states of the protein (soluble native and unfolded forms, rodlets) that have indicated that the unfolded, native monomeric and rodlet forms of RodA are not recognized by the human innate immune response. Many of the results of this work were recently published (Valsecchi *et al.*, 2019a).

The structure of RodA shows the typical fold of hydrophobins organized around the four disulfide bridges, with a central β -barrel highly constrained by two disulfide bonds. The β -barrel is linked to two α -helices by the two other disulfide bridges (Fig. 20). Analysis of the dynamics of the protein by ^{15}N relaxation has shown that the core of the structure is rigid, that the N-terminal region of the protein is disordered and that the C4-C5 and C7-C8 inter-cysteine loop regions are flexible. The surface of the protein shows an amphiphilic character with two

INTRODUCTION

hydrophobic patches in these dynamic regions as well as in the C3-C4 region. A single-point mutational analysis coupled to peptide characterization identified 6 hydrophobic residues in the C7-C8 and C4-C5 flexible regions that retard fiber formation *in vitro*, and it was shown that mutations at two of those positions also retard rodlet formation at the surface of the spores.

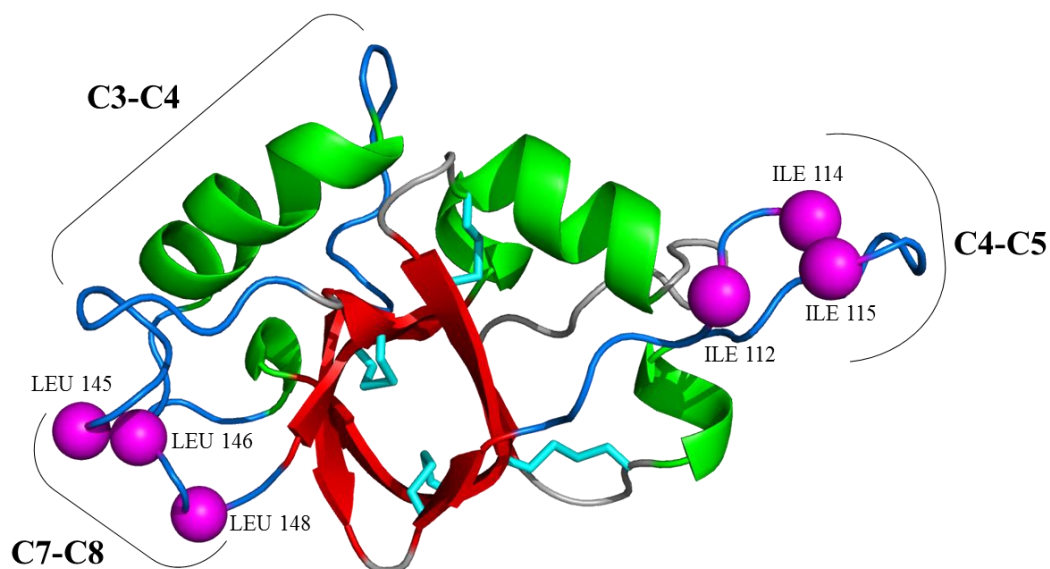


Fig. 20. RodA solution structure.

Cartoon representation of the solution structure of RodA (PDB: 6GCJ) with the disulfide bonds, colored in cyan, β -sheets are colored in red, α -helices in green and inter-cysteine loop regions in blue marine and indicated. Important residues for RodA self-assembly are highlighted as magenta spheres. Cysteines are indicated by the respected position in the sequence.

As in other hydrophobins, the surface exposed hydrophobic patches displayed by RodA seem to be important to address the protein to the HHI/AWI where conformational rearrangements and assembly into amyloids take place. Mutational analysis work on the EAS hydrophobin had also identified an amyloidogenic sequence in the hydrophobic and dynamic C7-C8 region that might be involved in the cross- β core of the fibers (Macindoe *et al.*, 2012) and hydrogen-deuterium exchange experiments on SC3 had put forward the relevance of the C3-C4 region for adhesion to hydrophobic surfaces and suggested its implication on rodlet formation (Wang, 2004).

1.9 Project description

My doctoral work was devoted to better understand the self-assembly of *A. fumigatus* Class I hydrophobins, namely RodA-C. Understanding the mechanism of amyloid formation is an interesting problem per se but is also important for biomedical or biotechnological applications. In parallel to my main project, with Isabel Valsecchi, we tried to produce recombinant folded RodE and RodF, two Class III hydrophobins, with the aim of studying for the first time a Class III hydrophobin and assessing whether these proteins self-assemble into amyloids or other morphologies and form amphipathic layers. Unfortunately, despite several efforts to produce the proteins using *E. coli* expression in the cytoplasm with strains that permit oxidation of cysteines (Origami, Shuffle) or in inclusion bodies and *in vitro* oxidative folding under different conditions, we never obtained a folded protein. These attempts are not described in this dissertation.

Building on the knowledge acquired on RodA and taking benefit of the possibility of comparing the self-assembly of three close homologs (RodA-C) to understand the amyloidogenic determinants of hydrophobins, the laboratory characterizes the mechanism of self-assembly of the three Class I hydrophobins from the opportunistic pathogen *A. fumigatus* coupling in a collaborative work solution and solid state NMR, EM, AFM, FT-IR (Fourier Transform Infrared Spectroscopy), SRCD (Synchrotron Radiation Circular Dichroism), fluorescence of amyloid binding dyes and the effect of mutations on self-assembly.

I was particularly implicated in the characterization of RodC and the comparison of its mechanism of assembly with that of RodA and RodB. In the first chapter I present the work we performed in collaboration with the laboratory of Margaret Sunde (University of Sydney) on the characterization of six hydrophobins present on the spores of *N. crassa* (EAS), *M. grisea* (MPG1), *A. nidulans* (DewA) and *A. fumigatus* (RodA-C). We aimed at understanding the secondary structure conformational changes that occur upon amyloidogenesis and the influence of the nature of the HHI or AWI on the self-assemblies formed by these surface-active proteins.

In the second chapter, I describe the characterization of the self-assembly of RodC. As a first step to understand the mechanism of self-assembly and the structural changes that occur, it is necessary to know the structure of the monomeric state. I thus describe the current status of the structural analysis of the native state of RodC by solution NMR. I also briefly describe our attempts to study the structure of the amyloid state of RodC by solid state NMR (ssNMR, collaboration with A. Loquet, IECB, Bordeaux) and of RodA and RodB. To get further insights

INTRODUCTION

on the mechanism of self-assembly, the kinetics of amyloid formation followed by the binding of the amyloid reporter dye ThT were performed as a function of concentration, temperature and studying amyloid formation from the native monomeric state and the reduced and unfolded state of RodC. The results are qualitatively analyzed under the light of the microscopic events that lead to fiber formation and the requirement of an HHI/AWI as shown for RodA-C in Chapter 1. To pinpoint the residues and regions that are important for amyloid formation, we analyze the effect of point mutations on the kinetics of amyloid formation of RodC, coupled to the characterization of peptides issued from the RodC sequence. Finally, we analyze the effect of major cell wall components and analogs of *A. fumigatus* spores on the self-assembly of RodC to investigate the possible templating effect of these molecules, which might be of relevance for RodC amyloidogenesis on the spores' cell wall.

Materials & Methods

2 Materials & Methods

2.1 Proteins and peptides studied

Several proteins and peptides have been studied. We have produced and purified RodA, RodB, RodC, RodE and RodF hydrophobins; 14 RodC mutants, and we have characterized 4 RodC related peptides (tables 3 and 4).

	Accession number (UniprotKB)	Residues	Molecular weight	Isoelectric point	Molar absorption coefficient (ml/ (cm.mg)
RodA	P41746	19-159	14542	4.9	0.137
RodB	B0XPA4	17-183	12853	6.3	0.272
RodC	B0Y9E4	23-155	13679	6.0	0.145
RodE	B0Y9N0	1-145	15363	10.4	0.097
RodF	B0Y2S5	19-190	20452	9.7	0.512

Table 3. Rod hydrophobins.

The residues used to produce recombinant proteins correspond to the protein without N-terminal signal peptide (which is cleaved by the mold upon secretion). The molecular weight, theoretical isoelectric point and extinction coefficients (Pace *et al.*, 1995) correspond to the recombinant proteins, which contain one (S) or 2 (GS) additional N-terminal residues. Molecular weights were calculated for the fully oxidized proteins.

Single point mutations of RodC (X→G)		M7	V110G	RodC peptides	
Number	Mutation	M8	V111G	Name	Sequence
M1	Y70G	M9	L112G	M2P	⁷⁹ AGLLSNLA ⁸⁶
M2	L82G	M10	L113G	M4P	⁹² ISSILAFD ⁹⁹
M3	I95G	M11	V144G	M7P	¹¹⁰ VVLLPI ¹¹⁵
M4	L96G	M12	L146G	M12P	¹⁴⁰ SGVGVSLP ¹⁴⁶
M5	V108G	M13	I149G		
M6	P109G				

Table 4. RodC point mutants and peptides.

Tables show the 13 single point mutants named M1 to M13 according to their relative position in the sequence and the peptides derived from the RodC sequence. Peptides MXP are named

MATERIALS & METHODS

after the single mutation region to which their sequence corresponds. An additional quadruple mutant named QM was studied (I95G, L96G, V144G, L146G).

Plasmid design, protein expression and purification are described in the next sections.

Peptides issued from the sequence of RodC (Fig. 21) were purchased from ProteoGenix. Their sequence corresponds to four predicted amyloidogenic regions that were probed by point mutants. The N- and C-terminal residues of the peptides were formylated and amidated, respectively, to avoid introducing charges that could hamper amyloid formation.

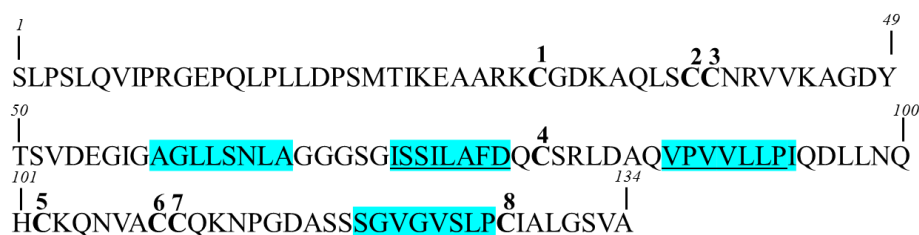


Fig. 21. RodC sequence.

The eight cysteine residues are highlighted in bold and numbered by their order of occurrence in the sequence. The predicted amyloidogenic regions underlined. The 4 designed peptides are indicated in blue.

2.2 Plasmid design

Hydrophobins and their mutants were produced as fusion proteins with ubiquitin and an N-terminal hexahistidine tag. The sequence contains a cleavage site (either for TEV or Ubp41 proteases, (Pille *et al.*, 2015) between ubiquitin and the hydrophobin (Fig. 22). Ubiquitin was used as a fusion protein to help maintain soluble the unfolded protein and intermediates during the *in vitro* oxidative folding step (see below). It was chosen for its small size and because it does not contain cysteines like GST, another protein often used to express and purify proteins. RodA and RodB were cloned in a pET15b plasmid (Novagen) coding for ampicillin resistance and a TEV cleavage site. A pET28b vector (Novagen) with kanamycin resistance coding for an Ubp41 cleavage site was used for RodC and RodC single point mutants. Multiple point mutants were cloned in a pET15b (ampicillin resistance and TEV cleavage site).



Fig. 22. Fusion protein design for hydrophobin production.

MATERIALS & METHODS

The sequence encodes for the protein of interest (hydrophobin Rod proteins and mutants) fused to ubiquitin with linking sequence corresponding to a cleavage site (yellow ray). The sequence encodes for an N-terminal hexahistidine.

All plasmids were ordered to ProteoGenix.

2.3 Expression and purification

Plasmids were transformed using heat shock in *Escherichia coli*. RodA and RodB were produced using the BL21 (DE3) strain. For RodC, we additionally tested Origami B (Novagen) cells in an attempt to produce native oxidized proteins in the cytoplasm. For Rod E and F, we also tried the Shuffle (New England Biolabs) strain. The Origami and Shuffle strains can in principle allow the production of disulfide containing proteins in the cytoplasm because both lack the thioredoxin and glutathione reductases. Additionally, the Shuffle strain contains the disulfide isomerase DsbC and cytoplasmic chaperones (DnaKJE, GroELS, ClpB) to facilitate the exchange of S-S and favor the formation of native S-S linkages (de Marco, 2009). For RodC, low yield of soluble and folded protein was obtained; RodC and its mutants were therefore produced as inclusion bodies using standard BL21 (DE3) *E. coli* strain. Importantly, WT RodC produced in the cytoplasm or oxidatively folded *in vitro* gave the same ^1H - ^{15}N HSQC spectra.

The same expression and purification protocols were followed for all native and mutated hydrophobins. Bacteria were grown at 37°C and expression was induced with 0.5 mM isopropyl β -D-1-thiogalactopyranoside (IPTG) at an absorbance of 0.6 at 600 nm. LB broth was to produce unlabeled proteins and M9 media for labelled proteins. M9 media contains $^{15}\text{NH}_4\text{Cl}$ and $^{13}\text{C}_6$ glucose (Eurisotop) to label ^{15}N and $^{15}\text{N}/^{13}\text{C}$ the proteins for NMR (Pham *et al.*, 2018). Cells were harvested by centrifugation after 4 h of induction at 37° C and frozen at -80° C.

The fusion protein was solubilized from the inclusion bodies with 6 M guanidinium hydrochloride pH 8.0 buffer (it contains 6 M guanidinium hydrochloride, 10 mM Tris-HCl pH 8.0, 100 mM NaH_2PO_4 and 1 $\mu\text{L}/3\text{mL}$ β -Me) and purified on a nickel affinity column (HisTrap, GE Healthcare) under denaturing conditions (8 M urea, 10 mM Tris-HC pH 8.0, 100 mM NaH_2PO_4 and 1 $\mu\text{L}/3\text{mL}$ β -Me). The *in vitro* oxidatively folding was performed by dialysis against a refolding buffer (100 mM NaCl, 50mM CH_3COONa pH 5.0, and 10 mM reduced and 1 mM oxidized glutathione). His-ubiquitin was then cleaved using either the deubiquitinase

MATERIALS & METHODS

UBP41 or the TEV enzyme and removed on nickel affinity columns (HisTrap, GE Healthcare). Hydrophobins were further purified by reverse-phase chromatography on hydrophobic C₁₈ or C₄ columns (Waters) with acetonitrile gradients. This step also separates the protein with correct S-S bonds from forms with incorrect and inter-monomeric disulfide linkages. A last step of purification by size exclusion chromatography was used to separate the monomeric form from aggregates. Proteins were dialyzed against H₂O and lyophilized until further use.

To check the purity, integrity and folding state of all purified proteins, we used polyacrylamide gel electrophoresis under denaturing and reducing conditions (SDS-PAGE), MALDI-ToF/ToF mass spectrometry (UltraFleXtreme, Bruker, Biophysics Platform of the Institut Pasteur) (integrity and purity) of the proteins and 1D ¹H or 2D (¹⁵N HSQC) NMR spectroscopy (purity, foldedness and integrity).

2.4 Solution nuclear magnetic resonance spectroscopy

We used NMR to complete the assignment of RodC as a first step to obtain its solution structure and to evaluate the purity, integrity and folding state of all purified proteins used in this study.

2.4.1 Assignment principle

To interpret NMR data (chemical shifts, relaxation rates, couplings, nuclear Overhauser effects...), it is necessary to first assign the signals (their resonance frequency expressed in ppm relative to a reference compound) to the atoms of the molecule. For proteins, the assignment strategy consists on first assigning the backbone and CB atoms using through-bond correlations based on J couplings of the ¹H, ¹⁵N and ¹³C atoms of ¹⁵N/¹³C doubly labeled proteins. The most important atoms in this strategy are backbone ¹H and ¹⁵N amide atoms. The spectrum that correlates both atom resonances is the ¹H-¹⁵N HSQC (heteronuclear single quantum correlation experiment), or other variants (HMQC, SOFAST...). This spectrum, which contains one ¹H and one ¹⁵N dimension, is a fingerprint of the structure and the dynamics of the protein. In an HSQC, each NH group normally generates one peak. Also, the tryptophan indole, asparagine and glutamine side-chain amides, and at ~low pH and/or ~low temperature arginine guanidinium and lysine amine resonances can be observed (Fig. 23).

MATERIALS & METHODS

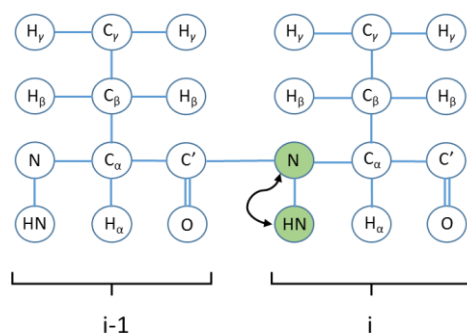


Fig. 23. HSQC experiment.

In this experiment, the magnetization is transferred from a hydrogen atom to an attached ^{15}N nucleus via the ^1H - ^{15}N J coupling (90-95 Hz for backbone amide groups). The chemical shift evolves (indirect dimension) on the nitrogen and the magnetization is then transferred back to the hydrogen for detection.

Using heteronuclear (^1H - ^{15}N , ^{15}N - ^{13}C , ^1H - ^{13}C) and homonuclear (^{13}C) coupling constants, magnetization can be transferred through the backbone and CB atoms, within and across sequential residues i and $i-1$. The assignment is performed using 2D ^1H - ^{15}N HSQC (and ^1H - ^{13}C HSQC) experiments coupled to three-dimensional (3D) triple resonance (^1H , ^{13}C and ^{15}N) experiments. The assignment strategy consists in using complementary pairs of experiments that show on the one hand, correlations between residues i and $i-1$, and on the other hand, intra-residue correlations (Fig. 24).

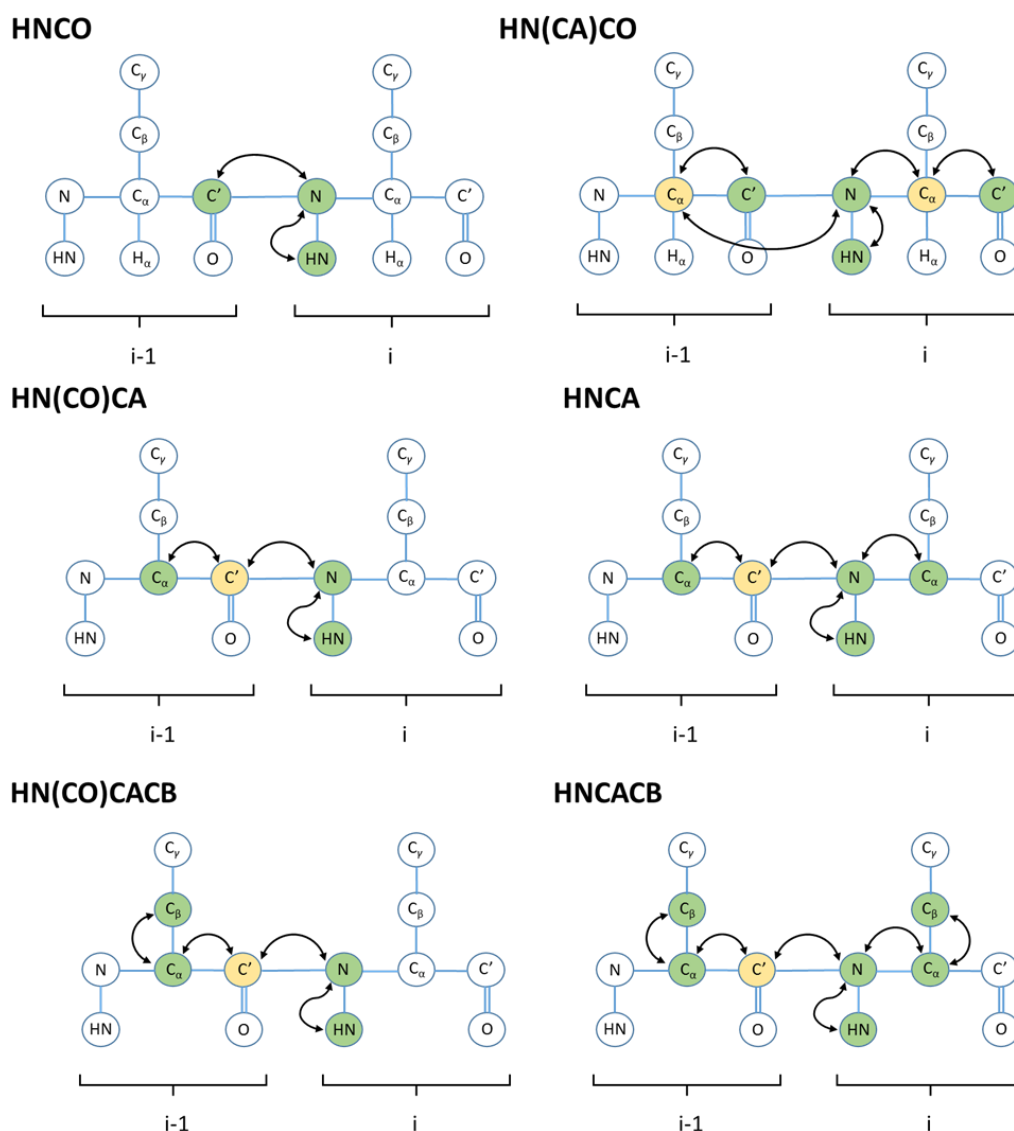


Fig. 24. Complementary pairs of triple resonance experiments for backbone assignment.

HNCO and HN(CA)CO; HN(CO)CA and HNCA; HN(CO)CACB and HNCACB. Observed nuclei are colored in green, while nuclei used to transfer magnetization but are not observed in spectra are in yellow. The name of the experiments includes the nuclei through which the magnetization is transferred (in parenthesis if these are not observed) and the nuclei the experiment correlates. For example, in the HN(CO)CA experiment, the magnetization passes from ^1H to ^{15}N and then to $^{13}\text{C}'$. From here it is transferred to the ^{13}CA of the previous residue and the carbonyl chemical shift evolve during the evolution period. Magnetization is then transferred back via the $^{13}\text{C}'$ to the ^{15}N and then ^1H nuclei for detection. The chemical shift evolves for the ^1HN , the ^{15}NH and the ^{13}CA , but not for the $^{13}\text{C}'$.

MATERIALS & METHODS

Using the three complementary pairs shown in Fig. 23, all the backbone and CB atoms of a spin system (intra-residue) and the previous one in the sequence are determined, for each residue. Matching the resonance frequencies of contiguous spin systems leads to the identification of coupled spin systems as shown in Fig. 25 with an example using the HNCO and HN(CA)CO experiments. This experiment allows the identification of the resonances belonging to the HN, N and C' carbonyl group from residue at position i and the previous one at position $i-1$

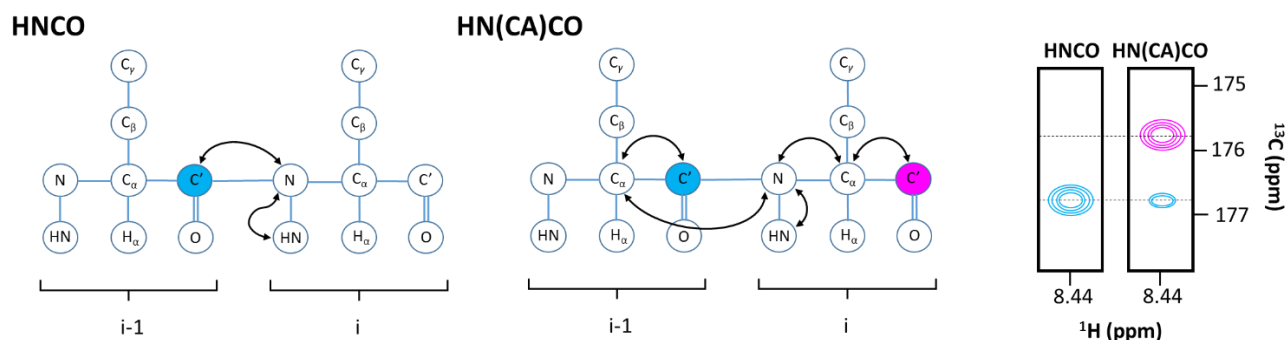


Fig. 25. Example of contiguous spin systems assignment with a set of two complementary sequences.

Left, the HNCO and HN(CA)CO correlations and magnetization transfer pathways. The blue color depicts residue $i-1$ and the pink residue i atoms and correlations. Right, 2D strip projection of both experiments at the ^{15}N frequency of the amide nitrogen of residue i . The x-axis corresponds to the proton dimension and the y-axis to the carbon one. In the HNCO, only the HN–C' correlation between the HN of residue i and the C' of residue $i-1$ is observed, while in the HN(CA)CO the correlation with the spin system $i-1$ and i carbonyl carbons are observed.

Following this strategy for all the amide groups, one can assign segments of contiguous spin systems. Because, different residues show different types of CA and CB chemical shifts, segments of spin systems can be matched with segments of residues in the protein sequence, ultimately leading to the complete sequential assignment of the backbone and CB resonances.

The next step in the assignment process is to assign the side chain, ^1H and ^{13}C , resonances to the corresponding atoms. This is mainly done through experiments that correlate the amide group signals of residue i with the side-chain ^1H [H(CC-TOCSY)NNH] or ^{13}C resonances [C(CCTOCSY)NNH] of residue $i-1$, or with residue i (^1H - ^{15}N HSQC-TOCSY, HNHA). The assignment to a specific residue is readily done because of the available assignment of the HN resonances. Assignment of the side chain resonances helps to confirm or assign new backbone

resonances. Another helpful 3D experiment for intra-residue side-chain proton assignment is HCCH-TOCSY, which correlates all aliphatic protons of a residue and benefits from the chemical shift dispersion on the ^{13}C dimension. Finally, aromatic protons are linked to the attached carbons through the ^1H - ^{13}C HSQC experiment and to their corresponding aliphatic side-chains through the 2D ^1H - ^{13}C (HB)CB(CGCD)HD and (HB)CB(CGCDCE)HE experiments that correlate the aromatic HD or HE proton signals to the aliphatic CB resonances, respectively.

2.4.2 Assignment of NMR backbone chemical shifts of RodC

We prepared a RodC sample at a final concentration of 0.6 mM in 50 mM CD_3COONa pH 4.5 and 10% D_2O .

RodC experiments were run at 45 °C and recorded on 600-MHz or 800-MHz (Avance Neo, Bruker) proton resonance frequency spectrometers equipped with cryogenically cooled probes. Spectra were recorded using TopSpin 3.5.7 or 4.0 (Bruker), processed with NMRPipe (Delaglio *et al.*, 1995) and analyzed with CCPNMR analysis 2.4.2 (Vranken *et al.*, 2005).

Backbone and CB atoms of RodC resonances were assigned from ^{15}N - ^1H HSQC, HNC(O), HN(CO)CA, HNCACB, CBCA (CO)NH and HNHA experiments following standard procedures as published in Pham *et al.*, 2018.

2.4.3 Secondary structure calculation

The secondary structure was predicted using the TALOS-N algorithm (Berjanskii and Wishart, 2005) from experimental chemical shifts (H, N, CO, CA, CB and HA) as described in (Pham *et al.*, 2018). The TALOS-N (Torsion Angle Likelihood Obtained from Shifts) algorithm is based on the secondary structure information contained in backbone atom chemical shifts to predict torsion angles. The algorithm extensively uses neural networks to search for the best matches of chemical shifts and residue types (tripeptides) within a database of high-resolution XR structures and corresponding chemical shifts. To avoid predicting torsion angles for very flexible regions of proteins, TALOS-N uses the random coil index method developed by Berjanskii and Wishart (Berjanskii and Wishart, 2005), which predicts dynamics on the picosecond nanosecond time scale from chemical shifts.

2.5 Amyloid formation followed by ThT fluorescence

The fluorescence properties of the amyloid reporter dye ThT are modified when it selectively binds the cross- β structure of amyloid fibers. Although there can be false negatives and false positives, ThT fluorescence represents the most convenient way to follow the kinetics of amyloid formation (Biancalana and Koide, 2010; Xue *et al.*, 2017).

Lyophilized monomer protein samples were solubilized in the appropriate buffer, centrifuged 15 min at 17000 g and filtered (0.22 μ) to eliminate possible aggregates. Centrifugation and filtering were done for all samples arising from lyophilized monomers for kinetics, fiber formation, ATR-FT-IR, etc.).

Experiments were performed using black 96-well flat-bottom plates (Greiner) and read on a SAFAS Monaco Xenius XC fluorimeter with controlled temperature. The excitation wavelength was followed at $\lambda = 415$ nm and emission at $\lambda = 484$ nm, both with 10-nm slits.

Although we tested different experimental conditions, in general, samples were incubated at 40 °C for RodA and RodB and 50 °C for RodC, RodC mutants and peptides. In order to increase the AWI and trigger amyloidogenesis, plates were thoroughly shaken at 720 rpm (orbital shaking) for 1 minute (RodA and RodB) or 3 minutes (RodC) between readings unless stated otherwise (Fig. 26). Assays were performed in 20 mM sodium acetate pH 5.0 buffer supplemented with 40 μ M ThT and wells were filled with 100 μ L unless stated otherwise. Protein concentrations were estimated with the BCA assay (Bio-Rad) calibrated with BSA, and knowing the conversion factor between BSA and hydrophobin concentrations.

MATERIALS & METHODS

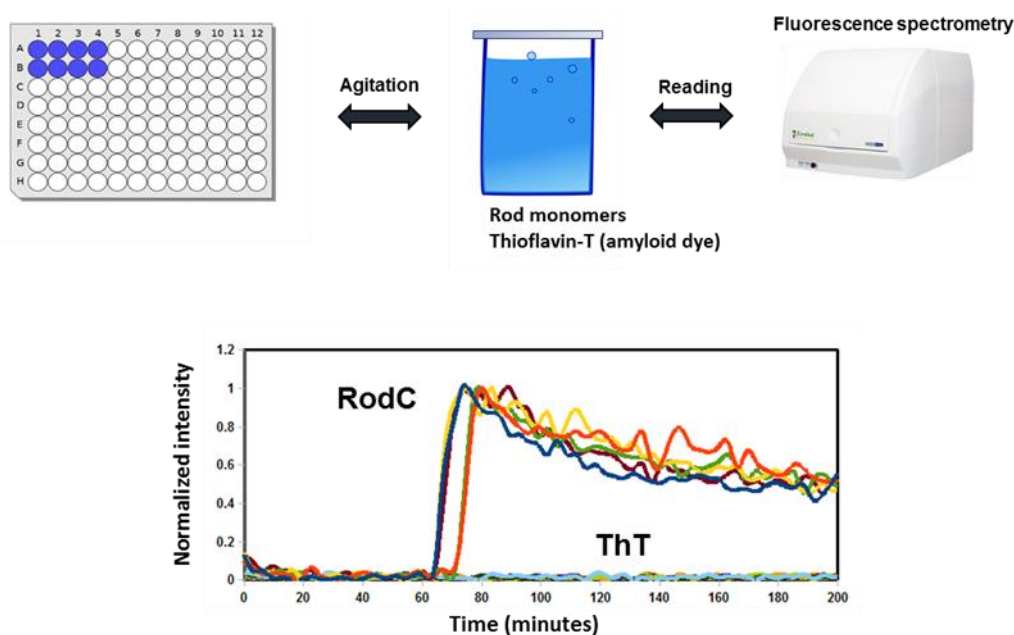


Fig. 26. Amyloid formation followed by ThT fluorescence

Top: Outline showing the protocol to follow amyloid formation. Samples are deposited in plates and incubated under thorough mixing. Bottom: Example of a kinetics experiment of RodC followed by ThT binding. The fluorescence intensity of ThT alone is weak and constant over time, while in the presence of RodC the fluorescence shows a sigmoidal shape with an increase of intensity upon fiber formation.

2.5.1 Effect of RodC point mutations on the fibrillation process

The importance of specific residues in fiber formation can be tested following the effect of point mutations in fibril kinetics formation. Finding several neighboring residues that have an effect on fiber formation can indicate that the corresponding region is involved in the cross- β core of the fibers. ThT fluorescence experiments were performed as explained above.

Thirteen single point mutations along the RodC sequence were designed and tested. Mutations were done on hydrophobic residues and included predicted amyloidogenic as well as non-amyloidogenic regions. Simple and multiple mutations were substitutions of a particular residue to glycine (X \rightarrow G) (Fig. 27).

MATERIALS & METHODS



Fig. 27. RodC sequence with the single point mutations.

The recombinant RodC sequence consists of 134 aminoacids corresponding to residues 16-153 of RodC plus an N-terminal Ser residue arising from cloning. The eight cysteine residues are in bold and numbered. The predicted amyloidogenic regions are underlined, and the 13 single point mutations are highlighted in grey (Y49G, L61G, I74G, L75G, V87G, P88G, V89G, V90G, L91G, L92G, V123G, L125G, I128G).

2.5.2 Effects of cell wall components on amyloid formation

In order to study whether major cell wall (MCW) components (polysaccharides and melanin) of the conidial cell wall have an effect on the amyloid formation of the hydrophobins, we performed kinetics experiments of RodC fiber formation in the presence of these compounds and followed the reaction by ThT fluorescence.

The MCW polysaccharides used to characterize the self-assembly of RodC were extracted and purified from *A. fumigatus* conidia by Vishukumar Aimanianda (*Aspergillus* Unit & Molecular Mycology Unit, Institut Pasteur): α -(1,3)-glucan, β -(1,3)-glucan and chitin. Laminarin, a soluble storage glucan from algae consisting of β -1,3-glucan with β -1,6-glucose branches and glucose were purchased from Sigma-Aldrich.

To mimic melanin, we prepared synthetic melanin by *in vitro* oxidation of its precursor in *A. fumigatus*: 1,8-dihydroxynaphtalene (DHN) (Sigma-Aldrich). DHN was dissolved at 0.9 mg/mL in 50 mM sodium bicarbonate pH 11.0 and incubated at 50 °C for 4 hours under constant shaking at 1200 rpm. Melanin was buffer-exchanged against water by repeated cycles of ultracentrifugation at 2.75 bar on an Airfuge (Beckmann).

RodC (25 μ g/mL) was incubated in the presence of each compound at 50 °C in 50 mM CH₃COONa pH 5.0 under continuous shaking (3 minutes orbital shaking at 720 rpm between reads). Chitin, α -(1,3)-glucan, β -(1,3)-glucan, glucose and laminarin were tested at 300, 500 and 750 μ g/mL whereas we used lower concentrations of DHN-melanin (100, 125 and 150

$\mu\text{g/mL}$) because of the high absorbance of this black pigment. Kinetics were performed in triplicate for each compound.

2.6 Synchrotron radiation circular dichroism spectroscopy of hydrophobins

Synchrotron radiation circular dichroism (SRCd) spectroscopy extends the utility of conventional CD spectroscopy because the high intensity of the light beam from a synchrotron enables collection of data to lower wavelengths ($< 190\text{ nm}$), the detection of spectra with higher signal-to-noise levels and less interference from salts, buffers, lipids and detergents (Wallace, 2009). The information content of CD at lower wavelengths is very interesting when studying β -structures because it allows the differentiation between parallel and anti-parallel β -sheets and detect twisted β -sheets (Micsonai *et al.*, 2015).

To study their assembly process, we recorded spectra of native monomer protein samples, of self-assembled rodlets formed in solution prior to the experiment and we investigated the changes in secondary structure of the native monomers upon heating. We performed temperature scans from $25\text{ }^\circ\text{C}$ to $94\text{ }^\circ\text{C}$ in $3\text{ }^\circ\text{C}$ steps, heating at $0.6\text{ }^\circ\text{C}/\text{min}$ and with one or two scans recorded per $3\text{ }^\circ\text{C}$ step.

To estimate the secondary structure content of the corresponding proteins we used the BeStSel (beta structure selection) algorithm specially conceived for SRCd data (Micsonai *et al.*, 2015).

2.7 Fourier-transform infrared spectroscopy

This technique is based on the measurement of the molecular bond vibration of molecules. Sample is shot with infrared radiation and its absorption stimulates vibrational motions. These vibrations can be quantitatively measured to obtain a fingerprint of the compound chemical structure (Baker *et al.*, 2014).

In biological samples, the most important regions of the spectrum are the amide I ($1500\text{-}1700\text{ cm}^{-1}$) and the amide II ($1600\text{-}1450\text{ cm}^{-1}$) regions (Fig. 28).

MATERIALS & METHODS

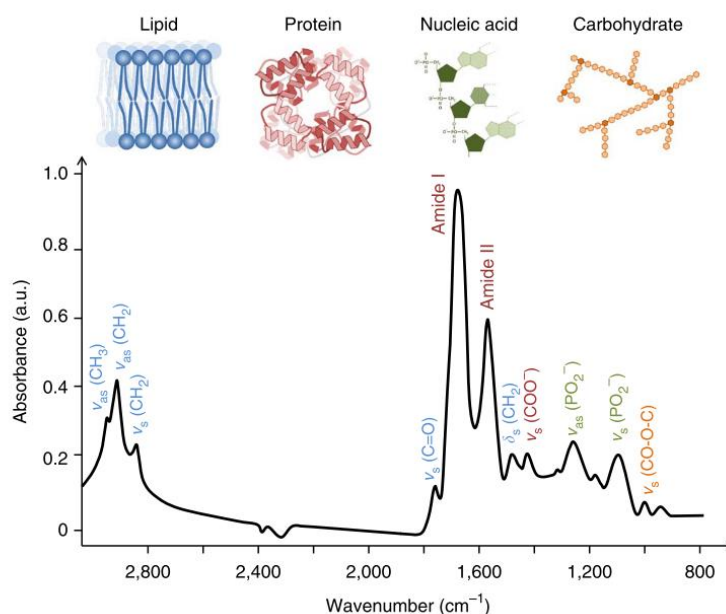


Fig. 28. Fourier-transform infrared spectroscopy example spectrum.

Typical biological sample spectrum with the peak assignments between 3000-800 cm⁻¹. ν = stretching vibrations, δ = bending vibrations, s = symmetric vibrations and as = asymmetric vibrations (extracted from Baker *et al.*, 2014).

In particular for proteins, the amide I band contains information on the backbone secondary structure as the vibrations depend on the backbone conformation.

There are three different IR spectroscopic sampling modes: Transmission, transfection and attenuated total reflection. We used the attenuated total reflection (ATR) mode that allows a continuous structural view of protein/peptide conversion during the aggregation process. Using this approach, samples can be soluble or insoluble, which is necessary to study the self-assembly and the aggregates formed (fibers, films, aggregates) (Sarroukh *et al.*, 2013; Baker *et al.*, 2014).

To study the conformational changes of hydrophobins upon assembly, we recorded spectra from lyophilized monomeric hydrophobins and rodlet forms. We also performed temperature ramp ATR FT-IR experiments starting with monomeric forms of hydrophobins. Lyophilized monomers were solubilized in the appropriate buffer, filtered (0.22 μm) and investigated during heating from 25 °C to 94 °C in 3-degree. Every protein was tested by triplicate.

2.8 Transmission electron microscopy

Transmission Electron Microscopy (TEM) of negatively stained or cryo-prepared specimens allows amyloid fibers to be visualized in a dried or a hydrated state, respectively. It is a very useful technique to check morphology. While negative staining offers good contrast, the resolution is low and drying the sample can induce morphological changes. On the other hand, cryo-TEM uses samples frozen in H₂O, much closer to native conditions and allows one to obtain higher resolution. Both methods are very useful coupled with other techniques to obtain qualitative data (Gras, Waddington and Goldie, 2011).

We have used negative stain TEM to study the morphology of the self-assemblies of hydrophobins after different experiments (e.g. kinetics, FT-IR, SRCD) and to check the morphology of mutants and peptides. Typically, in these experiments, 4 μ L of sample (at 200 or 400 μ g/mL) were placed on a carbon coated copper grid (300 mesh, CF300-CU, Electronic Microscopy Sciences) and incubated for 2 min at room temperature. Grids were glow discharged beforehand (2 mA, 1 min) to make the grid surface negatively charged and hydrophilic. In all cases, samples were stained with (2 %) uranyl acetate on the grids.

Experiments were performed on a Tecnai -T12 (120 Kv, FEI) transmission electron microscope at the UBI platform of the Institut Pasteur with the help of Gérard Péhau-Arnaudet.

2.9 Atomic force microscopy

Atomic force microscopy (AFM) allows three-dimensional topographic measurement of surface roughness within nanoscale resolution. It is a scanning microscope based on mechanical forces in which the sharp tip interacts with the atoms of the sample surface (Vahabi, Nazemi Salman and Javanmard, 2013).

This technique was first developed for material science but is widely used in biology. It is commonly used to study amyloid morphology and has been applied to study phenotypic characteristics of mutant strains with altered cell-wall constituents, for example *A. fumigatus* Rod mutants or hydrophobin assembly (Dufrière, 2008; Valsecchi *et al.*, 2018; Valsecchi *et al.*, 2019a).

Hydrophobin and peptide samples were prepared from lyophilized material dissolved in H₂O. Four μ L of samples at 5 μ g/mL were deposited on mica or HOPG (highly oriented pyrolytic graphite), dried at room temperature overnight and further dried 2 h at 70°C. Samples were

MATERIALS & METHODS

prepared either from monomers, or from proteins that were self-assembled in H₂O by vigorous shaking at 40°C (RodA, RodB) or 50°C (RodC) monomer samples (25 µg/ml). To test the effect of cell wall polysaccharides on hydrophobin assembly, the polysaccharides, or melanin were first dried on mica or HOPG and then hydrophobins were applied and dried as above.

AFM experiments were conducted by Vincent Duprès (Institut Pasteur de Lille) in ScanAsyst mode in air using a Nanoscope 8 MultiMode AFM equipment (Bruker, Santa Barbara, CA) and ScanAsyst-Air cantilevers.

Results & Discussion

3 Results & Discussion

3.1 Chapter 1: Manuscript. Probing structural changes during self-assembly of surface-active hydrophobin proteins that form functional amyloids in fungi

3.1.1 Introduction

With the aim of understanding the secondary structure conformational changes associated with rodlet formation of hydrophobins, we decided to work with six hydrophobins from four different fungal species. The proteins EAS (*N. crassa*), MPG1(*M. grisea*) and RodA (*A. fumigatus*) self-organize into rodlet layers that cover the spores of the respective fungal spores providing hydrophobicity. The protein DewA (*A. nidulans*), as well as RodB and RodC (*A. fumigatus*), are present in the spore cell wall but are not implicated on the outer rodlet layer. For practical reasons, modified recombinant versions of EAS (EAS Δ 15) and DewA (DewY) known to form rodlets as the corresponding WT proteins were used in the study.

We used different biophysical techniques (NMR, SRCD, FT-IR and EM) to study the self-assembly of the six hydrophobins under different conditions and with different surfaces to characterize the structural changes and the influence of the interface upon auto-association. This work is summarized in the accompanying paper (and its Supplementary Material) that appeared in a special issue of the *Journal of Molecular Biology* dedicated to functional amyloids.

3.1.2 Framework and objective

During years people have been trying to understand the self-assembly process within biological systems. This is a key process in important diseases such as Alzheimer's or Parkinson's to form the amyloid plaques during the disease development. Furthermore, this process is present not only in biological systems, but also in material and physics science.

It has been shown that fungi are able to form functional amyloids from hydrophobin proteins that self-assembly to form fibers that can also associate in a rodlet structure. It is known that the biological role of the assembled form cannot be provided by monomeric form thus the

understanding of the assembly process is of big interest. During the last years many efforts have been focused on the study of the soluble form and the fiber structure but not on the assembly process. Therefore, in this paper we wanted to better understand the secondary structural changes that occur upon assembly of hydrophobins by different biophysical approaches and on different surfaces.

We have studied 6 class I hydrophobins: MPG1, DewY, EAS Δ 15, RodA, RodB and RodC in its monomeric form by NMR and SRCD. Then, we investigated the effect of HHI upon heating (it is known that hydrophobins need an interface that triggers assembly) and on different type of surfaces by SRCD and FT-IT.

Manuscript



Probing Structural Changes during Self-assembly of Surface-Active Hydrophobin Proteins that Form Functional Amyloids in Fungi

Chi L.L. Pham^{1,†}, Borja Rodríguez de Francisco^{2,†}, Isabel Valsecchi², Régine Dazzoni², Ariane Pillé², Victor Lo¹, Sarah R. Ball¹, Roberto Cappai³, Frank Wien⁴, Ann H. Kwan⁵, J. Iñaki Guijarro² and Margaret Sunde¹

1 - Discipline of Pharmacology, School of Medical Science and Sydney Nano, University of Sydney, NSW 2006, Australia

2 - Biological NMR Platform, Institut Pasteur CNRS UMR 3528, 75015 Paris, France

3 - Department of Pharmacology and Therapeutics, School of Biomedical Sciences, The University of Melbourne, Parkville, VIC 3010, Australia

4 - DISCO Beamline, Synchrotron SOLEIL, 91192 Gif-sur-Yvette, France

5 - School of Life and Environmental Sciences and Sydney Nano, University of Sydney, NSW 2006, Australia

Correspondence to Ann H. Kwan, J. Iñaki Guijarro and Margaret Sunde: margaret.sunde@sydney.edu.au
<https://doi.org/10.1016/j.jmb.2018.07.025>

Edited by Sven J Saupe

Abstract

Hydrophobins are amphiphilic proteins secreted by filamentous fungi in a soluble form, which can self-assemble at hydrophilic/hydrophobic or water/air interfaces to form amphiphilic layers that have multiple biological roles. We have investigated the conformational changes that occur upon self-assembly of six hydrophobins that form functional amyloid fibrils with a rodlet morphology. These hydrophobins are present in the cell wall of spores from different fungal species. From available structures and NMR chemical shifts, we established the secondary structures of the monomeric forms of these proteins and monitored their conformational changes upon amyloid rodlet formation or thermal transitions using synchrotron radiation circular dichroism and Fourier-transform infrared spectroscopy (FT-IR). Thermal transitions were followed by synchrotron radiation circular dichroism in quartz cells that allowed for microbubbles and hence water/air interfaces to form and showed irreversible conformations that differed from the rodlet state for most of the proteins. In contrast, thermal transitions on hermetic calcium fluoride cells showed reversible conformational changes. Heating hydrophobin solutions with a water/air interface on a silicon crystal surface in FT-IR experiments resulted in a gain in β -sheet content typical of amyloid fibrils for all except one protein. Rodlet formation was further confirmed by electron microscopy. FT-IR spectra of pre-formed hydrophobin rodlet preparations also showed a gain in β -sheet characteristic of the amyloid cross- β structure. Our results indicate that hydrophobins are capable of significant conformational plasticity and the nature of the assemblies formed by these surface-active proteins is highly dependent on the interface at which self-assembly takes place.

© 2018 Elsevier Ltd. All rights reserved.

Introduction and Background

Filamentous fungi produce and secrete small amphipathic proteins, known as hydrophobins, which are important in modulating the interactions between these fungi and their environments [1]. Hydrophobins have the capacity to spontaneously self-assemble at hydrophobic/hydrophilic interfaces (HHIs) to form amphipathic layers. The layers of some hydrophobins, known as class I hydrophobins, consist of robust

fibrillar structures known as rodlets, which have an underlying cross- β amyloid structure. Class II hydrophobins self-assemble into amphipathic layers that lack the fibrillar amyloid structure, while some other hydrophobins with more diverse sequence have been described but have never been studied experimentally [2,3].

Class I hydrophobin rodlets are found on the surface of fungal spores and may also play important roles during the fungal life cycle, including during infection

and growth within the host [1]. The outer face of the rodlet layer is hydrophobic and resists wetting. The layer facilitates adhesion to waxy surfaces such as plant leaves in the case of plant pathogens [4,5] and, in animal hosts, serves to protect fungal spores from immune detection [6]. Hydrophobin rodlets are functional amyloids, where the self-assembled amyloid form of the protein imparts a biological role that is not provided by the monomeric form.

We have chosen to study six class I hydrophobins (MPG1, DewY, EAS $_{\Delta 15}$, RodA, RodB and RodC) from four different fungal species. MPG1 is expressed by the plant pathogen *Magnaporthe oryzae*. This fungus causes rice blast, the fungal infection responsible for loss of up to one third of the global annual rice crop [7]. MPG1 forms the hydrophobin rodlets that cover the surface of *M. oryzae* spores. Expression of MPG1 is associated with attachment of the fungal spore to the leaves of the rice plant, hyphal growth and development of the appressorium [5]. DewA is expressed in the spores of *Aspergillus nidulans*, but this hydrophobin does not form the outer rodlet coating on spores, which is composed of the *A. nidulans* hydrophobin RodA. In this work, we have used DewY, a protein that is structurally identical to DewA but that carries two introduced mutations to the wild-type sequence, within the flexible N-terminal and C-terminal regions (A4Y and T114Y), to facilitate protein concentration determination by UV absorbance measurements [8]. DewY and DewA share the same fold in solution according to ^1H 1D NMR spectroscopy (Supplemental Fig. S1). EAS $_{\Delta 15}$ is a truncated form of the hydrophobin EAS, which coats the surface of *Neurospora crassa* spores and protects them from wetting. EAS $_{\Delta 15}$ has similar assembly properties to EAS [9]. Three class I hydrophobins that are present on the spores of the airborne human pathogenic fungus *Aspergillus fumigatus* have also been included [10]. RodA from *A. fumigatus* forms the non-immunogenic rodlet coating on the outer surface of the spores [6], and RodB is highly expressed during infection, while the role of RodC is not yet understood [11]. The six hydrophobins we have studied are all from Ascomycetes and are therefore members of the class Ia subgroup of hydrophobins, which display more variability in sequence and inter-cysteine lengths, even than the class Ib subgroup from Basidiomycetes [12]. While RodA, RodB and RodC from *A. fumigatus* are close homologues, sharing over 36% of sequence identity (excluding cysteines) in the region between the first and eighth cysteine residues, DewA, EAS and MPG1, display high sequence and inter-cysteine spacing variability relative to each other and to the three *A. fumigatus* hydrophobins. For example, DewA shows only 17.6%, 4.2% and 11.5% identity to EAS, MPG1 and RodA, respectively. This contrasts with the higher level of sequence identity between class Ib hydrophobins, which includes SC3 (*Schizophyllum commune*), Vmh2 (*Pleurotus ostreatus*) and ABH1

(*Agaricus bisporus*), with SC3 showing 43.8 and 31.5% sequence identity with Vmh2 and ABH1, respectively.

The ability of hydrophobin rodlet layers to reverse the wettability of surfaces and to assemble into robust, non-immunogenic and biocompatible coatings on multiple surfaces has led to significant interest in the application of these proteins for biotechnological and biomedical applications [13]. For instance, variants of DewA have been applied in implant [14] and stent coatings [15]. The effective use of hydrophobins for such purposes requires an understanding of the structure of class I hydrophobins in the monomeric and rodlet forms and the ability to control or tune the self-assembly process. We have therefore carried out a study of the structural changes that occur in six different class I hydrophobins upon self-assembly.

The three-dimensional structures of the monomeric forms of MPG1, DewA, EAS $_{\Delta 15}$ and RodA have previously been determined in solution by NMR [4,8,9,16] and I. Valsecchi et al. (in preparation). These four hydrophobins share a distinctive, constrained β -barrel or half β -barrel structure that is a consequence of the unique pattern of disulfide bonding characteristic of all hydrophobins [17]. The structures of the monomeric forms of RodB and RodC are not yet available; however, sequence analysis and NMR data presented herein indicate that they have a similar fold. EAS is one of the most well-characterized hydrophobin, and the rodlet form of EAS $_{\Delta 15}$ has been studied by solid-state NMR and is consistent with the formation of a cross- β amyloid core structure when the protein self-assembles [18].

Unlike the hydrophobin SC3, which can assemble into nanorods in solution [19], and the hydrophobin Vmh2, which forms amyloid fibrils in solution in a process influenced by pH, temperature and calcium ions [20], the hydrophobins included in this study require the presence of a HHI to trigger self-assembly into amyloid-structured rodlets from aqueous solutions. We have previously demonstrated this for MPG1 [4], DewY and EAS $_{\Delta 15}$ [21] and now show this is also true for RodA, RodB and RodC from *A. fumigatus*. Conditions including pH, temperature, protein concentration and presence of surface tension modulators affect the kinetics of assembly of amyloid-structured hydrophobin rodlets [4,21,22]. In this study, we focus on conformational change in the presence of a HHI in order to generate mechanistic information about the process of hydrophobin self-assembly.

We have applied synchrotron radiation circular dichroism (SRCD) spectropolarimetry and attenuated total reflection (ATR) Fourier-transform infrared (FT-IR) spectroscopy to study the structural changes that occur when different hydrophobin proteins interact with surfaces or self-assemble into the functional amyloid rodlet form. The assembled forms have been imaged by transmission electron microscopy. The monomeric and polymerized forms of MPG1, DewY, EAS $_{\Delta 15}$,

RodA, RodB and RodC have been studied by SRCD and FT-IR to assess the secondary structure of the proteins and conformational changes during self-assembly. SRCD has several advantages over conventional bench-top CD, providing a significant extension in the spectral range, an improved signal-to-noise ratio, less interference arising from light scattering and the ability to collect spectra from proteins in a wide range of solution conditions [23,24]. The extension of the spectral range to the lower wavelengths, along with improvements in signal-to-noise ratio, is particularly helpful for delineating the different types of β -structures found in proteins and macromolecular assemblies such as amyloid fibrils and discriminating between parallel and anti-parallel β -sheet with left, right or no twist (i.e., relaxed state). SRCD has recently been used to characterize a number of proteins that form amyloids and to monitor the secondary structure changes during the amyloid formation process [24–26]. FT-IR can provide information regarding the secondary structure of proteins in insoluble forms and in solution, and therefore provides an additional complementary capacity for the assessment of the β -structure in the monomeric and amyloid forms of hydrophobins.

Results and Discussion

SRCD analyses of hydrophobins in solution reflect the characteristic hydrophobin β -barrel monomer structures, with a significant amount of irregular structure combined with right-hand twisted antiparallel β -sheets

SRCD spectra were collected from the monomeric forms of the six hydrophobins in solution under standard conditions (25 °C, atmospheric pressure) using a quartz glass cell. The data were processed using *CDtool* [27] and spectral fitting was performed with BeStSel [24], using a linear combination of eight structural components that provided close agreement with experimental data (Fig. 1). The SRCD results are consistent with the shared hydrophobin fold in all hydrophobins, which comprises a small β -barrel core structure decorated by ordered and disordered loop regions [28] (Fig. 2). A key feature of the BeStSel analysis was the identification of a substantial proportion (between 42% and 51%) of the structural composition of all of the hydrophobins as “Others,” a category that represents β -bridge, bends, loop/irregular, 3_{10} and π -helix components (Table 1). This likely reflects the unusual structural constraints imposed by the arrangement of the four disulfide bonds in the hydrophobins, which link β -strands together and generate multiple inter-cysteine loops. The next largest category of secondary structure was β -sheet, with the total β -content ranging from 20% to 31%. The SRCD data fitting indicates that effectively all of the β -sheets

present in hydrophobins are antiparallel, consistent with the hydrophobin structures solved to date. BeStSel further distinguishes antiparallel β -sheets into three subgroups: left-hand twisted, relaxed and right-hand twisted (termed anti1, anti2 and anti3, respectively). The anti3 component is predominant in all six hydrophobins. In some cases, small amounts of α -helical structural elements are predicted by BeStSel, which are not consistent with the determined structures. For example in the case of EAS $_{\Delta 15}$, BeStSel fitting predicts an α -helical component (10%) that is not observed in the NMR structure (Table 1).

The BeStSel secondary structure component estimations from SRCD data were compared to the secondary structures of the six hydrophobins predicted from backbone and CB chemical shifts using data deposited with the BMRB database (for MPG1, EAS $_{\Delta 15}$, DewY, RodA) or determined here (RodB and RodC) (Table 1 and Fig. 2). For MPG1, EAS $_{\Delta 15}$, DewY and RodA, the secondary structure was also estimated from the PDB coordinates using the BeStSel and DSSP algorithms [24,30]. These four hydrophobins show a common central antiparallel β -barrel or half β -barrel stabilized by two disulfide bridges between cysteines C3–C4 and C7–C8 (numbering of cysteine residues corresponds to their order of appearance in the sequence; this convention is used throughout this work) (Fig. 2). The two other disulfide bridges (C1–C6 and C2–C5) connect cysteine residues within the β -barrel with regions flanking the β -barrel (Fig. 2). Outside the β -barrel, the secondary structure of these hydrophobins shows more variability. The NMR chemical shift-derived and the 3D structure-derived secondary structures are, in general, in very good agreement. The main differences are mostly observed at the ends of the α -helices and β -strands and in some short helical elements that are not captured by the TALOS-N algorithm. As with MPG1, EAS $_{\Delta 15}$, DewY and RodA, the chemical shift-derived secondary structures of RodB and RodC show β -strands in the vicinity of cysteines C2 to C8, suggesting that the 3D structures of both proteins also contain a central β -barrel. We have previously shown that recombinant RodA adopts the same cysteine pairing and structure as the native protein extracted from the fungal spores and used NMR-derived data (nOes) to determine the topology of the native protein [16], which corresponded to the established idiosyncratic pattern observed in hydrophobins. Because the hydrophobin proteins are refolded *in vitro*, it is important to ensure that the correct S–S pairing is obtained. Given the high-sequence similarity of RodA, RodB and RodC, the similarity in secondary structural elements in the regions of the eight cysteines, the topology of antiparallel β -strands observed for RodA, and the observation that all cysteine residues in RodB and RodC are oxidized and show the same pattern of highly shifted CB chemical shifts as RodA (see below), we can conclude that RodB and RodC adopt the same S–S pairing and

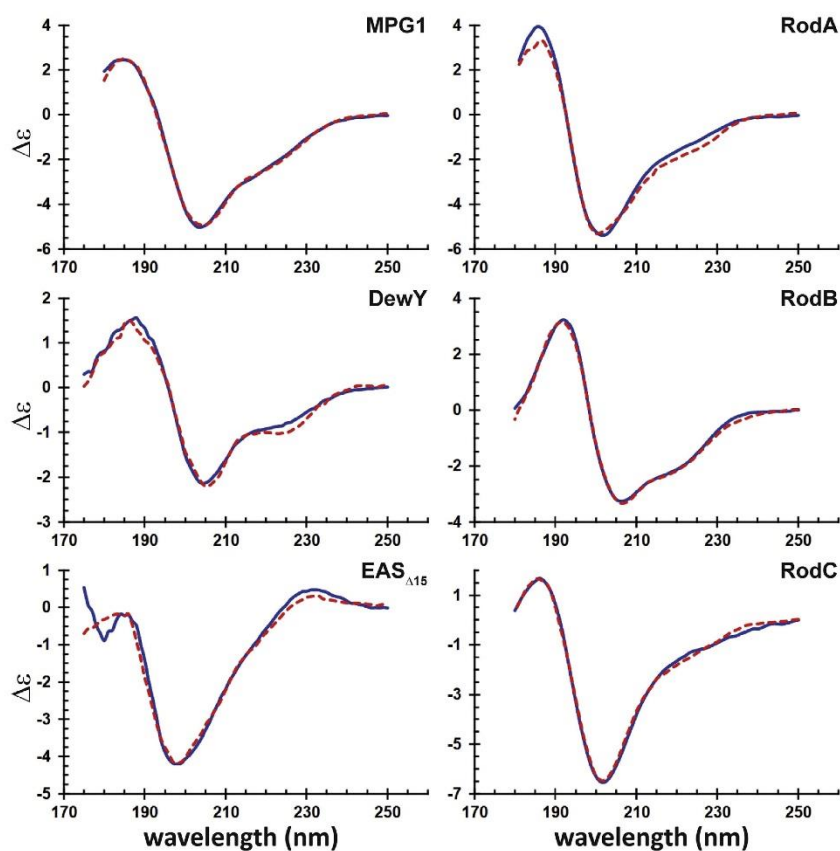


Fig. 1. SRCD spectropolarimetry of monomeric hydrophobins. The recorded experimental spectra (solid line) were processed using *CDtool*[27] then fitted using BeStSel [24] (dashed line) to deconvolute the composition of secondary structure elements, as shown in Table 1. CD is expressed as residual molar circular dichroism ($\Delta\epsilon$, $M^{-1} \cdot cm^{-1}$). The spectra of the monomeric hydrophobins were collected twice with different samples, and a representative spectrum is shown for each protein.

a similar 3D structure to that of RodA. To summarize, except for $EAS_{\Delta 15}$, all the hydrophobins studied herein display a mixed α/β topology.

Generally, there is a good agreement (differences within $\sim 10\%$) for all secondary structure components estimated by the different methods. The estimations of helical structure are the most divergent. For DewA/Y, BeStSel analysis calculates 6% helical content from the SRCD data, while 17% is present in the NMR structure. However, the NMR structure was determined from the major DewA conformer 1 (DewA-1), while the minor and more disordered conformer 2 (DewA-2) may also be present in the CD sample and contribute to a lower combined helical signal [8]. The proportion of

structure judged as “Turn” and “Others” by the BeStSel and DSSP algorithms differs, presumably because of differences in the definition of these elements. Overall, the SRCD-BeStSel method gives a reliable estimation of secondary structure composition in the monomeric forms of the hydrophobins, including the subtypes of β -structural elements, that matches well with those observed in the NMR structures and/or established from chemical shifts.

Conformational changes in hydrophobins induced by heating in the presence of a HHI

Previous conventional CD studies have revealed that the hydrophobins EAS and SC3 undergo major

Table 1. Summary of the secondary structure composition obtained from BeStSel analysis of SRCD data and NMR structures, along with estimations obtained using the DSSP algorithm and chemical shift data (TALOS-N)

	Helix1 (regular)	Helix2 (distorted)	Alpha helix	Helix3 ₁₀	Total helix	Anti1 (left twisted)	Anti2 (relaxed)	Anti3 (right twisted)	Parallel	Total beta	Turn	Others
MPG1												
SRCD	12	10	–	–	22	0	2	17	2	20	14	44
NMR structure	3	13	–	–	16	3	2	13	0	18	14	52
SS_DSSP	–	–	14	3	17	–	–	–	–	18	26	39
TALOS-N	–	–	–	–	18	–	–	–	–	19	–	63
DewA/Y												
SRCD	0	6	–	–	6	1	10	15	0	26	18	50
NMR structure	3	14	–	–	17	2	3	19	0	24	17	42
SS_DSSP	–	–	17	0	17	–	–	–	–	22	35	26
TALOS-N	–	–	–	–	18	–	–	–	–	19	–	63
conformer 1 TALOS-N	–	–	–	–	5	–	–	–	–	14	–	81
conformer 2 TALOS-N	–	–	–	–	5	–	–	–	–	14	–	81
EAS_{Δ15}												
SRCD	4	6	–	–	10	0	7	24	0	31	16	43
NMR structure	0	0	–	–	0	0	5	33	0	38	12	50
SS_DSSP	–	–	0	0	0	–	–	–	–	37	28	35
TALOS-N	–	–	–	–	0	–	–	–	–	41	–	59
RodA												
SRCD	11	4	–	–	15	0	2	22	0	24	14	47
NMR structure	8	10	–	–	18	0	6	16	0	22	12	48
SS_DSSP	–	–	17	4	21	–	–	–	–	22	19	38
TALOS-N	–	–	–	–	13	–	–	–	–	19	–	68
RodB												
SRCD	11	8	–	–	19	2	9	14	0	25	14	42
TALOS-N	–	–	–	–	16	–	–	–	–	17	–	67
RodC												
SRCD	3	5	–	–	8	0	2	23	0	25	16	51
TALOS-N	–	–	–	–	5	–	–	–	–	19	–	76

The values in the table are percentages. The BeStSel algorithm assigns Helix3₁₀ to "Others" and the TALOS-N analysis distinguishes only between "Helix, Sheet and Others."

experiments as slight expansion of the cell during heating led to the formation of microbubbles throughout the hydrophobin solution and hence to the introduction of air/solution interfaces (inset to Fig. 3, RodA panel). The bubbles that were observed in the quartz cell at the end of the thermal transition experiments had a diameter of ~0.5–1 mm per bubble and resulted in a combined total area covering approximately half of the cell (inset to Fig. 3, RodA panel). In contrast, heating of a solution of RodA over the same temperature range in a tightly sealed calcium fluoride cell with a path length of 12 μm did not show the formation of microbubbles and did not result in significant changes in the recorded SRCD spectra (Supplemental Fig. S2).

The combination of heating and the formation of air/solution interfaces surrounding the bubbles led to conformational changes in the hydrophobins, indicated by alterations in the SRCD spectra (Fig. 3). For MPG1, DewY, EAS_{Δ15} and RodB, relatively large changes in the spectra were observed upon heating and the changes were irreversible, as judged by spectra collected after cooling the samples to 25 °C (Fig. 3, black dashed spectra). The change in circular dichroism signal at 205 nm with temperatures up to 94 °C, for

DewY, EAS_{Δ15} and RodB, indicates that the structural transitions induced by heating are complete over this temperature range. For MPG1, the structural transition was likely complete, although no clear plateau in the signal at 205 nm was observed, since the post-melt sample recorded at 25 °C indicated that the transition was irreversible and showed a very similar spectrum to the spectrum at 94 °C. These observations suggest that conversion of MPG1, DewY, EAS_{Δ15} and RodB to a different and irreversible form has occurred.

For RodA, a non-cooperative transition with structural changes was observed upon heating in the quartz cell, and when the solution was cooled from 94 °C to 25 °C, the post-melt spectrum did not resemble any of the other spectra in the temperature series. This unusual result suggests that heating under these conditions induces some structural changes in RodA but does not generate a single, stable assembled structure. Instead, heating allows the protein to access, and subsequently during cooling to fold into, an alternative low-energy structure. RodA did not undergo large conformational changes when heated in a calcium fluoride cell, indicating that the structure of this hydrophobin is highly dependent on the environment (Supplemental Fig. S2). RodC did not exhibit large changes in the

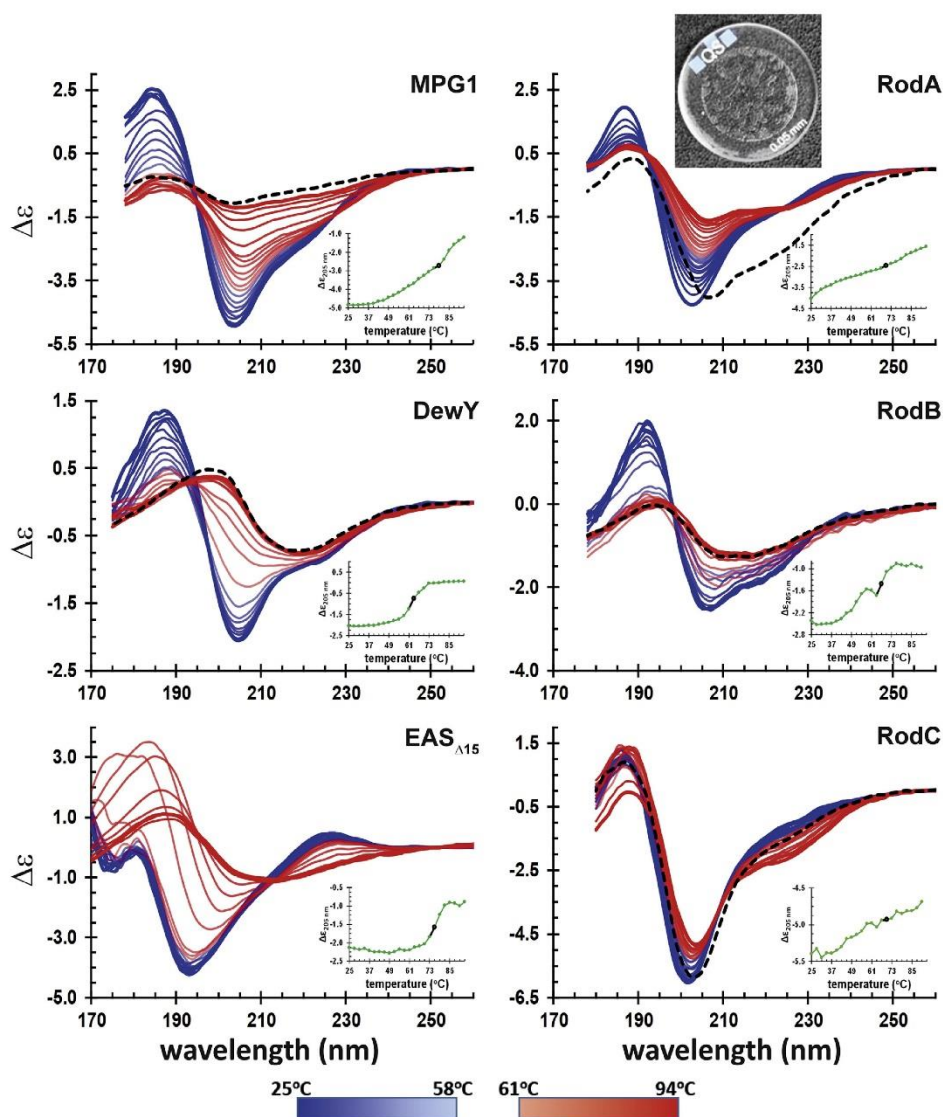


Fig. 3. Temperature-dependent conformational change of hydrophobins monitored by SRCD. Spectra were recorded from 25 °C to 94 °C in 3-degree steps, followed by cooling of the sample back to 25 °C (black dashed line). Photo inset in RodA panel shows the microbubbles formed in the quartz cell during the thermal transition experiments; it is representative of all samples where microbubbles were observed to form. Graphical insets show the change in $\Delta\epsilon_{205\text{nm}}$ with increasing temperature. The black symbol indicates the temperature at which the midpoint of the structural transition was observed for each hydrophobin. The secondary structure composition estimated at this temperature is shown in Table 2, between estimates from spectra collected at 25 °C and 94 °C. The thermal transition experiments were performed twice for EAS_{Δ15}, and the results from the two scans were comparable (one of which is shown here). Subsequent experiments with the other hydrophobins were performed once.

SRCD spectrum upon heating, showing that the protein does not appear to undergo major conformational change or assemble into a different stable form under these conditions.

Despite the spectra of MPG1, DewY, EAS_{Δ15} and RodB changing substantially as the temperature increased, analysis of the secondary structure of these hydrophobins using the BeStSel algorithm revealed that only relatively small changes in secondary structure content occurred with heating and introduction of HHIs. The total β-structure content did not change for EAS_{Δ15} and increased by only a small amount (6% for RodB) or a moderate amount (8%–9% for MPG1 and DewY), compared with the form of the protein populated at 25 °C in the absence of HHIs (Table 2). The small changes in β-structural content observed with the hydrophobins contrast to the relatively large changes seen with another amyloid-forming protein α-synuclein (Supplemental Fig. S3). The minor increases in β-structure content in the hydrophobins were accompanied by a relative shift from right-hand twisted to relaxed β-sheet content. For MPG1 and RodB, a large decrease in helical content occurred upon transition to the self-assembled form (by ~80% and ~50%, respectively). The observed

decrease in helical content was small for DewY (~20%); however, this estimate may be confounded by the low estimate of helical structure in the monomer by BeStSel and the population of a less structured conformation of the protein in the sample.

One explanation for the lack of a substantial increase in β-structure in the heated SRCD experiments is that the heating and bubble formation inside the SRCD cell have not resulted in conversion to the rodlet form, which is known to have an underlying amyloid cross-β structure arising from intermolecular association. Instead, the conditions have generated intermediate states with an irreversible change in protein conformation, which may be on pathway to rodlet formation. The particular hydrophobins included in this study require the presence of a HHI to trigger self-assembly into amyloid-structured rodlets. We have previously demonstrated this specifically for MPG1, EAS_{Δ15} and DewA with an assay that removed the HHI while maintaining agitation of the solution [4,21]. Although rodlet formation by EAS_{Δ15}, DewY and MPG1 occurs readily *in vitro* when a HHI is present and all molecules are exposed to HHIs by agitation of the solution or drying down of the solution, it is possible that the extent of the HHI in the SRCD cell or length of incubation time was not

Table 2. Summary of the secondary structure composition obtained from BeStSel analysis of SRCD data at 25 °C and 94 °C and at the temperature at which the structural transition midpoint was observed

	Helix1 (regular)	Helix2 (Distorted)	Total Helix	Anti1 (left twisted)	Anti2 (relaxed)	Anti3 (right twisted)	Total Anti	Parallel	Total Beta	Turn	Others
MPG1											
25 °C	12	10	22	0	2	17	19	2	21	14	43
79 °C	4	6	10	0	3	4	7	7	14	16	60
94 °C	2	3	5	3	11	11	25	4	29	18	48
Back to 25 °C	0	2	2	4	11	15	30	0	30	19	49
DewY											
25 °C	0	6	6	2	10	14	26	0	26	18	50
64 °C	4	5	9	4	12	13	29	1	30	16	45
94 °C	2	3	5	6	14	12	32	3	35	16	44
Back to 25 °C	1	3	4	6	15	14	35	1	36	16	43
EAS_{Δ15}											
25 °C	0	6	6	0	8	23	31	0	31	20	43
73 °C	1	5	6	0	7	21	28	0	28	22	44
94 °C	0	5	5	4	13	14	31	0	31	17	47
RodA											
25 °C	9	5	14	0	3	19	22	0	22	15	49
70 °C	6	6	12	1	7	10	18	6	24	16	48
94 °C	5	5	10	2	8	8	18	7	25	18	47
Back to 25 °C	5	11	16	0	0	0	0	7	7	14	63
RodB											
25 °C	10	6	16	2	7	8	17	5	22	15	47
67 °C	6	2	8	3	10	2	15	10	25	17	50
91 °C	4	3	7	4	13	4	21	7	28	18	47
Back to 25 °C	4	4	8	4	12	8	24	6	30	17	45
RodC											
25 °C	4	7	11	0	3	15	18	0	18	14	57
70 °C	6	9	15	0	2	9	11	3	14	14	57
94 °C	2	11	13	0	0	2	2	0	2	16	69
Back to 25 °C	6	12	18	0	3	12	15	0	15	13	54

The values in the table are percentages.

sufficient to convert these proteins to the final rodlet structure [4,8,9]. All three hydrophobins from *A. fumigatus* are also capable of assembly into amyloid structures *in vitro*, as judged by the time-dependent increase in fluorescence when samples were incubated with the amyloid binding dye thioflavin T (ThT) and shaken vigorously to increase the air-water interface (Supplemental Fig. S4). These three hydrophobins display kinetics typical of amyloid formation, with a sigmoidal shape consisting of three phases: an initial lag phase corresponding to nucleation followed by a fast phase of amyloid formation and elongation and a final stationary phase (Supplemental Fig. S4). For RodA and RodB, which form amyloids rapidly under these conditions, the nucleation phase is almost not observed, similar to EAS $_{\Delta 15}$ and MPG1 [4]. Furthermore, as previously shown for MPG1, DewA and EAS $_{\Delta 15}$ [4,21], a HHI is also required by *A. fumigatus* hydrophobins to self-assemble into amyloids. If the HHI is abolished as described in Ref. [21], even under vigorous agitation and long incubation times, RodA, RodB and RodC do not bind ThT and therefore do not form amyloids (Supplemental Fig. S4).

Unfortunately, it proved impossible to collect SRCD spectra from previously prepared samples of lyophilized hydrophobin rodlets, even after extensive sonication efforts to dissolve or disperse the resuspended material. The hydrophobic nature of these proteins and the tendency of the rodlets to associate laterally into films appear to result in the formation of large insoluble protein clusters that are opaque to the beam. This contrasts with the samples of lyophilized amyloid fibrils composed of α -synuclein, which readily redissolved in buffer upon sonication and gave rise to strong SRCD signals (Supplemental Fig. S3).

Even if rodlet formation did occur to some extent in some of these heated samples, self-assembly into the rodlet form does not necessarily involve an overall large increase in β -sheet structure if intermolecular β -sheet interactions replace intramolecular ones, or the β -barrel core structure relaxes or unfolds to some extent when self-assembly occurs, as data suggest is the case for EAS $_{\Delta 15}$ [18,32]. This is supported by the observation of a shift from predominantly right-hand twisted β -structure in the monomeric forms of the hydrophobins to more relaxed β -structure in the assembled forms (Table 2).

ATR FT-IR also shows changes in hydrophobin conformation upon heating of hydrophobins in solution in the presence of a silicon crystal and air/solution interface

The structural transitions induced by heating the six class I hydrophobins in the presence of a silicon crystal were also investigated by FT-IR. The element silicon is hydrophobic, but the silicon crystal is readily oxidized in the presence of air or water at room temperature and becomes hydrophilic. Although the sample chamber

was sealed, some evaporation of the sample did occur during the heating, demonstrated by recovery of only 65% of the sample volume and indicating the generation of an air/solution interface during the thermal transition. For all six hydrophobins, there was a very large increase (from ~10- to 50-fold) in the raw signal (i.e., absorbance) across the spectra as the temperature increased, consistent with protein adsorbing to the silicon surface when the sample was heated (Supplemental Fig. S5). A similar increase has been observed for SC3 during self-assembly at an air-water interface [33]. Given this, vector normalization was performed following vapor subtraction, to compensate for the increasing coverage of the detector as the temperature rose. In five of the hydrophobins (all except RodC), heating resulted in a shift of the position of the main peak to ≤ 1630 cm^{-1} and a decrease in signal intensity in the shoulder at ~ 1660 – 1680 cm^{-1} (Fig. 4). The presence of a main peak at ≤ 1630 cm^{-1} is consistent with amyloid β -sheet structural content and is suggestive of rodlet assembly, as cross- β structures in amyloid give rise to FT-IR signals between 1611 – 1630 cm^{-1} , whereas native β -sheet structures give rise to broader maxima between 1630 – 1643 cm^{-1} . The reduced twist angle in cross- β amyloid structures, compared to native β -structures, is correlated with maxima at lower wavenumbers [34]. The samples were recovered after the FT-IR experiments and examined by transmission electron microscopy (Fig. 5). For MPG1 and EAS $_{\Delta 15}$, straight rodlets, appearing in clusters, were observed. DewA and RodA formed large sheets composed of wavy fibrils. RodB assemblies consisted of laterally packed bundles with some regular substructure. No polymeric structures could be detected in samples of RodC. The observation of RodA rodlets after heating in the FT-IR cell indicates that the combination of heating, generation of an air/solution interface and the more hydrophobic silicon surface is sufficient to trigger rodlet formation, whereas heating and generation of microbubbles in the quartz cell used for SRCD was not. No clear structural transition was detected in RodC by FT-IR under these conditions, and no polymeric structures could be detected afterward by electron microscopy, in spite of the demonstrated ability of RodC to self-assemble into ThT-positive structures from solution, with vigorous shaking and exposure to air/solution interfaces (Supplemental Fig. S4). Further work will be required to identify the nature of biologically relevant interface(s) able to trigger RodC rodlet assembly. These results highlight the surface activity of hydrophobins and the importance of particular interfaces for the activity of individual hydrophobins.

FT-IR spectra were also collected from lyophilized samples of monomeric forms of the six hydrophobins and from lyophilized preparations of rodlets. In all cases, a shift was observed in the position of the main peak from ~ 1640 to ≤ 1630 cm^{-1} (Fig. 6). The differences between spectra collected from lyophilized

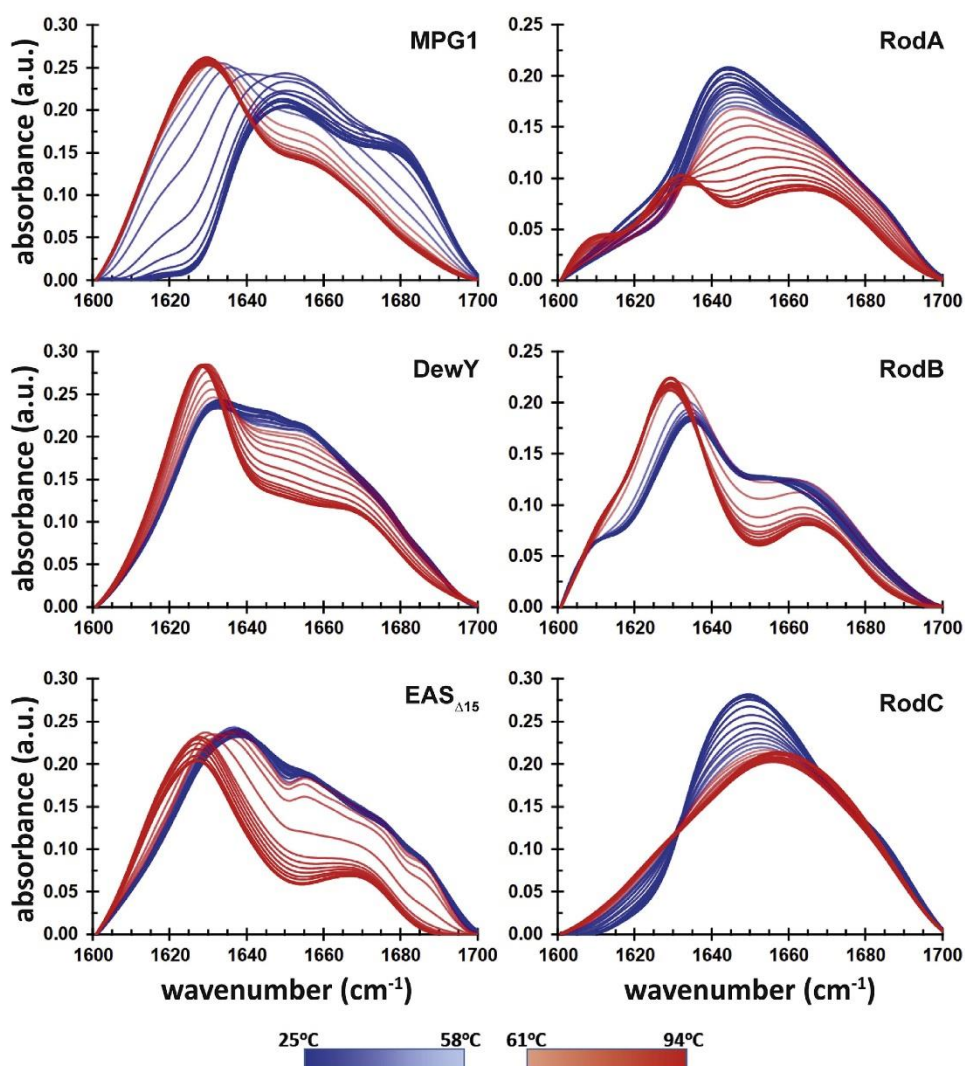


Fig. 4. Temperature-dependent conformational change of the six hydrophobins in solution, as measured by ATR FT-IR using a silicon crystal. Spectra were recorded from 25 °C to 94 °C in 3-degree steps. The changes in the amide I region of the FT-IR protein spectra with increasing temperature are color-coded in blue and red as indicated in the bottom of the figure. Spectra are baseline corrected. The FT-IR thermal transition experiments were performed once (RodA, RodB and RodC), twice ($EAS_{\Delta 15}$), three times (DewY) or four times (MPG1), with reproducible results.

monomer and rodlet samples were less marked than those observed in the heated samples. The interaction between the hydrophobin proteins and the silicon surface, from solution, appears to result in additional ordering of the secondary structure. While

the lyophilized hydrophobins are not in their native environment and may undergo some structural change when lyophilized, it is clear that the lyophilized rodlet samples gave rise to spectra with main peaks appearing at consistently lower wavenumbers than

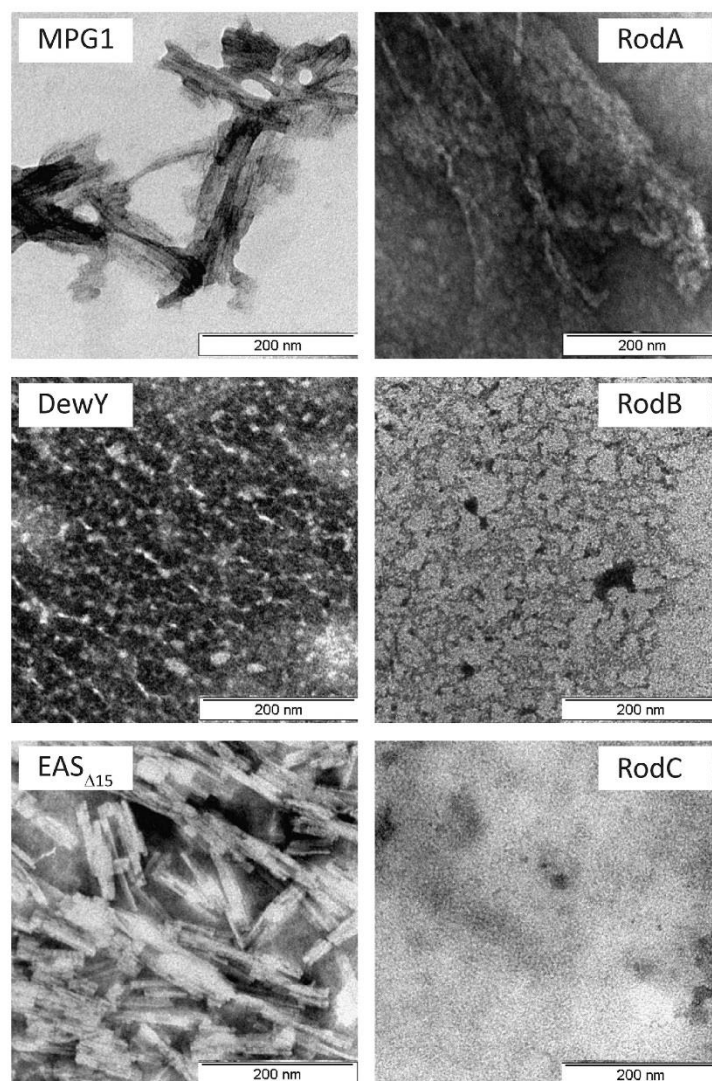


Fig. 5. Negatively stained electron micrographs of hydrophobin samples recovered from FT-IR thermal transition experiments. Samples were stained with uranyl acetate (MPG1, RodA, RodB and RodC) or sodium silicotungstate (DewY, EAS $_{\Delta 15}$) to achieve contrast. Scale bars are 200 nm.

spectra recorded from the monomeric form of the same protein lyophilized from the soluble state (Fig. 6). The extent of the shift to lower wavenumbers is similar to that observed for lyophilized samples of α -synuclein upon assembly from monomers to fibrils (Supplemental Fig. S3).

In these FT-IR analyses, the hydrophobin rodlets do not display as pronounced a shift to lower wavenumbers as other amyloid structures and this could reflect the steric restraints imposed by the multiple disulfide bonds in hydrophobins. The C3–C4 and C7–C8 disulfide bridges each link two contiguous β -strands

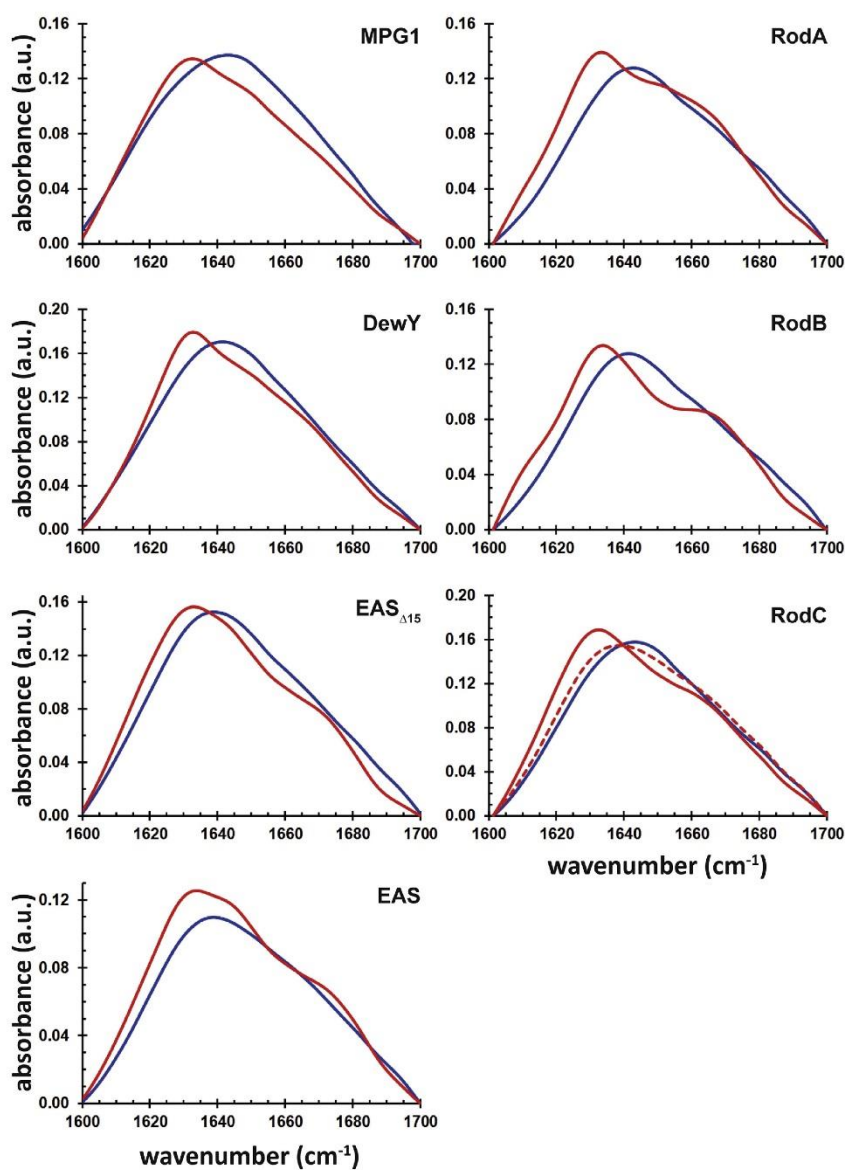


Fig. 6. ATR FT-IR spectra collected from lyophilized samples of hydrophobins in monomeric (blue) and rodlet (red) forms. At least three spectra were recorded for each protein sample. The amide I regions from representative baseline-corrected spectra are shown. Two populations of RodC rodlets with distinct structures were observed in two different samples, as indicated by the red solid and dashed lines.

or extended backbone segments in the hydrophobins of known structure. These disulfides show an unusual, tight arrangement in RodA, MPG1, DewY and EAS_{Δ15},

which differs from the most commonly observed linear arrangement of disulfides (Supplemental Fig. S6). This arrangement is reflected in the chemical shifts

observed for the CB carbons of the C3, C4, C7 and C8 cysteines of the six hydrophobins, which show highly downfield-shifted resonances with very high chemical shift values ranging between 45.3 and 53.8 ppm (Supplemental Fig. S6), except for cysteine C7 of both DewA conformers and C4 of the less populated DewA conformer 2, which display lower chemical shifts. These chemical shifts are in the higher percentiles for Cys CB chemical shifts in the BMRB database. A marked change is observed in the 225- to 230-nm region of the SRCD spectrum of EAS $_{\Delta 15}$ with heating (Fig. 3). Although less pronounced, this effect is also observed for RodC and MPG1, or in the stable conformation adopted by RodA upon cooling back to 25 °C. Constrained disulfide bonds and aromatic residues in asymmetric environments can contribute to the CD signal around 225–230 nm, although the sign of the contribution cannot be predicted [35]. Hydrophobins contain only a few tyrosine and phenylalanine aromatic residues, and in the known structures, several of them are at least partially solvent exposed, suggesting that their contribution to the signal should be minor. The changes in this region of the SRCD spectra may therefore possibly indicate that heating of these hydrophobin is accompanied by a conformational change within the β -barrel that results in a change in the conformation and relaxation of the β -barrel disulfides (Fig. 3).

Conclusions

SRCD was chosen as a method of analysis of hydrophobin structure and conformational plasticity because of the increased informational content arising from the accessible lower wavelengths and the possibility of discriminating between parallel and anti-parallel β -sheets and left-hand twisted, right-hand-twisted and relaxed β -structures. Estimation of the secondary structure content of the monomeric forms of MPG1, DewA, EAS $_{\Delta 15}$, RodA, RodB and RodC in solution reveals that the hydrophobins from *A. fumigatus* conform to the characteristic, tightly constrained β -barrel or half-barrel core structure previously described for MPG1, DewA and EAS $_{\Delta 15}$ [4,8,9,36] and in others [37-39]. A diverse range of regular secondary structure elements and irregular loops, bends, β -bridges and helical components occur in the inter-cysteine regions and are accommodated on the periphery of the barrel structures.

Hydrophobins are highly surface-active proteins and assemble on hydrophilic and hydrophobic surfaces in a way that reverses the wettability of the surface [28,40]. On hydrophobic surfaces, some class I hydrophobins have been shown to form amyloid-structured rodlet layers that are resistant to depolymerization when exposed to acids, bases and detergents [21,31,41,42], but most class I hydrophobins studied to date, including the six studied here, critically require a HHI to undergo

the transition to the amyloid rodlet form [4,21]. Although other conditions can induce self-assembly of some hydrophobins in solution, for example, SC3 [19], none of the hydrophobins from *N. crassa*, *M. oryzae*, *A. nidulans* and *A. fumigatus* that we have studied here self-assemble to form rodlets in bulk solution. There is no evidence for self-assembly in the absence of a HHI at the relatively high concentrations (360–690 μ M; 5–10 mg/mL) required for NMR structural studies, which have yielded the structures or the assignments of these proteins in solution.

Heating in a quartz cell under conditions that resulted in the generation of microbubbles and HHIs triggered conformational change of MPG1, DewY, EAS $_{\Delta 15}$ and RodB into an irreversible form that is likely on-pathway to rodlets. The quartz surface itself remains hydrophilic under these conditions, indicating that it is the generation of the HHI that induced conformational change in the proteins [43]. The thermal transition was accompanied by loss of helical structure in MPG1, RodB and DewY, indicating an alteration from the monomeric form of these proteins that has been characterized in solution. Heating resulted in a relatively small increase in β -structure content in all of the hydrophobins. This finding may reflect that the thermally induced form that is detected under these conditions is not the final cross- β rodlet structure or it may provide an indication that rodlet assembly involves some interchange between intramolecular and intermolecular β -sheet content and not just the formation of new β -sheet interactions. SC3, a class I hydrophobin from *S. commune*, initially assembles into a β -structure-rich but morphologically featureless, stable protein film that subsequently develops the characteristic fibrillar rodlet morphology upon extended incubation [33]. SRCD analysis revealed that the thermal transition was accompanied by a relative increase in relaxed β -structure over the right-hand twisted sheets found in the monomeric forms of the hydrophobins in solution. These changes are consistent with the conformational changes predicted by the model of the rodlet form of EAS $_{\Delta 15}$ that is consistent with ssNMR data [18].

It was possible to collect FT-IR spectra from lyophilized monomeric and rodlet forms of the hydrophobins. These data indicated that self-assembly of these hydrophobins involves a change from a mixture of helical, β -sheet and less regular structure to the β -rich form found in disease-associated fibrils and in other functional amyloids [33,34]. Along with ThT amyloid assembly assays, these experiments confirmed that the previously uncharacterized hydrophobins RodA, RodB and RodC from *A. fumigatus* do self-assemble into amyloid-structures similar to those formed by other class I hydrophobins, and they require a HHI for assembly into ThT-positive structures. Heating of the hydrophobins in the presence of a silicon crystal and an air/solution interface in the FT-IR experiments exposed the proteins to an environment that triggered conformational change and self-assembly into the rodlet

form for all of the hydrophobins except RodC. The different effects observed with quartz and silicon surfaces highlight the surface activity of these proteins and the effect of diverse interfaces on the properties of these unusual proteins. These differences may reflect the multiple roles played by these proteins, including on the fungal spore surface (EAS $_{\Delta 15}$, MPG1 and RodA), within the spore (DewY) and during infection and biofilm formation (RodB). Future identification of the role of RodC in *A. fumigatus* in the spore cell wall may reveal the nature of the native interface required to induce its self-assembly into the rodlet form [11].

The hydrophobin rodlet structure was first observed on the surface of fungal spores in electron micrographs more than 50 years ago [17,44]. Its role in protection of the spore and identification of component hydrophobins occurred decades later, and rodlets were first identified as functional amyloids in 2000 [45]. Much of our understanding about the cross- β structure of amyloid fibrils and the mechanism of amyloid formation comes from studies of disease-causing amyloidogenic proteins and polypeptides [46], where formation results from self-assembly of aberrantly produced or misfolded forms of proteins and the protein function is generally lost upon fibril formation. However, there is a growing recognition that the amyloid fibril structure is widely applied in nature for diverse functional purposes [47]. In hydrophobin rodlets and other functional amyloids, biological activity is maintained or generated when the fibril forms. Hydrophobin rodlets are a particularly intriguing form of functional amyloid because the fibrils further associate laterally to form amphipathic sheets. This study has highlighted the dynamic nature of hydrophobins and the role of HHIs in triggering conformational change and self-assembly. Future high-resolution studies of the assembled functional rodlets will shed light on the roles they play in fungal biology and may lead to application of hydrophobins in biotechnological applications.

Materials and Methods

Protein expression and purification

All hydrophobins were produced as fusion proteins with an N-terminal hexahistidine (His $_6$) tagged ubiquitin (Ub) and a cleavage site between the Ub sequence and the hydrophobin (Hyd) sequence. A similar protocol was used for the six proteins. The His $_6$ -Ub-Hyd proteins were expressed using the *Escherichia coli* BL21 (DE3) strain. Bacteria were grown at 37 °C, expression was induced with IPTG and cells were harvested by centrifugation after 3 or 4 h of induction. The fusion proteins were (i) extracted from cells with denaturant (6 M guanidinium hydrochloride), (ii) affinity purified under denaturing conditions and buffer-exchanged to 8 M urea-containing solutions on nickel columns,

(iii) folded *in vitro* by dialysis against an appropriate folding buffer containing reduced and oxidized glutathione and (iv) proteolyzed with the His $_6$ -tagged deubiquinating UBP41 or TEV enzymes. Hydrophobins were then (v) separated from the enzymes and the remaining unproteolyzed fusion proteins on a second nickel affinity column, (vi) further purified by reverse-phase chromatography on hydrophobic C $_{18}$ or C $_4$ columns and (vii) lyophilized until further use. For RodA, RodB and RodC, (viii) a final size exclusion chromatography separation was performed using a Superdex 75 Increase column (GE Healthcare) to obtain the monomeric proteins. *A. fumigatus* proteins were buffer exchanged against 20 mM sodium bicarbonate or H $_2$ O and lyophilized until further use. The vectors and the detailed protocols for DewY, EAS $_{\Delta 15}$, MPG1 and RodA have been described [4,8,9,16]. For RodB and RodC, the same protocol used for RodA was applied [16]. Plasmids based on the pET28b vector (Novagen) coding for RodB and RodC fusion proteins His $_6$ -Ub-Hyd (and ampicillin resistance) were purchased from Proteogenix (France). The sequences of RodB and RodC corresponded to full-length sequence without the predicted N-terminal secretion peptide and additional N-terminal serine residue arising from cloning. For NMR experiments with doubly labeled ^{15}N - ^{13}C RodB or RodC, bacteria were grown in minimal M9 media supplemented with 0.43 g/L of yeast extract without amino acids and without ammonium sulfate (DIFCO), and containing $^{15}\text{NH}_4\text{Cl}$ (0.52 g/L, $\geq 98\%$; Eurisotop) and $^{13}\text{C}_6$ glucose (2 g/L, $\geq 98\%$; Eurisotop) as sole sources of nitrogen and carbon, respectively. α -Synuclein was recombinantly expressed and purified as previously described [48]. Purified lyophilized α -synuclein was dissolved in 6 M guanidine hydrochloride and 20 mM Tris.HCl (pH 7.4) to a concentration of $\sim 300 \mu\text{M}$. To obtain monomeric protein in solution, sample was buffer exchanged into 20 mM NaH $_2$ PO $_4$ and 150 mM NaCl (pH 7.4) using a ZebraTM spin desalting column with 7 kDa MWCO (ThermoScientific). Fibrils were formed by continuously shaking the solution of monomeric protein at 1200 rpm and 37 °C for 9 days in an Eppendorf Thermomixer Comfort. The fibril-containing solution was centrifuged at 16,000g for 20 min, and the pellet was washed and resuspended in MilliQ water and then lyophilized. For SRCD measurements, lyophilized fibrils were re-dissolved into 20 mM NaH $_2$ PO $_4$ (pH 7.4) and sonicated with a probe sonicator for 30 s twice at the highest-power setting that did not generate foaming. Protein concentration was determined using an extinction coefficient of 5120 M $^{-1}$ cm $^{-1}$ at $A_{280 \text{ nm}}$.

For all hydrophobins, sample purity was assessed to be $\geq 98\%$ by analytical RP-HPLC and SDS-PAGE (Supplemental Fig. S7). MALDI-TOF mass spectrometry indicated the integrity of the proteins and NMR spectra and parameters were in agreement with having monomeric forms of the proteins up to concentrations of 5–10 mg/mL depending on the protein.

Assignment of NMR backbone chemical shifts of RodB and RodC

NMR experiments were recorded on 600-MHz [Direct Drive (Agilent Technologies) or Avance III HD (Bruker)] or 800-MHz (Avance Neo, Bruker) proton resonance frequency spectrometers equipped with cryogenically cooled probes. Experiments were run at 25 °C for RodB and 45 °C for RodC. Protein concentration and buffer were 0.47 mM in 50 mM sodium phosphate (pH 6.5) and 5% D₂O for RodB and 0.6 mM in 50 mM deuterated sodium acetate (pH 4.5) and 10% D₂O for RodC. Spectra were recorded using VnmrJ 3.2 (Agilent Technologies) or TopSpin 3.5.7 or 4.0 (Bruker), processed with NMRPipe and analysed with CCPNMR analysis 2.4.2 [49]. Backbone and CB atoms of RodB and RodC resonances were assigned from ¹⁵N-¹H HSQC [50], HNC0, HN(CO)CA, HNCACB, CBCA(CO)NH [51] and HNHA [52] experiments following standard procedures.

SRCD spectropolarimetry

SRCD experiments were performed at the SOLEIL Synchrotron (Saclay, France) on the DISCO beam line (proposal 20160949). The beamline was calibrated with CSA at 6.9 mg/mL in a 0.01-cm pathlength cell as standard. Lyophilized preparations of monomeric or amyloid rodlet forms of the proteins were dissolved in an appropriate buffer and studied in quartz (0.005-cm optical path) or calcium fluoride cells (0.0012-cm optical path) at concentrations ranging from 3.4 to 8.1 mg/mL. For MPG1, the sample was dissolved in 25 mM sodium phosphate (pH 7.4), and for the other five hydrophobins, samples were dissolved in 20 mM sodium acetate (pH 5.0). Three or five scans at 25 °C with a 1-nm step were accumulated for each sample. Temperature ramps were performed between 25 °C and 94 °C in 3 °C steps, with heating at 0.6 °C/min and with one or two scans recorded per 3 °C step. For each protein except for EAS_{Δ15}, a final spectrum was collected after the sample had cooled back to 25 °C. Sample concentrations were determined by absorbance. Protein spectra were obtained from the difference of protein-in-buffer and the buffer spectra and converted to residual molar circular dichroism ($\Delta\epsilon$, M⁻¹ · cm⁻¹) using *CDtool* [27].

Secondary structure calculations

The secondary structure content of DewY, EAS_{Δ15}, MPG1 and RodA (Valsecchi *et al.*, in preparation) was estimated from the corresponding PDB structures using DSSP [30] and with BeStSel [24]. The secondary structure content of the soluble monomeric form of the six hydrophobins used in this study was also calculated from NMR experimental chemical shifts (H, N, CO, CA, CB and HA) with the TALOS-N algorithm [53] data

deposited with the BMRB or determined herein (RodB and RodC). SRCD spectra were deconvoluted with BeStSel [24] to estimate the secondary structure content of the corresponding proteins.

Amyloid formation followed by ThT fluorescence

The fluorescence enhancement of ThT upon binding amyloid fibers was used to monitor amyloid formation by RodA, RodB and RodC. Experiments were performed using black 96-well flat-bottom plates (Greiner) with proteins at a final 50-μg/mL concentration in H₂O (RodA and RodB) or 20 mM sodium acetate (pH 5.0; RodC) and 40 μM ThT. Kinetic experiments were conducted on a SAFAS Monaco Xenius XC fluorimeter, with excitation at 415 nm, emission at 484 nm and 10-nm excitation and emission. Samples were incubated in the fluorimeter at 40 °C (RodA and RodB) or 50 °C (RodC) under vigorous orbital mixing (RodA and RodB: 720 rpm; RodC: 840 rpm) between readings. To assess the importance of an interface in amyloid formation, we used the method proposed in Ref. [21]. Samples were deposited in completely filled wells (400 μL, no HHI) or partially filled wells (100 μL), and the wells were carefully sealed. Samples were then incubated for 16 h at 25 °C (RodA and RodB) or 50 °C (RodC) under orbital mixing at 840 rpm. Fluorescence spectra were recorded before and after incubation.

Attenuated total reflection FT-IR of lyophilized monomer and rodlet hydrophobin samples

Lyophilized rodlet samples were prepared by dissolving purified, lyophilized monomeric hydrophobins in MilliQ water to a concentration of 0.5–1.0 mg/mL. Over a 5-day period, samples were repeatedly shaken for 5–6 h, centrifuged for 10 min at 16,000g, lyophilized overnight, and then resuspended in water. For RodC, the sample was incubated at 50 °C for 6 h with shaking at 1200 rpm. Attenuated total reflection (ATR) FT-IR measurements were performed on lyophilized samples of monomeric or rodlet forms using a Bruker Lumos FT-IR microscope. Spectra were recorded from 4000 to 600 cm⁻¹ with a resolution of 4 cm⁻¹. Three to five spectra consisting of an average of 64 scans each were collected for each sample.

ATR FT-IR of hydrophobins in solution and during heating

Lyophilized monomeric proteins were dissolved in the appropriate buffer as used for SRCD at concentrations ranging from 3.8 to 6.5 mg/mL. ATR FT-IR spectra of protein solutions were recorded using a Bruker CONFOCHECK spectrometer equipped with a BioATR II cell. For FT-IR measurements, 20-μL samples were placed on the surface of the silicon

crystal in the sample chamber, which has a radius of 2 mm and which was sealed before measurements and heating commenced. Spectra were collected from 25 °C to 94 °C in 3 °C steps. The sample was allowed to equilibrate for 180 s at each temperature before spectra collection. Spectra were recorded from 4000 to 850 cm^{-1} with a resolution of 4 cm^{-1} . Each spectrum is an average of 128 scans. Protein concentrations were determined by absorbance measurements for DewY and EAS $_{\Delta 15}$ and by the BCA protein assay for the other four hydrophobins.

Transmission electron microscopy

Post-FT-IR thermal transition experiment samples were diluted 100-fold in MQW. For MPG1, RodA, RodB and RodC, a 20- μL drop of the hydrophobin-containing solution was placed directly onto the surface of a carbon-formvar-coated TEM grid (ProSciTech) and allowed to incubate for 10 min. Then the excess solution was wicked away and the grids were washed with MilliQ water three times. Samples were stained with 2% uranyl acetate for 10 min. For DewY and EAS $_{\Delta 15}$ samples, a 20- μL drop of hydrophobin solution was incubated for 20 min before floating a TEM grid on the surface of the drop for 30 s. The TEM grids were washed three times and then stained with sodium silicotungstate for 10 min. Grids were imaged at 120 kV on a Philips 120 Biofilter TEM with EMSIS Veleta CCD camera.

Acknowledgments

This work was supported by the Australian Research Council in the form of Discovery Project Grants to M.S. and A.H.K. (DP120100756 and DP150104227) and by Australian Government funding in the form of Post-graduate Research Awards to V.L. and S.B. The data collection at SOLEIL Synchrotron was funded by proposal 20160949, and we are grateful to Matthieu Réfrégiers for assistance with the application for beam time. We thank and acknowledge the support of the staff, particularly Joonsup Lee, in the Vibrational Spectroscopy facility at the Sydney Analytical Core Research Facility. This work was additionally funded by the French ANR (ANR FUNHYDRO ANR-16S-CE110020-01) and the Institut Pasteur PTR 529 awarded to J.I.G. B.R.F. is part of the Pasteur-Paris University International PhD Program. This program has received funding from the European Union's Horizon 2020 research and innovation program under the Marie Skłodowska-Curie grant agreement No. 665807. The 800-MHz NMR spectrometer of the Institut Pasteur was partially funded by the Région Ile de France (SESAME 2014 NMRCHR grant no 4014526).

Appendix A. Supplementary data

Supplementary data to this article can be found online at <https://doi.org/10.1016/j.jmb.2018.07.025>.

Received 5 May 2018;

Received in revised form 19 July 2018;

Accepted 23 July 2018

Available online 7 August 2018

Keywords:

functional amyloid;
hydrophobin;
rodlet;
synchrotron radiation circular dichroism;
Fourier-transform infrared

†C.L.L.P. and B.R.F. contributed equally to this work.

Present address: R. Dazzoni, Institute of Chemistry and Biology of Membranes and Nano-Objects, 33607 Pessac, France.

Abbreviations used:

HHIs, hydrophobic/hydrophilic interfaces; SRCD, synchrotron radiation circular dichroism; FT-IR, Fourier-transform infrared spectroscopy; ThT, thioflavin T; ATR, attenuated total reflection.

References

- [1] J. Bayry, V. Aimananda, J.I. Guijarro, M. Sunde, J.P. Latge, Hydrophobins—unique fungal proteins, *PLoS Pathog.* 8 (2012), e1002700.
- [2] B.G. Jensen, M.R. Andersen, M.H. Pedersen, J.C. Frisvad, I. Sondergaard, Hydrophobins from *Aspergillus* species cannot be clearly divided into two classes, *BMC Res. Notes* 3 (2010) 344.
- [3] V. Seidl-Seiboth, S. Gruber, U. Sezerman, T. Schwecke, A. Albayrak, T. Neuhof, et al., Novel hydrophobins from *Trichoderma* define a new hydrophobin subclass: protein properties, evolution, regulation and processing, *J. Mol. Evol.* 72 (2011) 339–351.
- [4] C.L.L. Pham, A. Rey, V. Lo, M. Soullès, Q. Ren, G. Meisl, et al., Self-assembly of MPG1, a hydrophobin protein from the rice blast fungus that forms functional amyloid coatings, occurs by a surface-driven mechanism, *Sci. Rep.* 6 (2016) 25288.
- [5] N.J. Talbot, M.J. Kershaw, G.E. Wakley, O.M.H. deVries, J.G.H. Wessels, J.E. Hamer, MPG1 encodes a fungal hydrophobin involved in surface interactions during infection-related development of *Magnaporthe grisea*, *Plant Cell* 8 (1996) 985–999.
- [6] V. Aimananda, J. Bayry, S. Bozza, O. Kniemeyer, K. Perruccio, S.R. Elluru, et al., Surface hydrophobin prevents immune recognition of airborne fungal spores, *Nature* 460 (2009) 1117–1121.
- [7] J. Fernandez, K. Orth, Rise of a cereal killer: the biology of *Magnaporthe oryzae* biotrophic growth, *Trends Microbiol.* 26 (2018) 582–597.
- [8] V.K. Morris, A.H. Kwan, M. Sunde, Analysis of the structure and conformational states of DewA gives insight into the

- assembly of the fungal hydrophobins, *J. Mol. Biol.* 425 (2013) 244–256.
- [9] A.H. Kwan, I. Macindoe, P.V. Vukasin, V.K. Morris, I. Kass, R. Gupta, et al., The Cys3–Cys4 loop of the hydrophobin EAS is not required for rodlet formation and surface activity, *J. Mol. Biol.* 382 (2008) 708–720.
- [10] S. Paris, J.P. Debeauvais, R. Cramer, M. Carey, F. Charles, M.C. Prevost, et al., Conical hydrophobins of *Aspergillus fumigatus*, *Appl. Environ. Microbiol.* 69 (2003) 1581–1588.
- [11] I. Valsecchi, V. Dupres, E. Stephen-Victor, J.I. Guijarro, J. Gibbons, R. Beau, et al., Role of hydrophobins in *Aspergillus fumigatus*, *J. Fungi* 4 (2018) 2.
- [12] M.B. Linder, G.R. Szilvay, T. Nakari-Setälä, M.E. Penttilä, Hydrophobins: the protein-amphiphiles of filamentous fungi, *FEMS Microbiol. Rev.* 29 (2005) 877–896.
- [13] M. Khalesi, K. Gebruers, G. Derdelinckx, Recent advances in fungal hydrophobin towards using in industry, *Protein J.* 34 (2015) 243–255.
- [14] S. Boeuf, T. Thom, B. Gutt, T. Strunk, M. Hoffmann, E. Seebach, et al., Engineering hydrophobin DewA to generate surfaces that enhance adhesion of human but not bacterial cells, *Acta Biomater.* 8 (2012) 1037–1047.
- [15] U. Weickert, F. Wiesend, T. Subkowski, A. Eickhoff, G. Reiss, Optimizing biliary stent patency by coating with hydrophobin alone or hydrophobin and antibiotics or heparin: an in vitro proof of principle study, *Adv. Med. Sci.* 56 (2011) 138–144.
- [16] A. Pille, A.H. Kwan, I. Cheung, M. Hampsey, V. Airmananda, M. Delepiere, et al., (1)H, (13)C and (15)N resonance assignments of the RodA hydrophobin from the opportunistic pathogen *Aspergillus fumigatus*, *Biomol. NMR Assign.* 9 (2015) 113–118.
- [17] M. Sunde, A.H. Kwan, M.D. Templeton, R.E. Beever, J.P. Mackay, Structural analysis of hydrophobins, *Micron* 39 (2008) 773–784.
- [18] V.K. Morris, R. Linser, K.L. Wilde, A.P. Duff, M. Sunde, A.H. Kwan, Solid-state NMR spectroscopy of functional amyloid from a fungal hydrophobin: a well-ordered beta-sheet core amidst structural heterogeneity, *Angew. Chem. Int. Ed. Engl.* 51 (2012) 12621–12625.
- [19] A. Zykwincka, T. Guillemette, J.P. Bouchara, S. Cuenot, Spontaneous self-assembly of SC3 hydrophobins into nanorods in aqueous solution, *Biochim. Biophys. Acta* 1844 (2014) 1231–1237.
- [20] A.M. Gravagnuolo, S. Longobardi, A. Luchini, M.S. Appavou, L. De Stefano, E. Notomista, et al., Class I hydrophobin Vmh2 adopts atypical mechanisms to self-assemble into functional amyloid fibrils, *Biomacromolecules* 17 (2016) 954–964.
- [21] V.C. Lo, Q. Ren, C.L. Pham, V.K. Morris, A.H. Kwan, M. Sunde, Fungal hydrophobin proteins produce self-assembling protein films with diverse structure and chemical stability, *Nanomaterials (Basel)* 4 (2014) 827–843.
- [22] V.K. Morris, Q. Ren, I. Macindoe, A. Kwan, N. Byrne, M. Sunde, Recruitment of class I hydrophobins to the air:water interface initiates a multi-step process of functional amyloid formation, *J. Biol. Chem.* 286 (2011) 15955–15963.
- [23] P.S. Kumagai, A.P.U. Araujo, J.L.S. Lopes, Going deep into protein secondary structure with synchrotron radiation circular dichroism spectroscopy, *Biophys. Rev.* 9 (2017) 517–527.
- [24] A. Miconai, F. Wien, L. Kernya, Y.H. Lee, Y. Goto, M. Refregiers, et al., Accurate secondary structure prediction and fold recognition for circular dichroism spectroscopy, *Proc. Natl. Acad. Sci. U. S. A.* 112 (2015) E3095–E3103.
- [25] K. Matsuo, H. Hiramoto, K. Gekko, H. Namatame, M. Taniguchi, R.W. Woody, Characterization of intermolecular structure of beta(2)-microglobulin core fragments in amyloid fibrils by vacuum-ultraviolet circular dichroism spectroscopy and circular dichroism theory, *J. Phys. Chem. B* 118 (2014) 2785–2795.
- [26] P. Ruzza, R. Hussain, B. Biondi, A. Calderan, I. Tessari, L. Bubacco, et al., Effects of trehalose on thermodynamic properties of alpha-synuclein revealed through synchrotron radiation circular dichroism, *Biomol. Ther.* 5 (2015) 724–734.
- [27] J.G. Lees, B.R. Smith, F. Wien, A.J. Miles, B.A. Wallace, CDtool—an integrated software package for circular dichroism spectroscopic data processing, analysis, and archiving, *Anal. Biochem.* 332 (2004) 285–289.
- [28] Q. Ren, A.H. Kwan, M. Sunde, Two forms and two faces, multiple states and multiple uses: properties and applications of the self-assembling fungal hydrophobins, *Biopolymers* 100 (2013) 601–612.
- [29] J.D. Thompson, D.G. Higgins, T.J. Gibson, CLUSTAL W: improving the sensitivity of progressive multiple sequence alignment through sequence weighting, position-specific gap penalties and weight matrix choice, *Nucleic Acids Res.* 22 (1994) 4673–4680.
- [30] W. Kabsch, C. Sander, Dictionary of protein secondary structure: pattern recognition of hydrogen-bonded and geometrical features, *Biopolymers* 22 (1983) 2577–2637.
- [31] X. Wang, M.L. De Vocht, J. De Jonge, B. Poolman, G.T. Robillard, Structural changes and molecular interactions of hydrophobin SC3 in solution and on a hydrophobic surface, *Protein Sci.* 11 (2002) 1172–1181.
- [32] I. Macindoe, A.H. Kwan, Q. Ren, V.K. Morris, W. Yang, J.P. Mackay, et al., Self-assembly of functional, amphipathic amyloid monolayers by the fungal hydrophobin EAS, *Proc. Natl. Acad. Sci. U. S. A.* 109 (2012) E804–E811.
- [33] M.L. De Vocht, I. Reviakine, W.P. Ulrich, W. Bergsma-Schutter, H.A.B. Wosten, H. Vogel, et al., Self-assembly of the hydrophobin SC3 proceeds via two structural intermediates, *Protein Sci.* 11 (2002) 1199–1205.
- [34] G. Zandomenighi, M.R. Krebs, M.G. McCammon, M. Fandrich, FTIR reveals structural differences between native beta-sheet proteins and amyloid fibrils, *Protein Sci.* 13 (2004) 3314–3321.
- [35] S.M. Kelly, T.J. Jess, N.C. Price, How to study proteins by circular dichroism, *Biochim. Biophys. Acta* 2005 (1751) 119–139.
- [36] A.H. Kwan, R.D. Winefield, M. Sunde, J.M. Matthews, R.G. Haverkamp, M.D. Templeton, et al., Structural basis for rodlet assembly in fungal hydrophobins, *Proc. Natl. Acad. Sci. U. S. A.* 103 (2006) 3621–3626.
- [37] J.A. Gandier, D.N. Langelaan, A. Won, K. O'Donnell, J.L. Grondin, H.L. Spencer, et al., Characterization of a Basidiomycota hydrophobin reveals the structural basis for a high-similarity class I subdivision, *Sci. Rep.* 7 (2017) 45863.
- [38] J. Hakanpää, M. Linder, A. Popov, A. Schmidt, J. Rouvinen, Hydrophobin HFBI in detail: ultrahigh-resolution structure at 0.75 Å, *Acta Crystallogr. D Biol. Crystallogr.* 62 (2006) 356–367.
- [39] J. Hakanpää, G.R. Szilvay, H. Kaljunen, M. Maksimainen, M. Linder, J. Rouvinen, et al., Two crystal structures of *Trichoderma reesei* hydrophobin HFBI—the structure of a protein amphiphile with and without detergent interaction, *Protein Sci.* 15 (2006) 2129–2140.

- [40] M. Sunde, C.L.L. Pham, A.H. Kwan, Molecular characteristics and biological functions of surface-active and surfactant proteins, *Annu. Rev. Biochem.* 86 (2017) 585–608.
- [41] M.L. de Vocht, K. Scholtmeijer, E.W. van der Vegte, O.M. de Vries, N. Sonveaux, H.A. Wosten, et al., Structural characterization of the hydrophobin SC3, as a monomer and after self-assembly at hydrophobic/hydrophilic interfaces, *Biophys. J.* 74 (1998) 2059–2068.
- [42] W. Yang, Q. Ren, Y.N. Wu, V.K. Morris, A.A. Rey, F. Braet, et al., Surface functionalization of carbon nanomaterials by self-assembling hydrophobin proteins, *Biopolymers* 99 (2013) 84–94.
- [43] R.N. Lamb, D.N. Furlong, Controlled wettability of quartz surfaces, *J. Chem. Soc. Faraday Trans. 1* 78 (1982) 61–73.
- [44] W.M. Hess, M.M. Sassen, C.C. Remsen, Surface characteristics of *Penicillium conidia*, *Mycologia* 60 (1968) 290–303.
- [45] H.A.B. Wosten, M.L. de Vocht, Hydrophobins, the fungal coat unraveled, *Biochim. Biophys. Acta Rev. Biomembr.* 1469 (2000) 79–86.
- [46] M. Sunde, C. Blake, The structure of amyloid fibrils by electron microscopy and X-ray diffraction, *Adv. Protein Chem.* 50 (1997) 123–159.
- [47] C.L. Pham, A.H. Kwan, M. Sunde, Functional amyloid: widespread in nature, diverse in purpose, *Essays Biochem.* 56 (2014) 207–219.
- [48] R. Cappai, S.L. Leck, D.J. Tew, N.A. Williamson, D.P. Smith, D. Galatis, et al., Dopamine promotes alpha-synuclein aggregation into SDS-resistant soluble oligomers via a distinct folding pathway, *FASEB J.* 19 (2005) 1377–1379.
- [49] W.F. Vranken, W. Boucher, T.J. Stevens, R.H. Fogh, A. Pajon, M. Llinas, et al., The CCPN data model for NMR spectroscopy: development of a software pipeline, *Proteins* 59 (2005) 687–696.
- [50] L.E. Kay, P. Keifer, T. Saarinen, Pure absorption gradient enhanced heteronuclear single quantum correlation spectroscopy with improved sensitivity, *J. Am. Chem. Soc.* 114 (1992) 10663–10665.
- [51] N.A. Farrow, O. Zhang, J.D. Forman-Kay, L.E. Kay, A heteronuclear correlation experiment for simultaneous determination of ^{15}N longitudinal decay and chemical exchange rates of systems in slow equilibrium, *J. Biomol. NMR* 4 (1994) 727–734.
- [52] G.W. Vuister, A. Bax, Quantitative J correlation: a new approach for measuring homonuclear three-bond $J\ \text{H}^{\text{N}}\text{H}^{\alpha}$ coupling constants in ^{15}N enriched proteins, *J. Am. Chem. Soc.* 115 (1993) 7772–7777.
- [53] Y. Shen, A. Bax, Protein backbone and sidechain torsion angles predicted from NMR chemical shifts using artificial neural networks, *J. Biomol. NMR* 56 (2013) 227–241.

Supplemental Data

Probing structural changes during self-assembly of surface-active hydrophobin proteins that form functional amyloids in fungi

Chi L. L. Pham et al.

Figure S1.

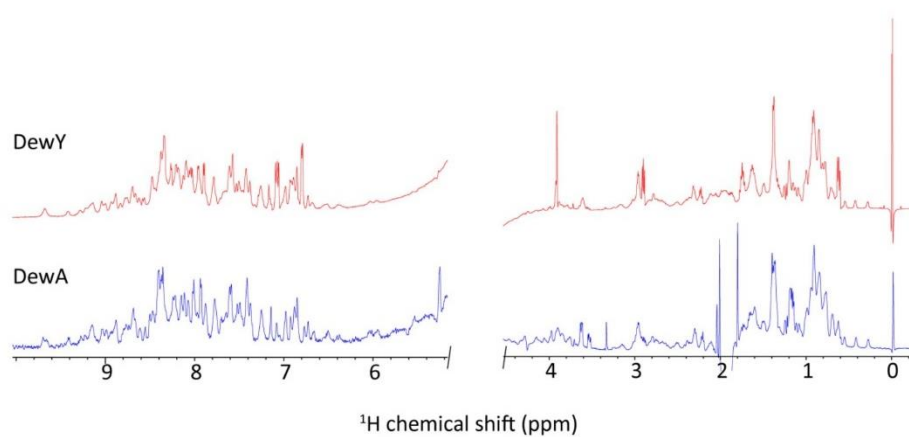


Fig. S1. 1D ¹H NMR spectra of DewY and DewA showing sharp and well-dispersed peaks indicative of folded proteins.

Figure S2.

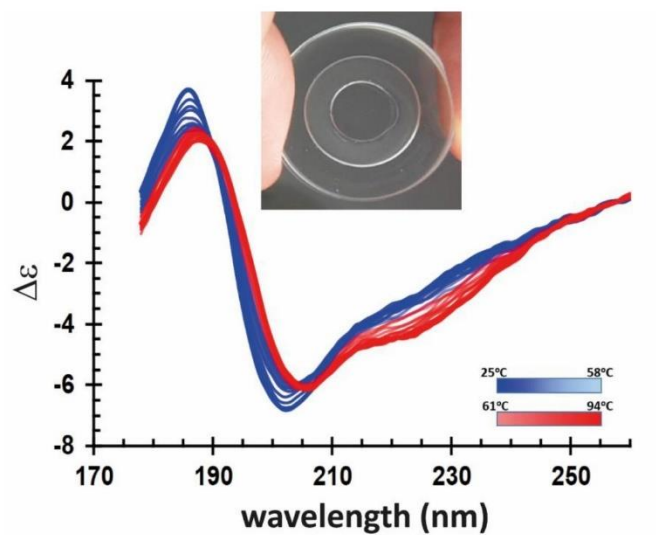


Fig. S2. Effect of increasing temperature on the secondary structure of RodA, as judged by SRCD spectra. Spectra were recorded from 25 °C to 94 °C in 3-degree steps, and spectra were collected with calcium fluoride cell. Photo insert shows no microbubbles formed in the calcium fluoride cell during the thermal transition experiments.

Figure S3.

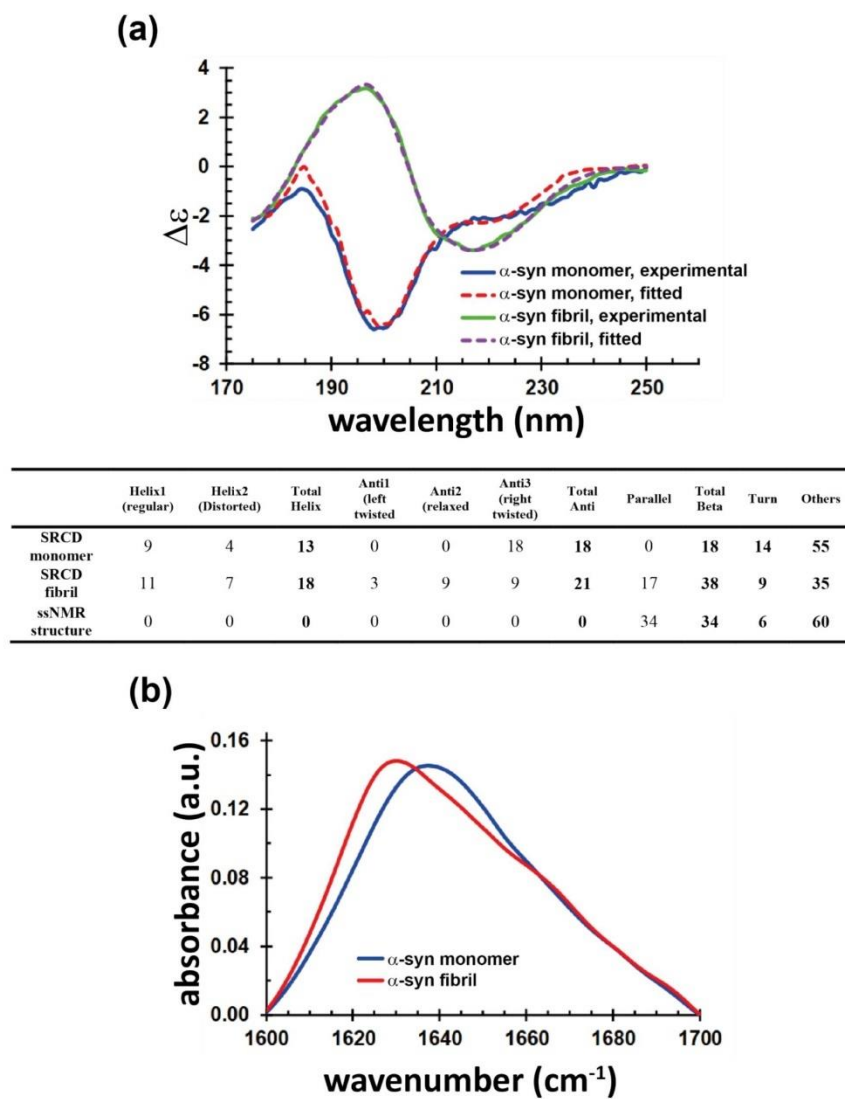


Fig. S3. Secondary structure analysis of α -synuclein (α -syn) in monomer and amyloid fibril forms. (a) SRCD experimental spectra (solid lines) were processed using *CDtool* then fitted using *BeStSel* (dashed lines). The *BeStSel* deconvoluted secondary structure composition from SRCD and ssNMR structure is shown in the table below. (b) ATR FT-IR of lyophilised samples.

Figure S4.

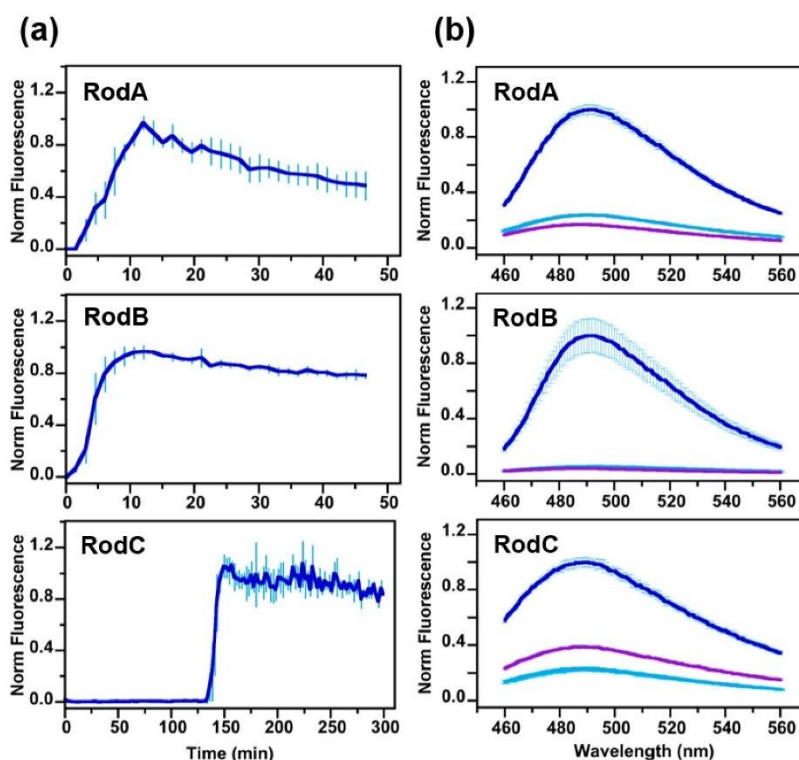


Fig. S4. Amyloid formation by RodA, RodB and RodC monitored by ThT fluorescence. Data were recorded with protein and ThT concentrations of 50 $\mu\text{g/mL}$ and 40 μM , respectively. (a) Kinetics experiments were performed at 40 $^{\circ}\text{C}$ for RodA and RodB and at 50 $^{\circ}\text{C}$ for RodC. (b) Fluorescence spectra of RodA, RodB and RodC before (violet) or after 16 h incubation under orbital mixing at 840 rpm at 25 $^{\circ}\text{C}$ (RodA and RodB) or 50 $^{\circ}\text{C}$ (RodC). Spectra in the presence or absence of an air:water interface are shown in blue and cyan, respectively. The curves of normalised ThT fluorescence intensity and errors correspond to the average and standard deviation of three independent replicates in (a) and in (b). In (b), spectra in the absence of an interface were corrected taking into account the difference of signal between the samples in the absence (400 μL) and presence of an HHI (100 μL) before incubation. In (b), the samples without an HHI do not form amyloids as shown by the lack of significant increase of ThT fluorescence after vigorous shaking during 16 hours.

Figure S5.

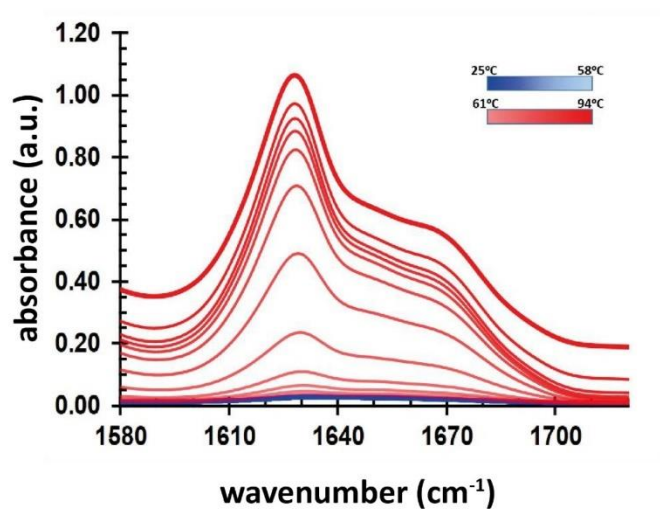


Fig. S5. Increase in ATR FT-IR signal with increasing temperature. Raw experimental spectral data collected from a solution containing DewY, and were representative of data sets collected from samples containing the other five hydrophobins. Spectra were recorded from 25 °C to 94 °C in 3-degree steps.

Figure S6.

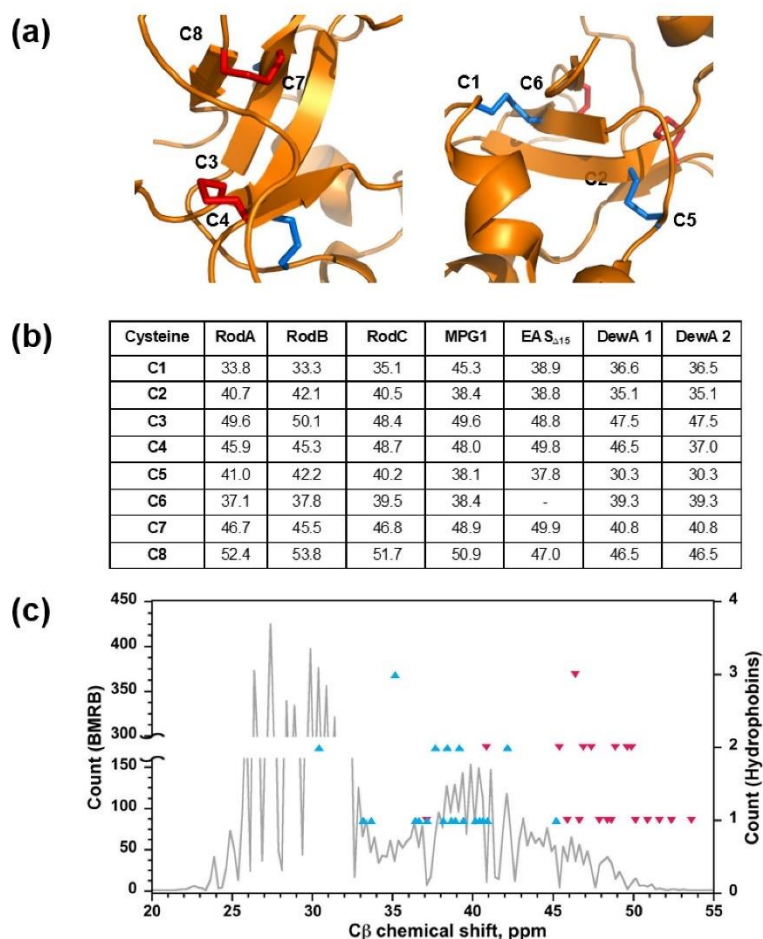


Fig. S6. Geometry of disulphide bonds and cysteine CB chemical shifts. (a) The C3-C4 and C7-C8 S-S bonds (blue) joining together contiguous strands of the central β -barrel are highly constrained by the β -sheet H-bond network and show a particular geometry compared to the more commonly observed linear arrangement of disulphides displayed by the C1-C6 and C2-C5 S-S bridges (red). The S-S (CA-CB-SG-SG-CB-CA) geometry is exemplified with two views of the structure of MPG1. The later configuration is similar for EAS _{Δ 15}, RodA and the major DewA conformer 1. (b) The C3-C4 and C7-C8 S-S bond geometry correlates with high values of CB NMR chemical shifts of cysteines C3, C4, C7 and C8 relative to the values

displayed by C1, C2, C5 and C6. (c) The comparison of the histograms of all Cys CB chemical shifts (13495 values, grey lines) deposited with the BMRB repository (excluding hydrophobins), with the corresponding chemical shifts of the six hydrophobins studied herein, indicates that indeed C3-C4 and C7-C8 (red triangles) CB chemical shifts have very high values, while C1, C2, C5 and C6 (blue triangles) show more standard chemical shifts. In (c) data were binned within 0.25 ppm intervals.

Figure S7.

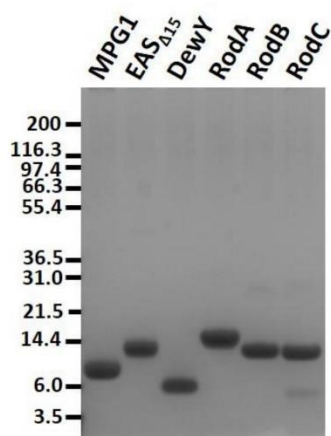


Fig. S7. SDS PAGE analysis of the purified hydrophobin preparations used to collect SRCD and FT-IR data.

3.2 Chapter 2: Hydrophobin self-assembly

3.2.1 Introduction

In the JMB paper, we characterized the secondary structure conformational changes that occur upon self-assembly of six hydrophobins including RodA-C and the dependence of the assembly on the nature of the HHI/AWI where auto-association takes place. In this chapter, I will describe the ongoing comparative study of the self-assembly of these *A. fumigatus* hydrophobins, with particular emphasis on RodC.

Although, we described in the manuscript that RodB and RodC, like it was previously shown for RodA, do form fibers and bind the amyloid reporter dye ThT, it had never been shown that the rodlets/fibers formed by the three proteins are based on the cross- β structure. Here, I will first present the confirmation that RodA-C do form amyloids and describe the morphology of their assemblies on different interfaces by EM and AFM.

Then I will briefly present, the structural work on the starting and end points of the self-assembly of RodC, *i.e.* the monomeric native state and the functional amyloid state, respectively. The native monomeric form of RodC is being studied by solution NMR and we have tried to study its amyloid state by ssNMR.

In the main part of this chapter I will focus on the mechanism of self-assembly of hydrophobins (principally of RodC) (i) based on the dependence of the amyloid formation kinetics on concentration and temperature. Results will be analyzed on the light of the requirement of a HHI or AWI interface for self-assembly and the associated conformational changes that occur; (ii) the effect of reducing the disulfide bonds of RodC on fibrillation kinetics (iii) the effect of point-mutations on fibrillation kinetics and the analysis of the capacity of RodC-derived peptides to pinpoint important results for amyloid formation; (iv) the effect of major cell wall components (glucans, chitin, a synthetic melanin analog...) on RodC amyloidogenesis.

3.2.2 *A. fumigatus* Class I hydrophobins form *bona fide* amyloids

The sequences of RodA, RodB and RodC are typical of Class I hydrophobins and as such it is predicted that the 3 proteins should form amyloid fibers based on a cross- β skeleton. To confirm that indeed the proteins form fibers we checked the three current experimental criteria that in the absence of the structure are used to define amyloids: morphology (electron

RESULTS & DISCUSSION

microscopy), binding to amyloid reporter dyes (ThT) and the cross- β diffraction pattern analyzed by fiber XR diffraction.

RodA-C bind ThT as previously observed in the laboratory, described in the literature (Pham *et al.*, 2018; Valsecchi *et al.*, 2019b) or herein. Although amyloid reporter dyes such as ThT are very useful probes to reveal the cross- β structure, these are not totally specific and can occasionally also bind to other types of structures and produce false negatives (Biancalana and Koide, 2010; Gade Malmos *et al.*, 2017).

To observe the morphology of hydrophobin assemblies, we used negative stain EM and AFM. Hydrophobin samples were prepared from monomers by drying on a solid support (AFM) or in solution by vigorous shaking to increase the air-water interface (EM).

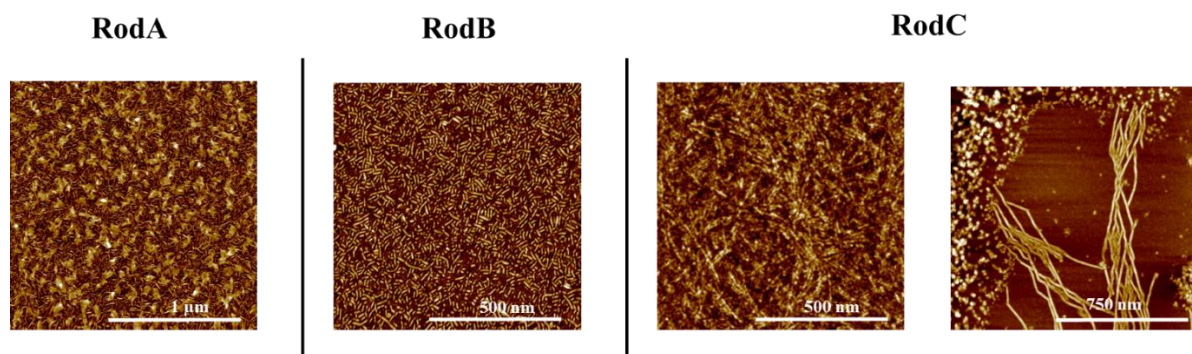


Fig. 29. AFM of RodA-C self-assemblies.

RodA and RodB monomer samples in H₂O were deposited on a hydrophobic surface (HOPG, highly oriented pyrolytic graphite) and RodC samples on a hydrophilic surface (mica) at a concentration of 5 μg/ml, dried overnight at room temperature and 2 h at 70 °C before imaging. AFM micrographs were recorded by Vincent Duprès (Institut Pasteur de Lille).

When dried on a surface (Fig. 29), the three hydrophobins form fibers that fulfill the characteristics of amyloids. Nevertheless, their appearance and surface preferences are quite distinct. While RodA and RodB prefer a hydrophobic surface (HOPG) but can form fibers on the hydrophilic mica (not shown), RodC only forms fibers on mica. RodA and RodB form rodlet-like structures that completely cover the surface and show lateral association forming films reminiscent of the rodlet layer formed by RodA at the surface of the spores. While HOPG or mica are regular surfaces that cannot mimic the complexity of the spore surface, the morphology of these *in vitro* rodlets is very similar to that observed for RodA on *A. fumigatus* conidia, albeit with different dimensions. In contrast with RodA and RodB, RodC assemblies show more variability. RodC can form rodlets that are hard to visualize on AFM, as well as in

RESULTS & DISCUSSION

other preparations, very long fibers together with protein domain clusters. RodC atomic force micrographs indicate that RodC self-assemblies under these conditions are heterogeneous. The different interactions and nature of the self-assemblies of hydrophobins with different surfaces are in line with our published observations on SRCD and FT-IR experiments (Pham *et al.*, 2018).

In AFM conditions, the proteins self-assemble in the presence of two different interfaces, the solid one (HOPG, mica) and the one with air. The situation is different when self-assemblies are prepared *in vitro* from monomer solutions, in which there is basically only the interface with air.

The self-assembly's morphology of samples prepared in solution imaged by TEM are shown in Fig. 30.

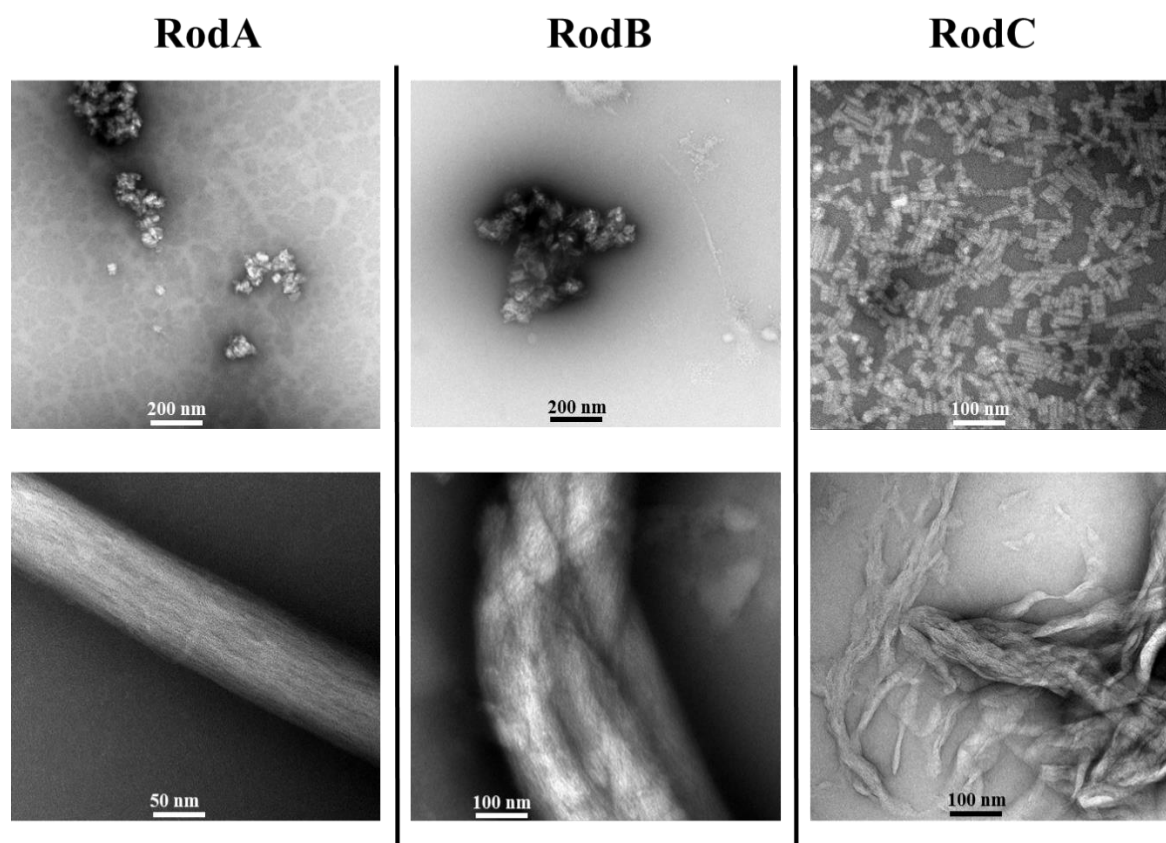


Fig. 30. Negative stain TEM of RodA-C self-assemblies.

Top, short-like rodlets. Bottom, long fibers. Self-assemblies were prepared in H₂O from monomers samples (25 µg/mL) after 2 h shaking at 50 °C. Four µL droplets were deposited on glow-discharged carbon coated copper grids and after 2 min incubation, stained with 2% uranyl acetate.

RESULTS & DISCUSSION

Despite many efforts to try sample preparation (concentrations, glow discharge, incubation and washing) and staining (dyes, incubation time...), the three hydrophobins remain difficult to image by negative stain (and cryo-EM) and results are variable. For some unknown reason, self-assemblies are not generally retained on the grids. Nevertheless, it is possible to observe fibers for the three proteins. Short rodlets (50 nm long and ~20 nm wide) with some degree of lateral association can be observed for the three proteins. These rodlets, although shorter and larger, are reminiscent of those observed for RodA on *A. fumigatus* conidial surface (Hess and Stocks, 1969; Valsecchi *et al.*, 2019b). The RodC sample in Fig. 30 shows a higher degree of order and lateral association than the rodlets formed by RodA and RodB that associate into clumps. Very long bundles of fibers were also observed for the 3 proteins with ~1 μm long and 70-100 nm wide dimensions.

XR fiber diffraction patterns (Fig. 31) were recorded from dried hydrophobins samples prepared in solution with the same conditions used for EM and ThT binding. The three proteins display the characteristic XR cross- β reflections at 4.7 \AA and 10 \AA (Fig. 31) indicative of the inter β -strand spacing in the direction of hydrogen bonding and inter- β sheet distances (side chain packing, as shown in Fig. 5 schematically), respectively. The reflections are observed as rings instead of arcs because the samples were not aligned. In addition, RodC shows a reflection at 34 \AA , which could arise from the repetitive subunit.

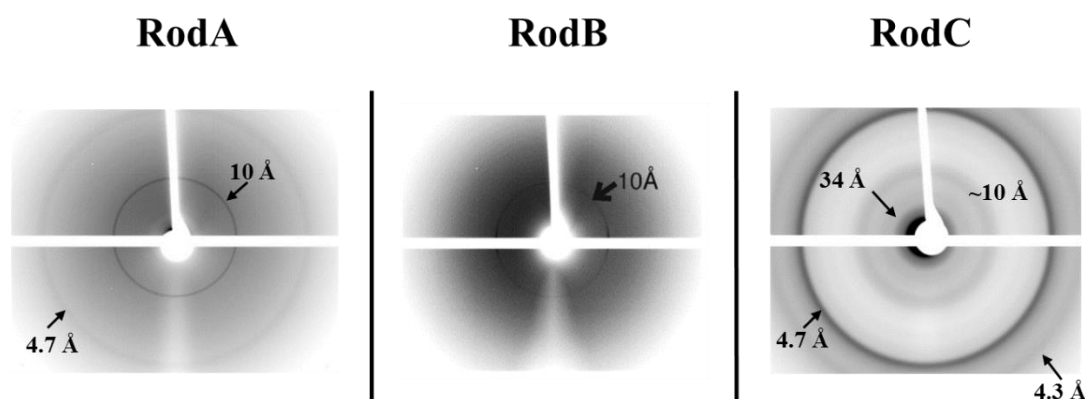


Fig. 31. RodA-C XR fiber diffraction

Dry hydrophobin samples (200 μg) were prepared from monomer samples (25 $\mu\text{g}/\text{mL}$ in 50 mM CH_3COONa pH 5) by vigorous shaking as described in Materials and Methods, and then dried under a nitrogen flux. XR diffraction patterns were collected at the IECB (collaboration Antoine Loquet).

In summary, RodA, RodB and RodC self-assemblies are *bona fide* amyloid fibers based on a cross- β core.

3.2.3 Solution and ssNMR

3.2.3.1 Solution NMR of RodC

To fully understand the mechanism of self-assembly of hydrophobins, it is necessary to know the structure of the monomers from which self-assembly takes place and the final amyloid state, which is the biologically functional form. To address the structure of the monomeric form we use solution NMR and to tackle the structure of the amyloid state we use solid state NMR (ssNMR, see next section) and we have tried TEM (negative and cryo-EM). The comparative study of the secondary structure of RodA-C determined from NMR backbone and CB chemical shifts using TALOS-N is presented in the JMB manuscript (Chapter I).

The spectra of the monomer of RodC show relatively large line-widths. Although RodA-C have a similar size (RodB 129 residues, RodC 134 residues, RodA 142 residues), RodA and RodB produced high quality spectra at 25 °C and the spectra of RodC were of very poor quality at this temperature. Heating the sample to 35 °C, alleviated this problem and allowed past work by Régine Dazzoni in the laboratory to assign the resonances of ~80% of the backbone and CB atoms of RodC. During my PhD, I extended this work to assign the resonances of 90 % of the backbone atoms, working at 45 °C (Fig. 32). The signal linewidth depends on the transversal relaxation rate (R_2) that in turn depends on the rate of molecular tumbling ($1/\tau_c$, where τ_c is the tumbling correlation time) and the internal dynamics of the corresponding atoms. The faster the tumbling, the lower the R_2 and the lower the linewidth. As expected with a faster molecular tumbling at increasing temperatures, the signals of RodC become sharper at higher temperatures. Nevertheless, at 25°C, RodC presents much wider signals than RodA and RodB, so the origin of this linewidth must be either a different molecular weight (dimerization...) or chemical exchange on the microsecond-millisecond time range. Several lines of evidence indicate that chemical exchange between two or more conformations is at the origin of the line broadening. First, on gel filtration (Superdex 75), the retention volume of RodC (12.5 mL) is smaller than the retention volume of RodA (11.7 mL) and slightly bigger than the retention volume of RodB (12.4 mL); second, the τ_c of RodC determined from the mean ^{15}N R_2/R_1 of RodC is 8.9 ± 0.6 ns, in agreement with a monomeric protein of 134 residues; third, the linewidths in RodC ^{15}H - ^{15}N HSQC spectra are broader at 800 MHz than at 600 MHz as

RESULTS & DISCUSSION

expected for exchange broadening. While we cannot assess the nature of the exchanging species (aggregates?), we think that this phenomenon is linked to slow motions of the disulfide bridges because several amide signals close to cysteines are exchanged broadened including the amide signal of the cysteine C8 (^{148}C).

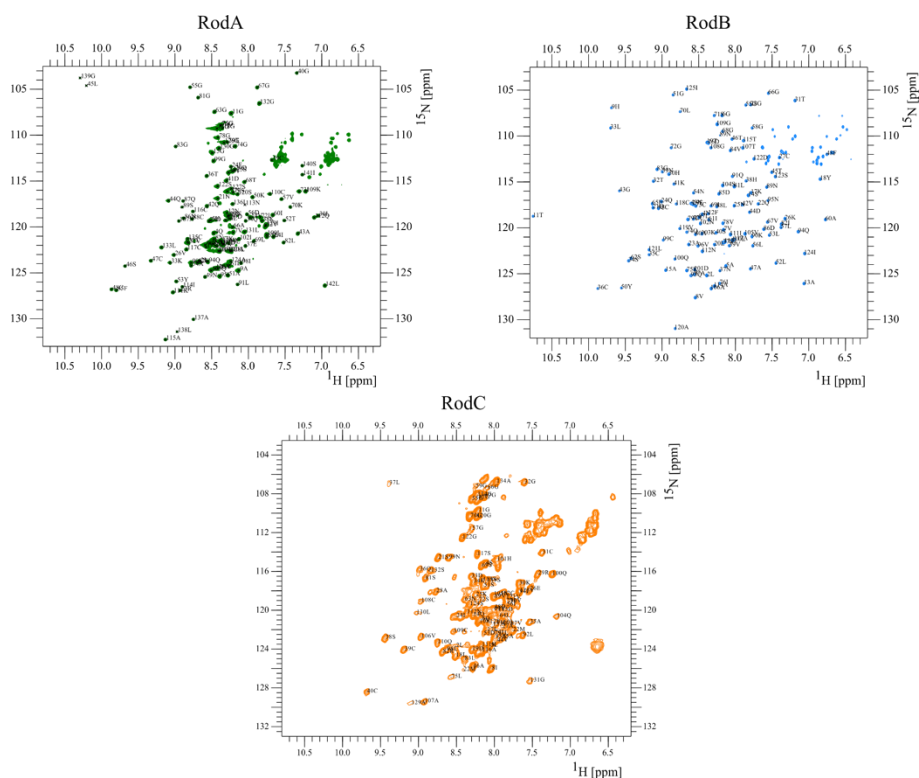


Fig. 32. ^1H - ^{15}N HSQC spectra of RodA (25 °C), RodB (25 °C) and a SOFAST experiment for RodC (45 °C).

The assignments of the side chains of the N/Q amides and arginine guanidinium amines are not displayed for the sake of clarity.

The relatively low dispersion of the peaks and the chemical exchange phenomenon renders difficult the assignment of RodC resonances, however we have assigned most of the backbone resonances and we are confident that it will be possible to obtain the structure of RodC in the near future. The comparison of the secondary structure of RodC, RodA and RodB, the knowledge from NMR chemical shifts and electrospray mass spectrometry that the 8 cysteines of RodC are oxidized, the determination by NMR of the disulfide pairing of RodC and the similarity of the cysteine CB chemical shifts that are linked to the highly constrained C-C and C-C bonds that link strands of the β -barrel core in RodA, MPG1, DewY and EAS Δ 15, indicate that the structure of RodC is similar to the structure of RodA (and RodB), with a central β -

RESULTS & DISCUSSION

barrel core and one α -helix upstream the first cysteine. RodC lacks, however, an α -helix shown by RodA in the inter-cysteine region C3-C4.

The internal dynamics of RodC backbone on the ns-ps time range were predicted from chemical shifts using the random coil index (RCI) method proposed by (Berjanskii and Wishart, 2005). The RCI parameter is calculated with an empirical correlation using averaged chemical shifts of the CA, C', HA, CB, and backbone ^{15}N atoms (Fig. 33).

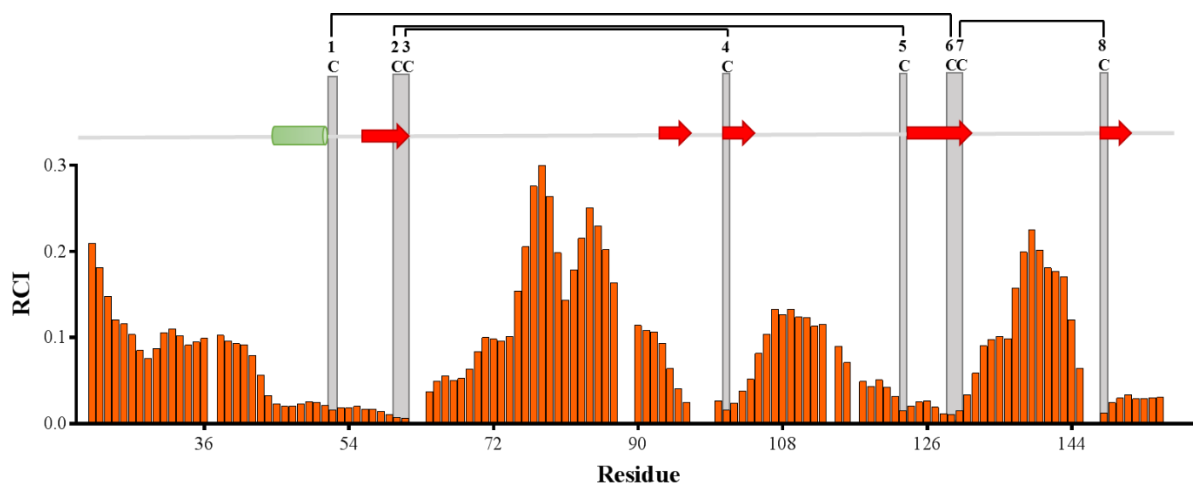


Fig. 33. RCI as a function of residue number.

A high RCI values denotes flexibility and inversely a low RCI value indicates rigidity of the backbone.

From the RCI values shown by RodC, we can conclude that the central β -barrel core of RodC, the α -helix and the other regions constrained by the disulfide bridges are rigid and the N-terminal region (22-36) and the inter-cysteine loops C3-C4 (62-92), C4-C5 (101-122) and C7-C8 (131-149) are flexible. β -Sheets are shown as red arrows and α -helices as green cylinders. The idiosyncratic pattern of cysteines is shown in grey bars.

3.2.3.2 Solid state NMR of RodA-C hydrophobins

The amyloid state is the biologically active form of hydrophobins in fungi, including *A. fumigatus*. Therefore, the final goal and the most challenging, is to solve the structure of the rodlet state. In order to characterize the structure of the rodlets of the three proteins, as well as to multiply the chances of obtaining homogeneous samples amenable to signal assignment and structural work, we studied the three proteins by ssNMR. We thus prepared doubly labelled (^{13}C and ^{15}N) RodA-C rodlets *in vitro*. This work was performed in conjunction with Isabel

RESULTS & DISCUSSION

Valsecchi who prepared RodA and RodB rodlets and the Antoine Loquet team (IEB, Bordeaux) who performed the ssNMR experiments. ssNMR is based on carbon detection and because of the low gyromagnetic ratio of this nucleus ($1/4^{\text{th}}$ of the proton gyromagnetic ratio) is a very insensitive method and requires high amounts of proteins. Experiments shown below were performed with samples containing between 4 (RodB) and 14 mg (RodC) of doubly labeled self-assembled proteins.

As a first characterization, 1D ^{13}C CP (Cross-Polarization) and INEPT (Insensitive Nuclei Enhanced by Polarization Transfer) experiments were performed spinning at the magical angle. The CP experiments detect rigid signals for carbons involved in rigid species and the INEPT experiment reports on flexible species (Fig. 34). The three proteins show similar 1D CP spectra with resonances typical of proteins (carbonyls: 170-180 ppm; aromatics: 140-110 ppm; aliphatics: 70-10 ppm) indicating that the samples contain rigid structures. The INEPT experiments done on the same samples effectively display no signal, showing the absence of significant amounts of flexible species and of flexible regions within the rigid species.

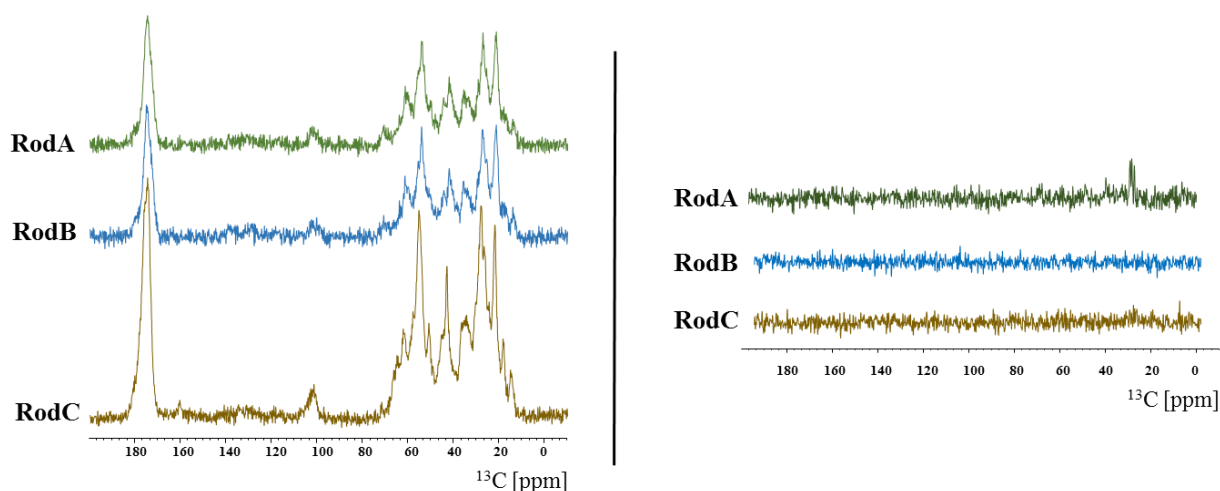


Fig. 34. Carbon CP-MAS (left) and INEPT (right) experiments of RodA, RodB and RodC.

To further assess the quality of the spectra, 2D PDSD (Proton-Driven Spin Diffusion) were recorded (Fig. 35).

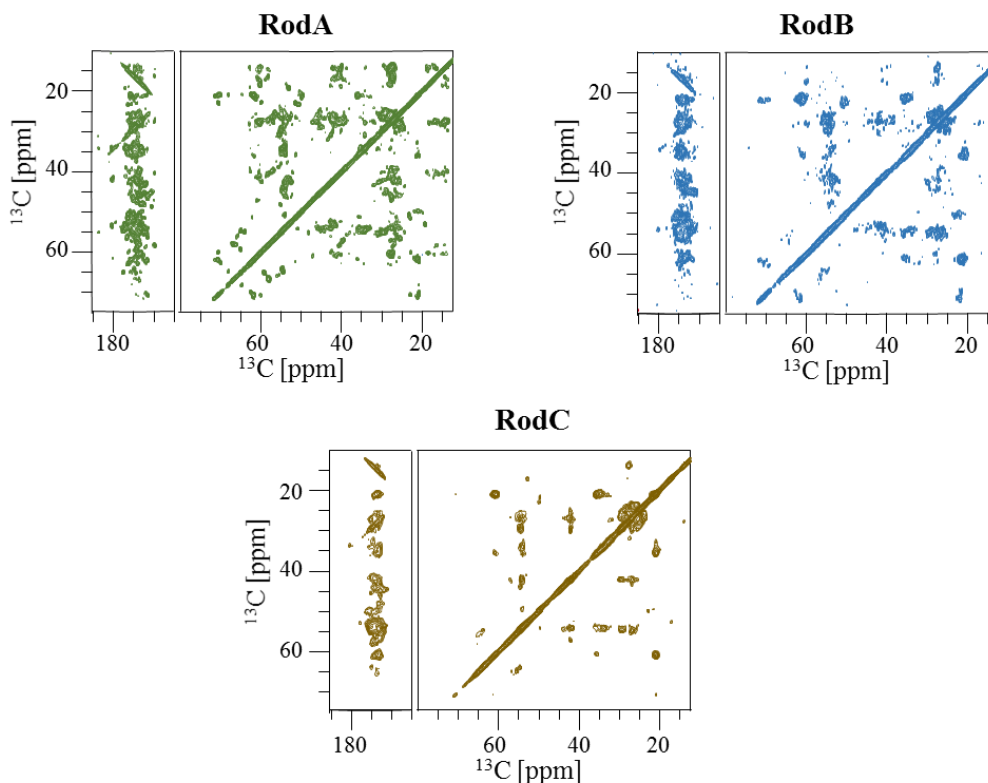


Fig. 35. Carbon-carbon PDSD spectra of RodA-C amyloids.

The PDSD spectrum of RodA (~ 8 mg of protein) shows abundant signals with a relatively low line-width suggesting that the sample is homogeneous. Furthermore, the spectrum also shows good dispersion suggesting the feasibility of the assignment of its ssNMR spectra. Although the amount of RodB was low (~4 mg), its PDSD also shows good dispersion and a moderate line-width. In contrast, the RodC spectrum (~ 14 mg) shows only a limited number of cross-peaks with very broad lines, indicating conformational heterogeneity and hampering further analysis of its structure by ssNMR.

RodA is currently being studied by ssNMR. Isabel Valsecchi has prepared a perdeuterated triply labelled (^{13}C , ^{15}N , ^2H) sample with back-exchanged amide protons that has been used by our collaborators to record proton-detected experiments with a high-speed rotor. Importantly, the proton and carbon detected spectra of RodA indicate that there is only one species and that the preparations are reproducible. Over 70 spin systems (out of 142) have been unambiguously identified and will be sequentially assigned in the next future to calculate the structure of the amyloid cross- β core.

3.2.4 Self-assembly kinetics of Rod hydrophobins

3.2.4.1 RodA-C self-assembly kinetics and importance of the AWI

To get insights into the mechanism of amyloid formation, we have performed amyloid fiber formation kinetics experiments monitored by ThT fluorescence. We have compared the kinetics of the three close homologs, analyzed the importance of the air-water interface (generally abbreviated HHI for hydrophobic hydrophilic interface, or AWI, for air-water interface), investigated the effect of concentration and, for RodC, we have performed a mutational analysis to pinpoint the regions involved in amyloidogenesis and characterized the effect of different MCW on its self-assembly.

Experiments at different pH and temperature for the three hydrophobins (previous work in the lab and in M. Sunde lab, University of Sydney and during my PhD) led to appropriate conditions to form amyloids and study the fibrillation kinetics.

The kinetics of amyloid formation of RodA-C are shown in (Fig. 36). Kinetics experiments were carried out at the temperature in which the monomers of RodA, RodB and RodC are stable (*i.e.* don't unfold) as stated by ^1H - ^{15}N HSQC NMR spectra (RodA and RodC) and SRCD melting experiments (RodA-C).

RESULTS & DISCUSSION

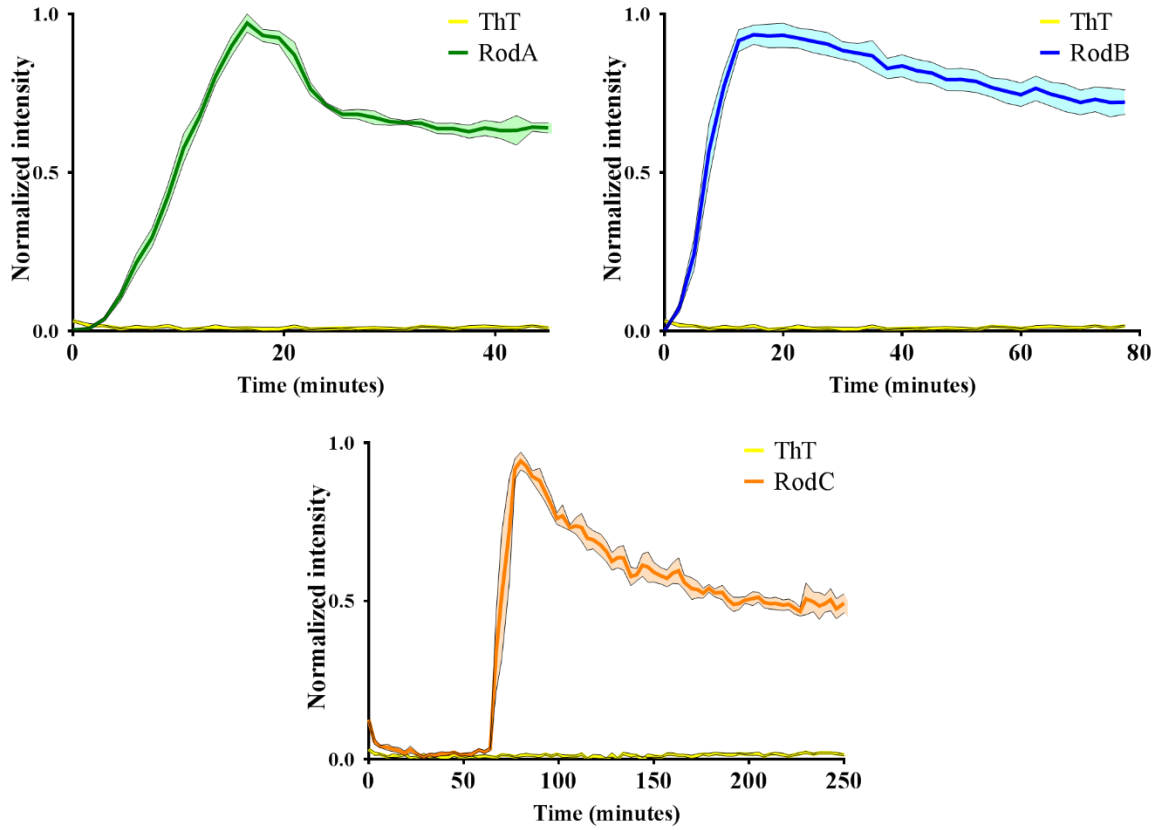


Fig. 36. RodA-C amyloid formation monitored by ThT fluorescence kinetics.

Experiments were performed using black 96-well flat-bottom plates (Greiner) with proteins at a final 50 $\mu\text{g}/\text{mL}$ (RodA and RodB) or 25 $\mu\text{g}/\text{mL}$ (RodC) concentration in H_2O (RodA and RodB) or 20 mM sodium acetate (pH 5.0 for RodC) and 40 μM ThT. Kinetics were carried out at 50 $^{\circ}\text{C}$ for RodC and 40 $^{\circ}\text{C}$ for RodA and RodB. Fluorescence intensity has been normalized. The curve and the envelope represent the mean \pm SEM (standard error from the mean) of five replicates

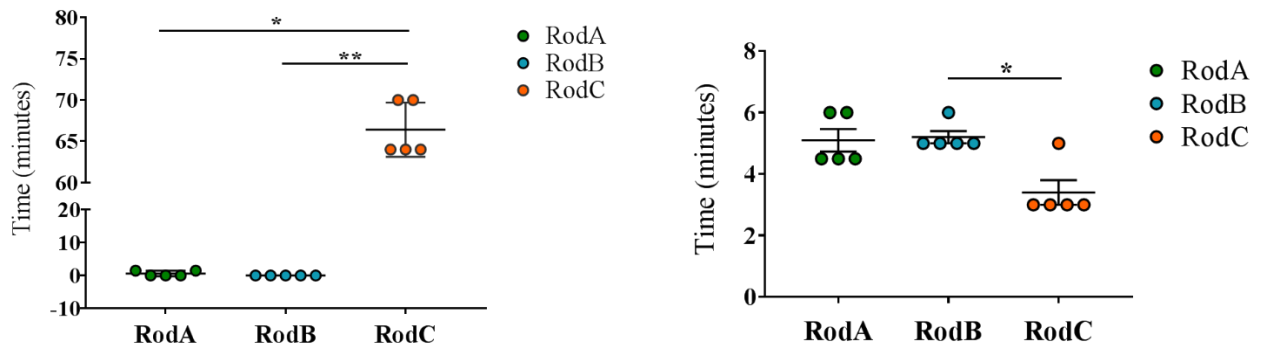


Fig. 37. Lag phase time and half-time of amyloid fibril formation.

RESULTS & DISCUSSION

Left, RodA-C lag phase time (*i.e.* time to reach the growth phase). Right, ($t_{1/2}$, time to reach half maximum fluorescence after the lag phase). Data are derived from five replicates. Statistical analysis: non-parametric Kruskal-Wallis test plus *post-hoc* Dunn test for multiple comparisons (circles=data, mean \pm SEM; n = 5, **p < 0.01, *p < 0.05).

The kinetics of RodA-C fibrillation show a sigmoidal curve indicating that amyloidogenesis is a nucleated phenomenon for the three proteins. RodA and RodB show very fast kinetics (Fig. 37) with a very short lag phase (0.6 min or undetectable, respectively), whereas RodC displays a much longer lag phase (66 ± 3 min) even at a higher temperature. These data indicate that relative to RodA and RodB, the nuclei that are competent for fibrillation are highly unstable and hence difficult to reach and accumulate for RodC, or that off-pathway intermediate species may form. In contrast, even though experiments were done at different temperatures and different concentrations, the growth phase shows pretty similar rates as evidenced by the half-times ($t_{1/2}$) observed for the three proteins. The growth phase is indeed very stiff in all instances ($t_{1/2} < 6$ min), suggesting an autocatalytic process.

The final plateaus of the kinetics profiles show a decrease in ThT fluorescence, a decrease that could *a priori* be attributed to a dissociation and unfolding of the fibers or to a change in conformation of the fibers that would result in a lower quantum yield of bound ThT. Although we cannot completely discard fiber modifications or unfolding at late stages of the kinetics, we attribute this phenomenon to a decrease in detectable fibers caused by fibers sticking to the well wall. In agreement with this, the plateau becomes flatter at higher protein concentrations, suggesting that as concentration increases, the relative amount of fibers adhering to the well surface, which ultimately becomes saturated, is smaller. This can be appreciated below in Fig. 40, which shows the kinetics of RodC at different concentrations.

ThT binds and reports on amyloid fibers only, so during the lag phase as observed with ThT many non-fibrillar species of different size can form, including propagation-competent species (nuclei), as well as fibers at concentrations below detection. In this respect, it is interesting to note that we observed by negative stain EM that native RodA and RodC monomers can form amorphous aggregates with diameters ranging from 10 to 20 nm on EM grids Fig. 38. Although these structures most likely form during the incubation with the grid and may not be related at all to the intermediates formed during fiber formation, EM data definitively shows that both proteins can form small assemblies that resemble species that appear during the formation of fibers of other proteins (Juárez, Taboada and Mosquera, 2009).

RESULTS & DISCUSSION

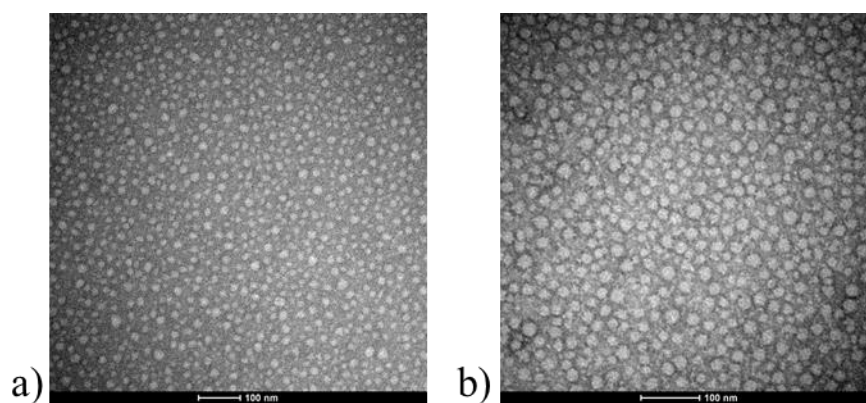


Fig. 38. TEM of RodA- and RodC-monomer samples.

Protein samples of RodA (a) and RodC (b) at 50 $\mu\text{g/mL}$ were incubated on the grids for 10 min and stained with 2% uranyl acetate.

Mathematical models of amyloid formation have provided many insights into the mechanism of amyloid formation (Cohen *et al.*, 2013; Buell *et al.*, 2014; Arosio, Knowles and Linse, 2015; Törnquist *et al.*, 2018). During the lag phase, primary nucleation is normally the main mechanism of nuclei formation and the accumulation of detectable short microfibers/nuclei represents the rate limiting step. As mentioned before, for amyloid formation in solution, a longer lag phase as observed for RodC could be intrinsic to the protein, with very unstable propagation-prone nuclei or could be due to the accumulation of off-pathway intermediates. In the case of hydrophobins, the situation may be more complicated because nuclei and fiber formation occurs at an HHI or air-water interface (AWI). Indeed, in our JMB paper presented in Chapter 1, we showed that in solution RodA-C, like previously shown for DewA, MPG1 and EAS $_{\Delta 15}$, require an AWI to form amyloids. Indeed, a simple experiment in which RodA-C monomers were vigorously shaken under the same conditions either (i) on wells completely filled with the sample and covered to avoid an AWI or (ii) with some air in the wells indicated that in the absence of an AWI, fibers do not form Fig. 39.

RESULTS & DISCUSSION

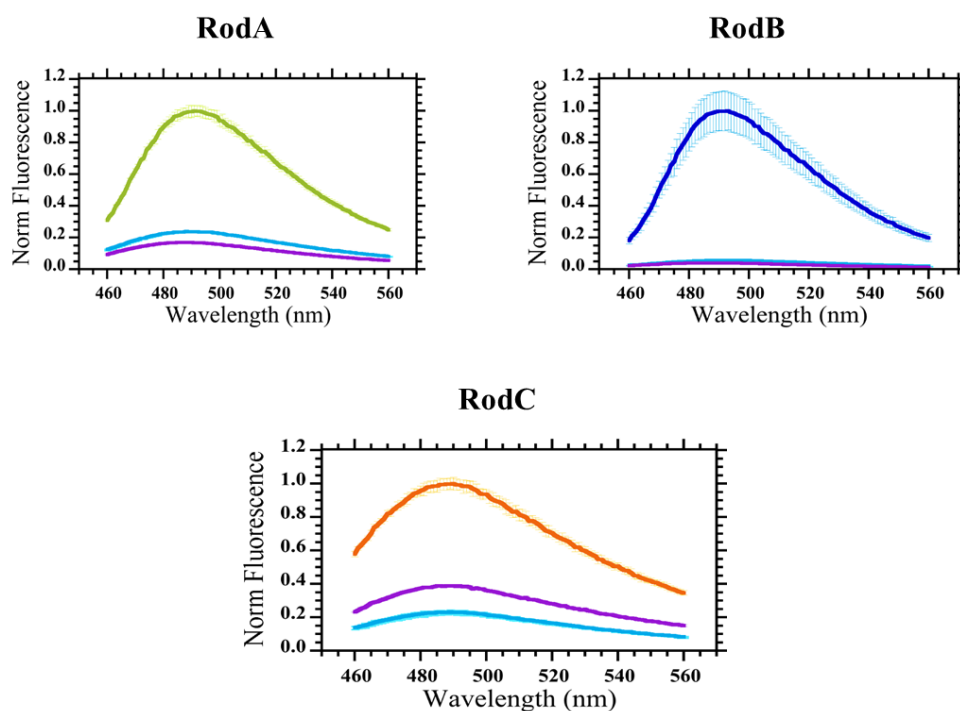


Fig. 39 . Influence of an AWI on RodA-C fiber formation.

RodA-C amyloids revealed by ThT fluorescence spectra for samples before shaking (violet) and after shaking in the absence (cyan) or presence (RodA in green, RodB in blue and RodC in orange) of an interface. Samples were shaken at 840 rpm and 25°C (RodA-B) or 50°C (RodC) for 16 hours in well plates completely filled (400 μ L, no AWI) or partially filled with sample (100 μ L, AWI). The fluorescence was corrected for the difference in volume

The primary nucleation for Rod hydrophobins is heterogeneous, as described in the literature (Törnquist *et al.*, 2018), in contrast to homogeneous primary nucleation that happens in solution and the availability of the AWI has to be considered.

During the growth phase, in addition to heterogeneous primary nucleation, elongation and fragmentation, another mechanism of fiber formation can dominate fibrillation: monomer-dependent secondary nucleation. In this mechanism, already formed fibers serve as catalytic surfaces to template the formation of new fibers from monomers. Here again, in the case of hydrophobins the situation may be more complicated because the AWI interface has to be considered along with another phenomenon not observed in general for other amyloids: the lateral association of fibers to form layers. ThT fluorescence only reports on the evolution of available cross- β structures and cannot directly inform on the lateral association of the fibers.

RESULTS & DISCUSSION

To probe the existence of off-pathway species, obligate intermediates and the effect of the interface in RodC fiber formation, we analyzed its fibrillation kinetics at different protein concentrations Fig. 40 and at different shaking rates that produce different available AWI areas.

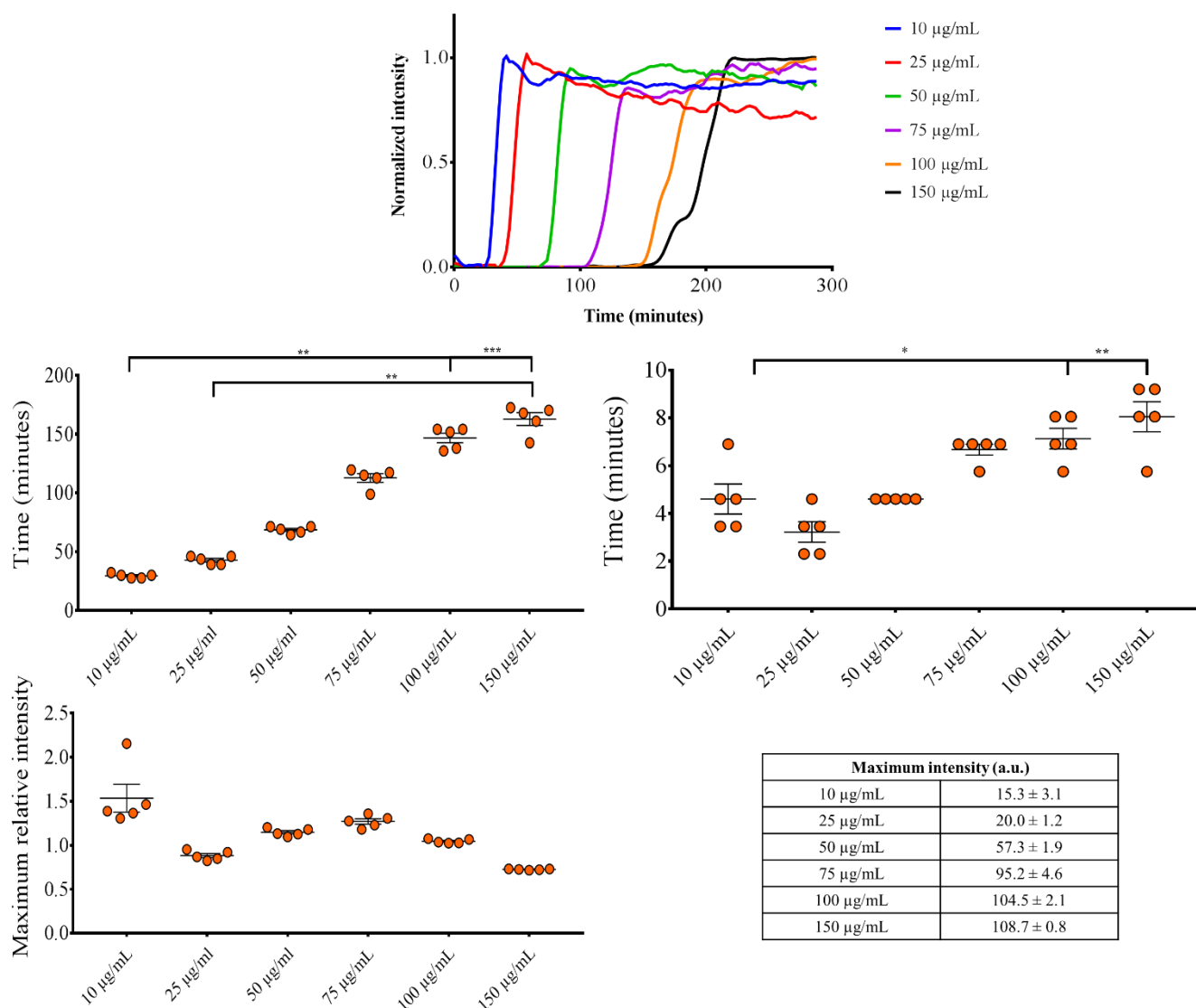


Fig. 40. RodC fiber formation kinetics at different protein concentrations.

Kinetics were followed by ThT fluorescence in the presence of increasing RodC concentrations (from 10 to 150 µg/mL). Experiments were performed in 20 mM sodium acetate pH 5.0 supplemented with 40 µM ThT. Five replicates were recorded for each protein concentration. Top, representative kinetics traces (normalized fluorescence intensity vs. time). Center, lag-phase time (left) and growth phase half-time (right) as a function of protein concentration. Bottom, maximum intensity corrected by concentration. The maximum intensities are shown in the table. Statistical analysis: non-parametric Kruskal-Wallis test plus post-hoc Dunn test for multiple comparisons (circles=data, mean ± SEM; n = 5, ***p < 0.001, **p < 0.01, *p < 0.05).

RESULTS & DISCUSSION

In contrast with what is expected for a high-order reaction like protein self-assembly, the lag and growth phases become slower with increasing concentrations, indicating that fiber formation is auto-inhibited. Indeed, between 10 and 100 μM the lag phase varies from 29 ± 2 to 163 ± 11 minutes and the growth phase half-time from 5 ± 1 to 8 ± 1 minutes. Between 100 and 150 $\mu\text{g/mL}$, the effect of concentration on the kinetics of both phases seems to plateau. The effect of concentration is more important on the lag phase than on the growth phase.

Importantly, the maximum of fluorescence at the final plateau is proportional to the concentration, or, as shown in Fig. 40, is effectively constant after correction by concentration. This result eliminates the possibility of the existence of non-productive off-pathway intermediates in the self-assembly of RodC, which could in principle explain the reduction in primary nucleation rates observed with the increase in protein concentration. Thus, the decrease in primary nucleation rate with concentration could only arise from surface saturation and/or an obligatory (-ies) oligomeric intermediate (s) that is (are) not self-propagation prone.

Because the growth phase rate is very fast and primary nucleation is very slow, this later phenomenon cannot significantly contribute to fibrillation during this phase and can thus not explain the negative correlation between rate and concentration. Both elongation and especially secondary nucleation are monomer-concentration dependent phenomena in which the rate should increase with concentration (a small dependence of concentration is expected for elongation if monomer concentration is not limiting). Nevertheless, at high monomer concentrations relative to the available fibril auto-catalytic surfaces, secondary nucleation should become independent of the concentration, in a phenomenon called supersaturation (Törnquist *et al.*, 2018). Although at high concentrations supersaturation can reduce or abolish the dependence of the secondary nucleation rate on concentration, its rate should not diminish with increasing concentrations. Hence, these observations point towards surface saturation. In agreement with this, although not studied systematically, we have observed for RodC, as well as for RodA and RodB, that fibrillation kinetics are slower at lower shaking speeds and faster at faster shaking speeds (not shown) and that increasing the sample volume added to wells (from 100 to 200 μL , for instance) to decrease the available surface per monomer while keeping the shaking rate constant, results in longer lag and growth phases. We can thus conclude that the availability of the AWI is limiting primary and secondary nucleation at 'high' concentrations ($> 25 \mu\text{g/mL}$). From our data and this qualitative analysis, we cannot get insights of the effect of surface saturation on fibril elongation. Furthermore, lag- and growth-phase

RESULTS & DISCUSSION

times for RodA and RodB fibrillation kinetics show a similar dependence on concentration and on reduction of the available AWI surface (not shown).

In summary, although full comprehension of the relative importance of the different microscopic events leading to fiber formation would require to fit data to master equations with a model describing these phenomena and including primary and secondary nuclei formation and fibril elongation at an interface, the qualitative analysis that we propose here indicates that (i) oligomerization and conformational changes necessary to form self-propagating nuclei occur at the AWI; (ii) the availability of surface limits fiber formation at high hydrophobin concentration ($> 25 \mu\text{g/mL}$, under the conditions that we used) and is at the origin of the observed self-assembly auto-inhibition ; (iii) the growth phase is very fast for RodA-C and is dominated by an autocatalytic process (secondary nucleation); (iv) no significant off-pathway intermediates accumulate; (v) the relatively long lag-phase observed for RodC is due to a high transition barrier necessary to form detectable nuclei.

3.2.4.2 Effect of the temperature on RodC self-assembly

Temperature effects can be useful to understand the mechanistic of fiber formation. In the case of RodC, however, this is difficult to perform because the duration of the lag phase becomes highly variable when decreasing the temperature (Fig. 41). In contrast to the lag phase, the different replicates show a homogeneous growth phase at 40 °C. Nevertheless, the lag phase of fibrillation at 40 °C is significantly longer than at 50 °C. Similarly, the half-time of the growth phase, becomes bigger at 40 °C (21 ± 2 min) with respect to 50 °C (3 ± 1 min) at the same concentration. Although a systematic study should be performed to draw conclusions, it can be hypothesized that the energetic barriers that are limiting the rate of both phases are of entropic origin and involve hydrophobic interactions.

RESULTS & DISCUSSION

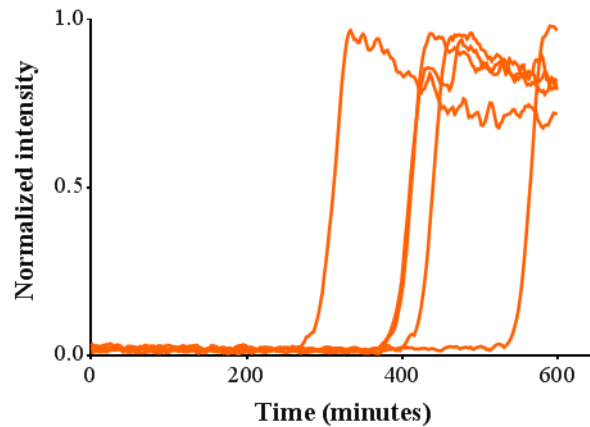


Fig. 41. RodC fiber formation kinetics experiments at 40 °C.

Experiments were conducted at 40° C with a concentration of 50 µg/mL. All other experimental conditions were the same as in Fig. 40.

3.2.4.3 Unfolded Rod hydrophobins also form amyloid fibers

Based on the observation that the unfolded and reduced form of the hydrophobin SC3 from *S. commune* forms amyloid fibers faster than the native monomer, it has been proposed that disulfide bridges of the native monomeric form serve to prevent premature self-assembly before secretion (De Vocht *et al.*, 2000). This proposition was based on the observation that *in vitro*, reduced SC3 self-assembles faster than the native disulfide bonded protein and that in *S. commune* mutants with SC3 cysteine mutations, protein aggregates accumulate within the spores. In fungi, as in other eukaryotes, disulfide bridges are formed in the endoplasmic reticulum prior to their secretion. Although there's a lack of information on hydrophobin secretion to the cell wall, the presence of a signal peptide in RodA-C suggests a regulated process. After finding that, like SC3, reduced and unfolded RodA is able to form amyloids *in vitro*, albeit with a different morphology, Valsecchi *et al.*, 2019b showed that *A. fumigatus rodA* mutants with one or four cysteines mutated to serine (preventing the formation of one or 4 native S-S bonds), did not present rodlets on the spore surface and could not detect RodA in the cell wall.

Here we wanted to study whether RodB and RodC are able to form fibers *in vitro* under reducing conditions and to compare the kinetics of fibrillation under native and reducing conditions for the three proteins. We used 5 mM DTT to perform kinetics assays, a reducing agent concentration shown by mass spectrometry to completely reduce and by ¹H -¹⁵N HSQCs to completely unfold RodA.

RESULTS & DISCUSSION

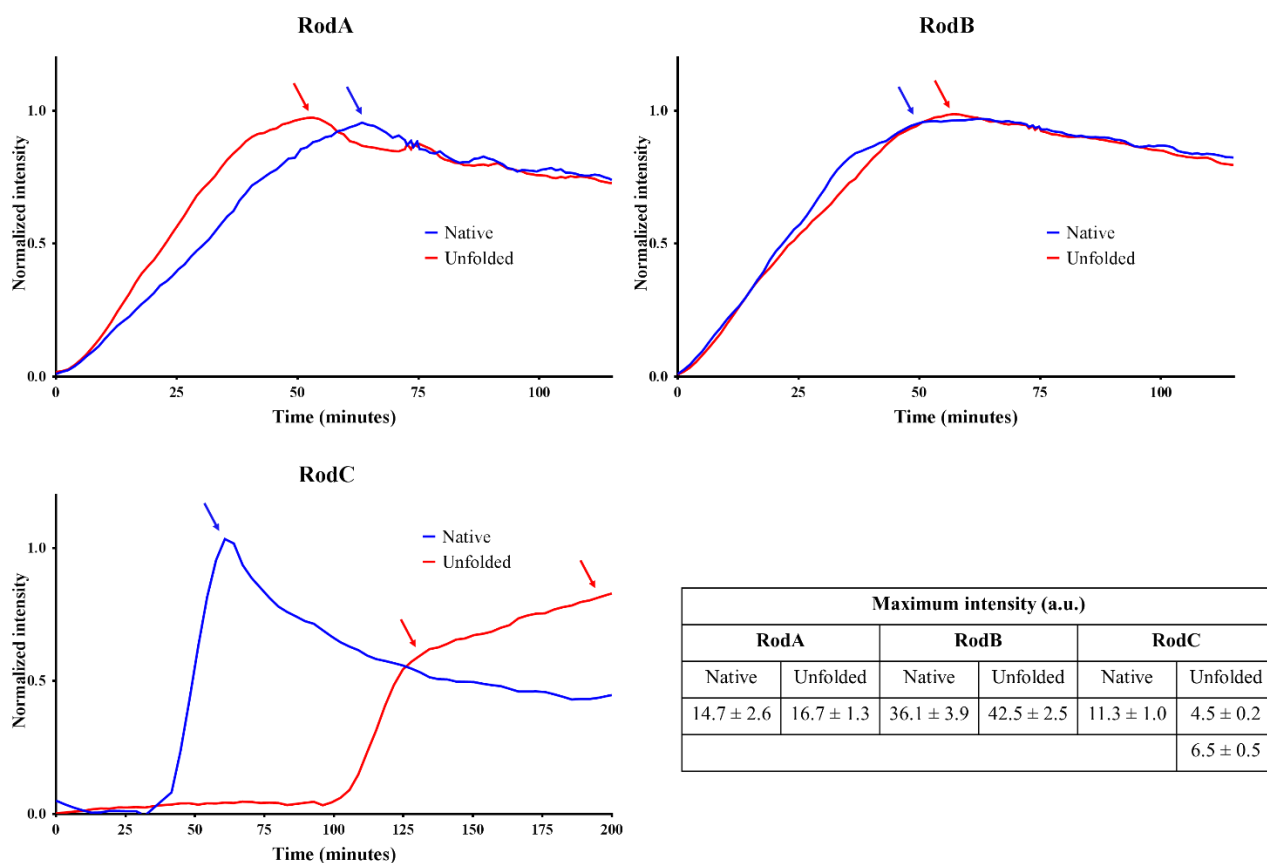


Fig. 42. RodA-C fibrillation kinetics under native and reducing conditions.

The native proteins and proteins under reducing conditions (in the presence of 5 mM DTT) were used at 25 $\mu\text{g}/\text{mL}$. RodA and RodB were studied at 25° C shaking at 480 rpm and RodC at 50 °C with shaking at 720 rpm. The maximum intensities (indicated by arrows in the kinetic traces) are shown in the table. Note that for RodC under reducing conditions, there are two maxima.

The kinetics of RodA and RodB show a very similar profile under reducing and native conditions at 25 $\mu\text{g}/\text{mL}$, with only a somewhat faster growth phase for native RodA (Fig. 42). In the case of RodC both phases become slower under reducing conditions. Moreover, for RodC, the growth phase shows two distinct phases under reducing conditions, indicating a different and more complex behavior of the protein. Indeed, in addition to a very fast phase with effectively the same rate than under native conditions, a second slower growth phase can be observed. While for RodA and RodB, the maxima of fluorescence intensity are effectively the same under native and reducing conditions, the maxima are different in the case of RodC, indicating either a different yield of fibrils, a different binding site for ThT or a mixture of both phenomena.

RESULTS & DISCUSSION

We further investigated the effect of concentration and the presence of an AWI on RodC fiber formation (Fig. 43). At concentrations below 25 μM , the kinetics show a typical sigmoidal profile. Between 25 and 75 $\mu\text{g/mL}$, however, the growth phase shows two distinct components (a fast and a slow one), while at higher concentrations (100 and 150 $\mu\text{g/mL}$, the fast component disappears).

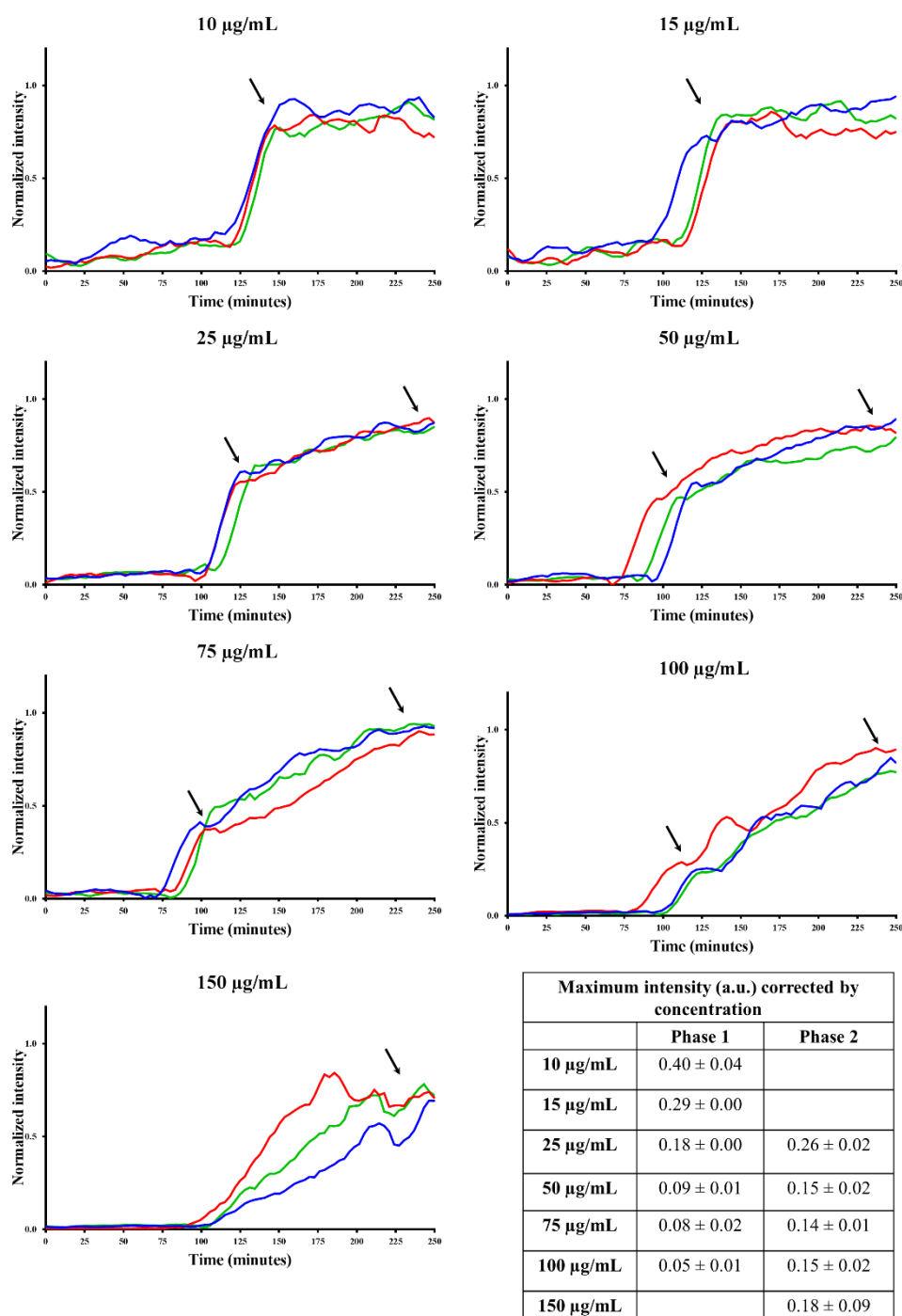


Fig. 43. Concentration dependence of RodC fibrillation kinetics under reducing conditions.

RESULTS & DISCUSSION

Experiments were performed at 50 °C in the presence of 5 mM DTT, with orbital shaking at 720 rpm. Three replicates were recorded for each concentration. The maximum intensities evaluated as shown by the arrows on the kinetic traces are presented in table 3.

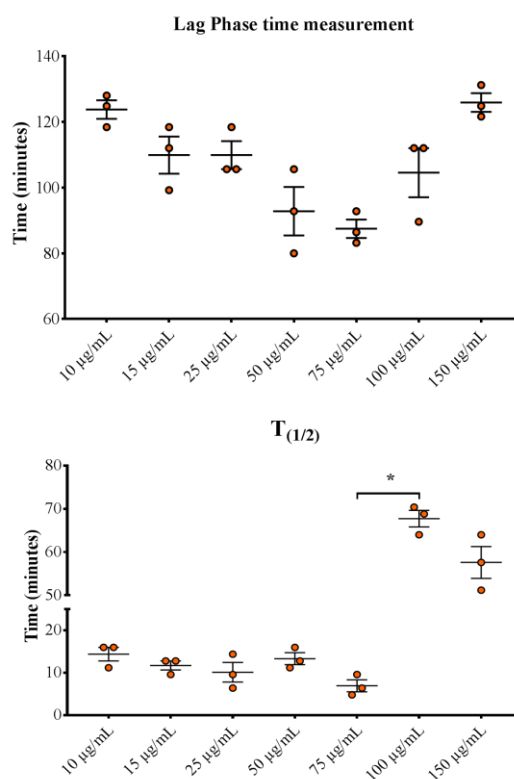


Fig. 44. Concentration dependence of RodC fibrillation under reducing conditions.

Lag-phase and growth-phase $t_{1/2}$ statistical analysis. Data are from Fig. 43 kinetics. Non-parametric Kruskal-Wallis test plus Dunn test for multiple comparisons *post-hoc* (circles=data, means \pm SEM; $n = 3$). The growth phase with increasing concentrations shows two distinct rates. The half-time is shown for the fast component between 10 and 75 μ M and for the single slow component at higher concentrations.

In contrast to the native protein, the lag phase and the fast component of the growth phase of RodC fibrillation kinetics under reducing conditions hardly show any dependence on concentration between 10 and 75 μ M concentrations, although the lag phase tends to decrease with concentration as expected for a high order molecular assembly. As can be observed on the kinetic traces in Fig. 44, the slow component on the growth phase is somewhat concentration independent. Although kinetics did not come to an end at some concentrations, in the presence of a reducing agent the yield of fibers seems to decrease with concentration, most likely due to an accumulation of non-amyloid aggregates. The differences in kinetics and on concentration dependence reveal a different mechanism of fiber formation from the native and unfolded state

RESULTS & DISCUSSION

and suggest that the available AWI area does not limit fiber formation under reducing conditions. This is in agreement with the kinetics observed for the reduced protein with and without an AWI interface. Indeed, as can be observed in Fig. 45, reduced and unfolded RodC is able to form fibers in the absence of an AWI.

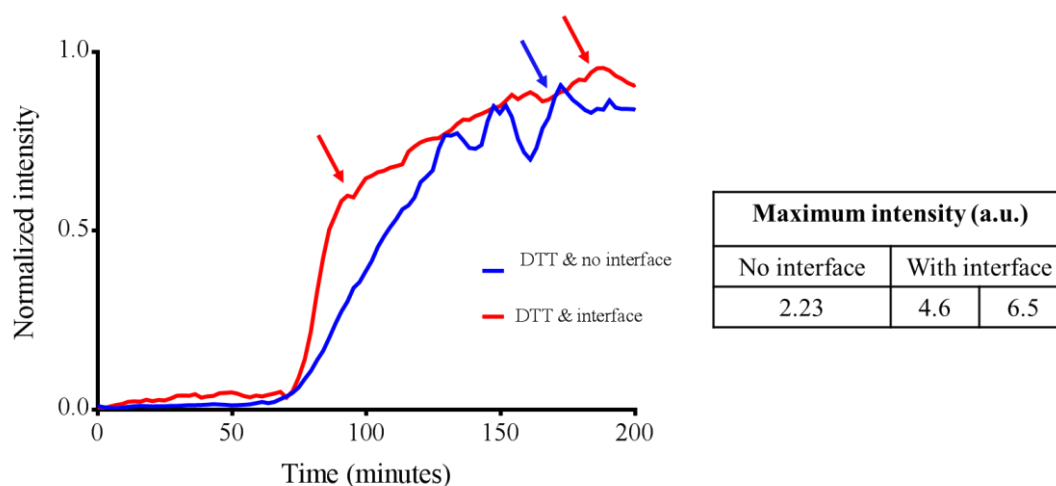


Fig. 45. Comparison of the kinetics of reduced RodC in the presence or absence of an AWI.

Smoothed representative traces. Experiment was performed with standard conditions (25 $\mu\text{g/mL}$ protein, 720 rpm in 20 mM buffer acetate pH 5) in the presence of 5 mM DTT. For the experiment in the absence of an interface the wells were completely filled with the sample (400 μL), while for the experiment with an interface the usual volume was used (100 μL). The maximum intensities corrected to the same volume (100 μL) are shown in the table.

We would like to underline that, under the conditions used, fiber formation was slower or happened at a similar rate for the unfolded proteins than for the native disulfide bridged proteins in clear contrast with the observations described in the literature for SC3 (De Vocht *et al.*, 2000). Although it is difficult to extrapolate the formation of amyloids within the spores to the *in vitro* experiments, the results presented here suggest that disulfides in *A. fumigatus* Class I hydrophobins do not prevent premature amyloid formation as suggested for SC3. Very recent results with RodA indicate that the protein lacking 1 or 4 cysteines, which was known to be absent from the cell wall, is not found either in the cytoplasm of the spores (Vishukumar Aimanianda, Institut Pasteur, personal communication).

3.2.4.4 Important residues in amyloidogenesis probed by single point mutants' kinetics

In order to pinpoint the important residues involved in amyloidogenesis, we followed the same strategy previously described for EAS (Macindoe *et al.*, 2012) and RodA (Valsecchi *et al.*, 2019b). The effect of point mutations on the kinetics of fiber formation was used to probe the importance of a particular residue in amyloidogenesis. We designed 13 point mutations along the RodC sequence [Fig. 46 and table 4 materials and methods], including both, residues predicted to be amyloidogenic and not amyloidogenic. Most of the mutations were done in loop regions as could be inferred from the secondary structure of RodC determined by NMR. Hydrophobic amino acid residues (I, L, V, Y) were mutated to glycines (Fig. 46). The rationale of introducing a glycine, the only amino acid without side-chain constraining the geometry of the backbone, is to increase the conformational space available for the protein in order to difficult the formation of the cross- β structure for residues that are involved in it.

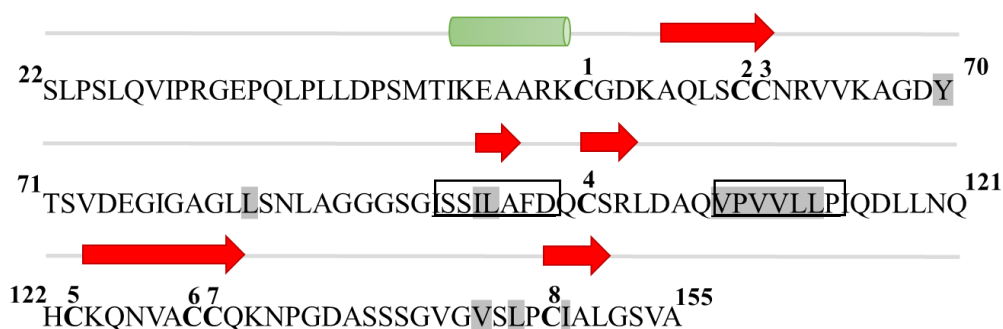
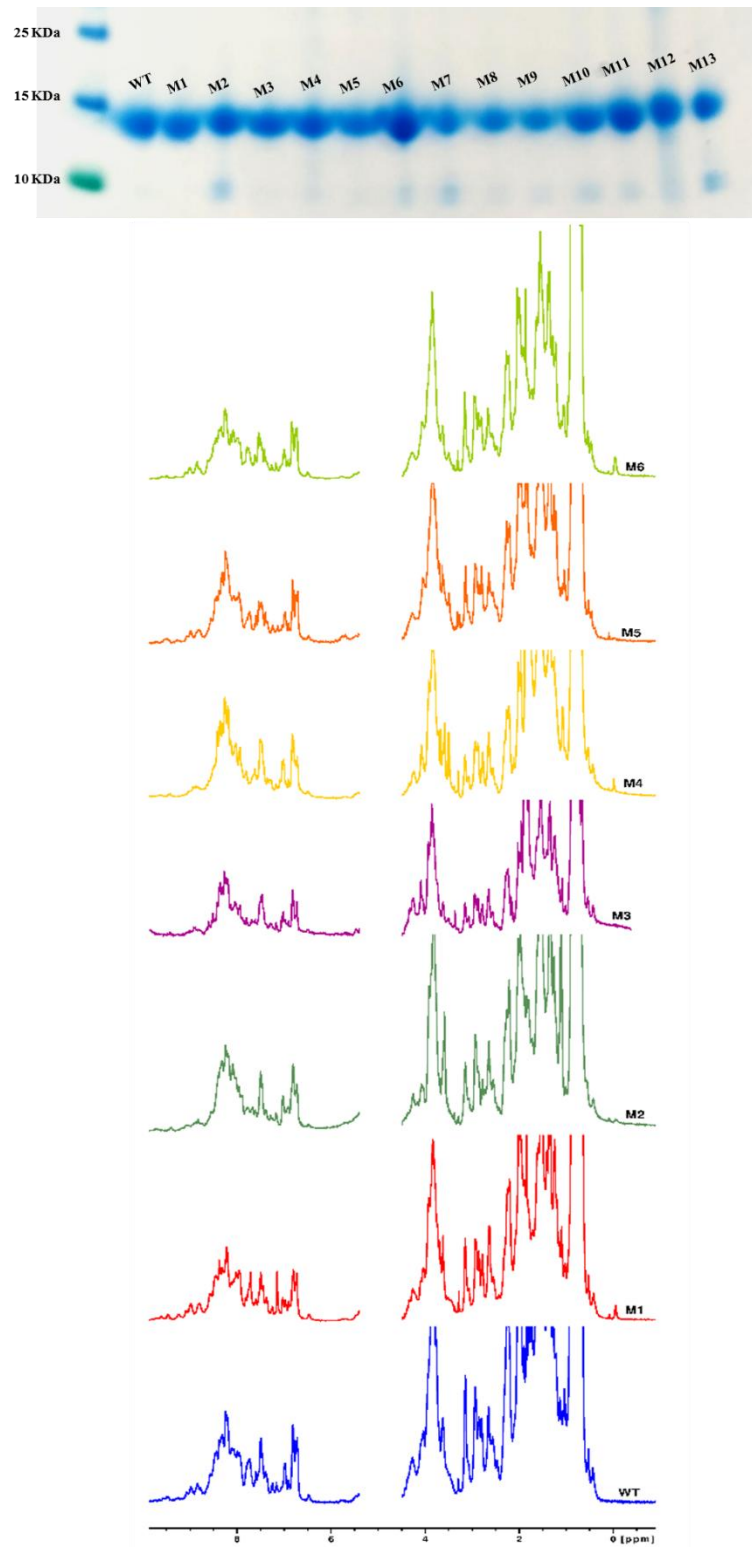


Fig. 46. RodC single-point mutations' position.

Numbering (from 22 to 155) corresponds to the numbering of the full-length RodC precursor (prior to cleavage of the N-terminal secretion region). The mutated residues (X→G) are highlighted in grey, the predicted amyloidogenic regions are boxed. The β -sheets are shown as red arrows and α -helices as green cylinders.

Mutants were purified following the same protocol used for the WT protein. We checked the integrity and identity (molecular weight corresponding to the mutated sequence) by MALDI-ToF/ToF mass spectrometry, the purity by SDS-PAGE (Fig. 47, top) and the folding by 1D-¹H NMR (Fig. 47, bottom).

RESULTS & DISCUSSION



RESULTS & DISCUSSION

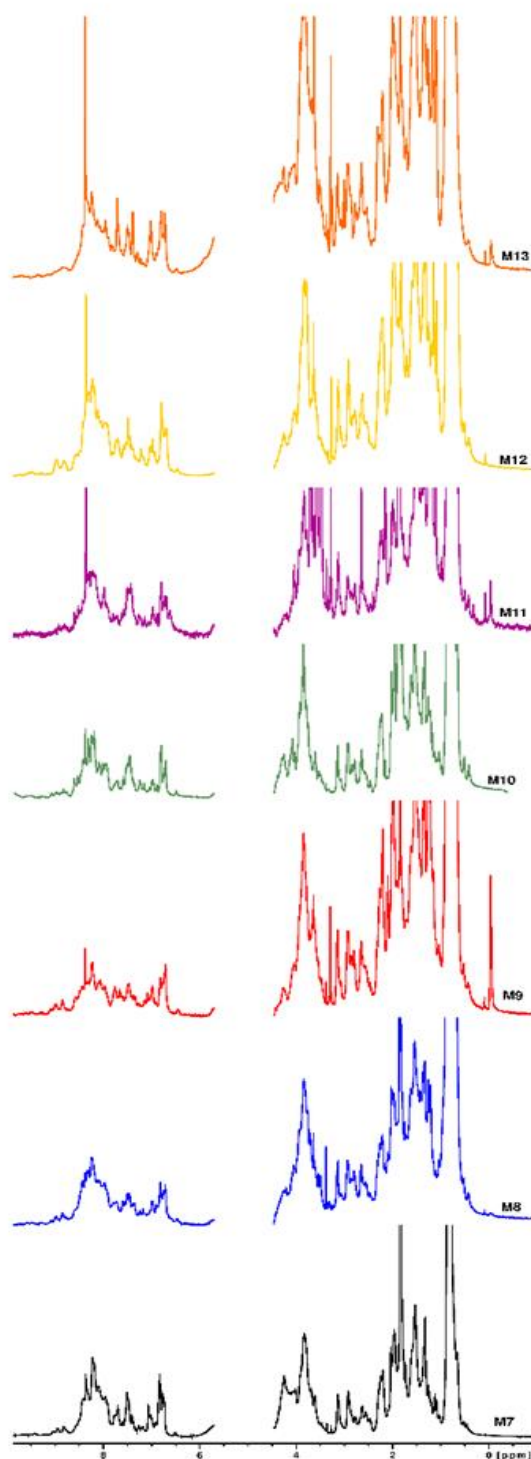


Fig. 47. RodC single-point mutants' purity and foldedness.

Top, SDS-PAGE gel of RodC wildtype (WT) and the 13 mutants (M1-M13). Bottom, downstream (left) and upstream (right) regions of ^1H 1D NMR spectra acquired with 256 scans and a sweep width of 16 ppm at 25°C and 600 MHz. Spectra are referenced relative to DSS

RESULTS & DISCUSSION

(sodium salt of 4,4-dimethyl-4-silapentane-1-sulfonic). Water signal was suppressed with a double pulsed-field gradient stimulated echo and selective adiabatic water inversion.

Importantly, the NMR spectra of all the mutants resemble the spectrum of WT RodC, indicating that the mutation did not affect the structure of the proteins.

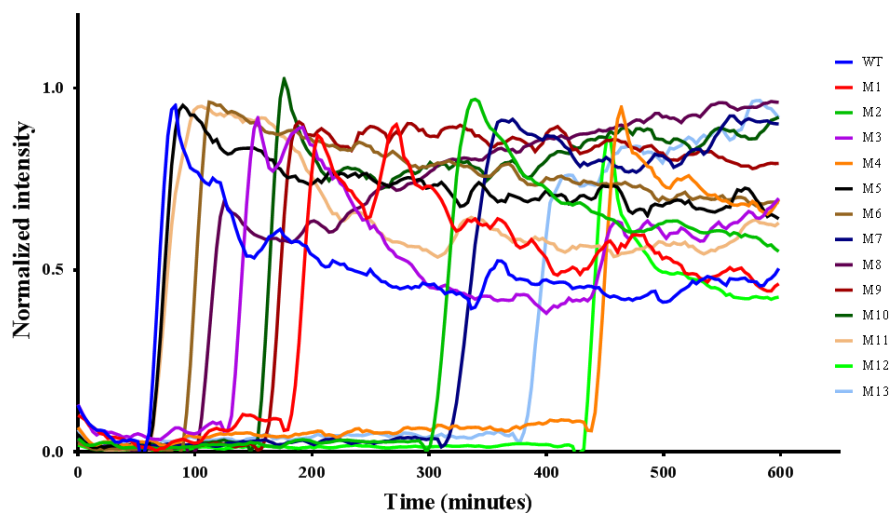
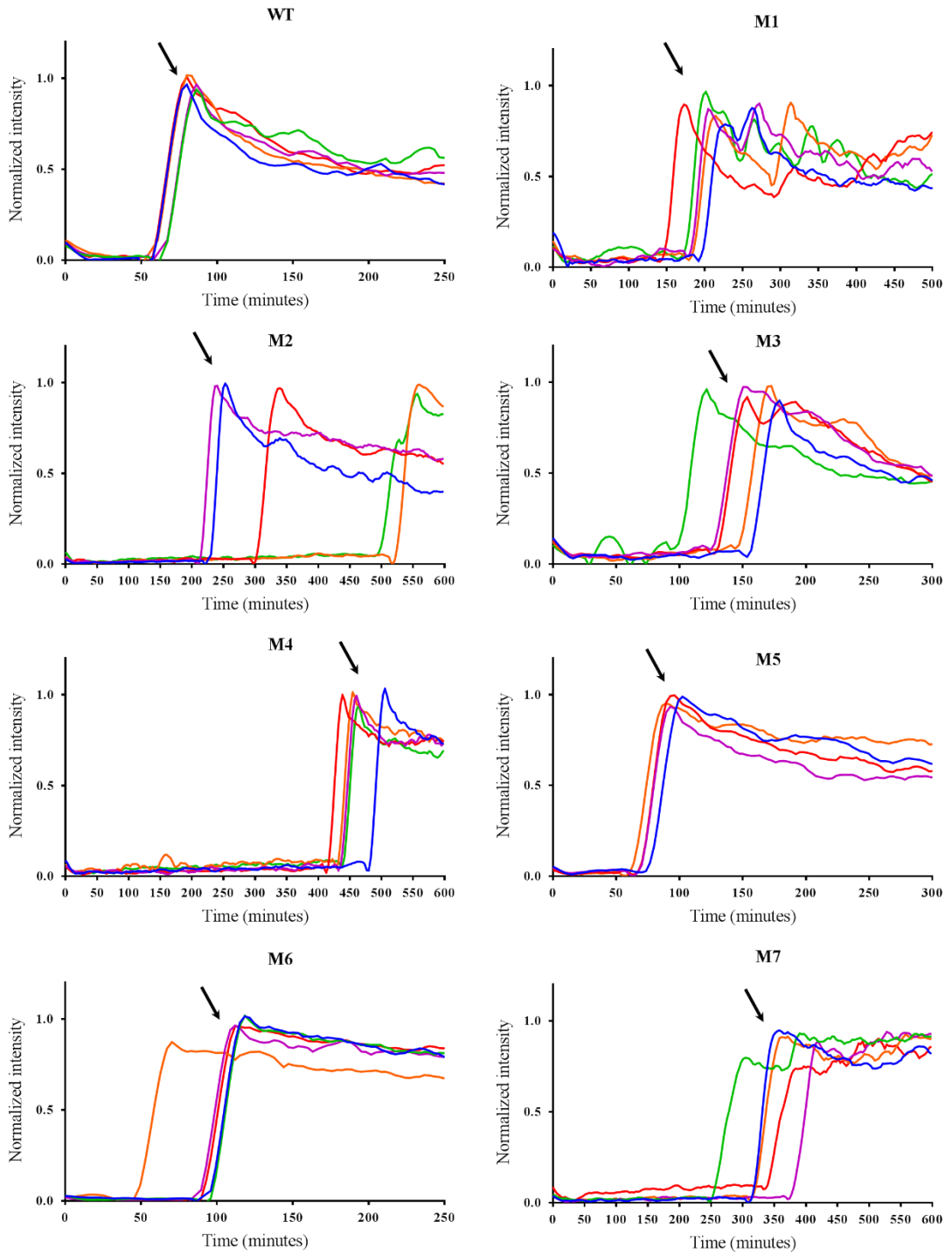


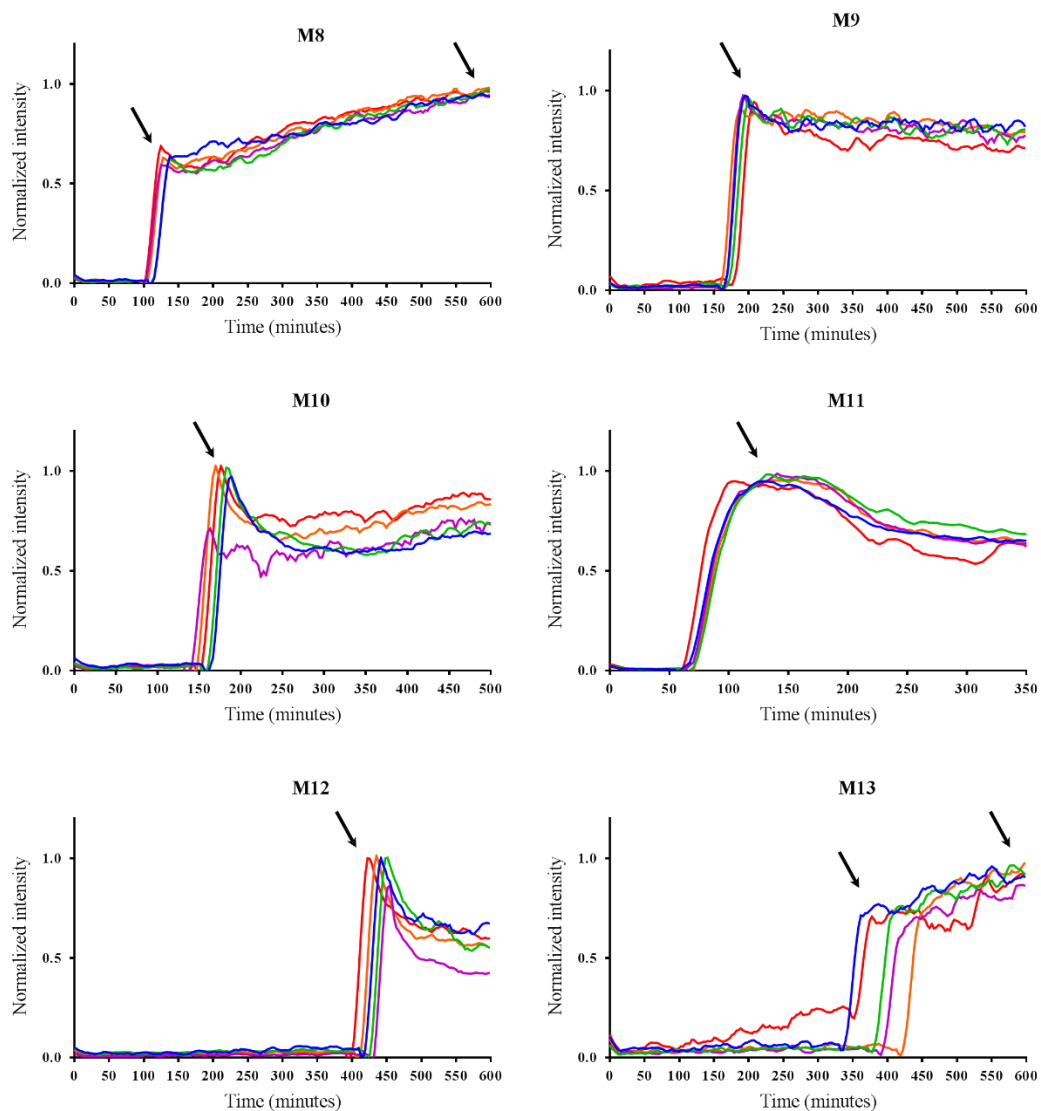
Fig. 48. RodC single-point mutant self-assembly kinetics – Comparison.

Representative traces of the fibrillation kinetics of the WT and mutants followed by ThT fluorescence. Protein concentration was 25 $\mu\text{g}/\text{mL}$ in 50 mM CH_3COONa pH5, 100 μL of sample per well. Five replicates were recorded for each protein (shown in Fig. 49). The experiment was repeated twice to make the statistical analyses displayed in Fig. 50 and with 10 replicates. The WT protein was included in the experiment.

RESULTS & DISCUSSION



RESULTS & DISCUSSION



Maximum intensity (a.u.)		
M1	M2	M3
10.3 ± 1.3	27.3 ± 6.4	8.46 ± 0.4
M4	M5	M6
16.1 ± 2.3	16.0 ± 7.2	38.2 ± 5.1
M7	M8	M9
19.5 ± 4.6	Phase 1: 11.5 ± 0.2	Phase 2: 27.8 ± 3.4
M10	M11	M12
16.9 ± 1.0	37.3 ± 9.8	23.7 ± 5.6
M13		
Phase 1: 10.6 ± 3.0	Phase 2: 11.8 ± 3.0	

Fig. 49. RodC single-point mutant self-assembly kinetics – Individual kinetic traces

RESULTS & DISCUSSION

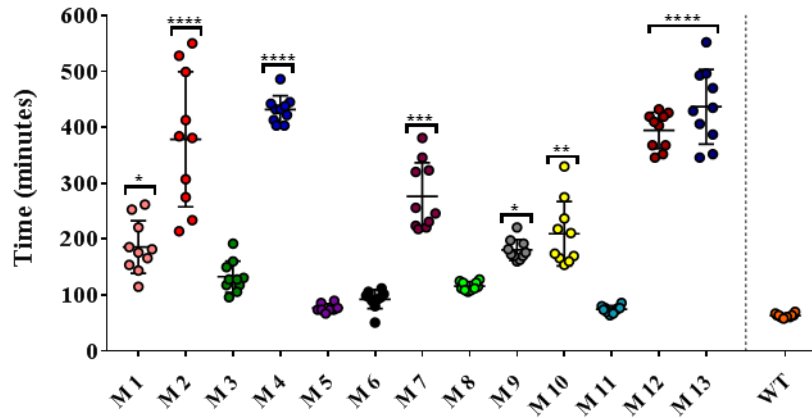


Fig. 50. RodC single-point mutant self-assembly kinetics – Lag phase.

Statistical analysis: non-parametric Kruskal-Wallis test plus Dunn test for post-hoc multiple comparisons (circles=data, mean \pm SEM; n = 10, **** p<0.0001, *** p<0.0001, **p < 0.01, *p < 0.05). The lag-phase duration is shown for 2 experiments with 5 replicates in each experiment. All the mutants and the WT were included in each experiment (same plate) to ensure the same experimental conditions.

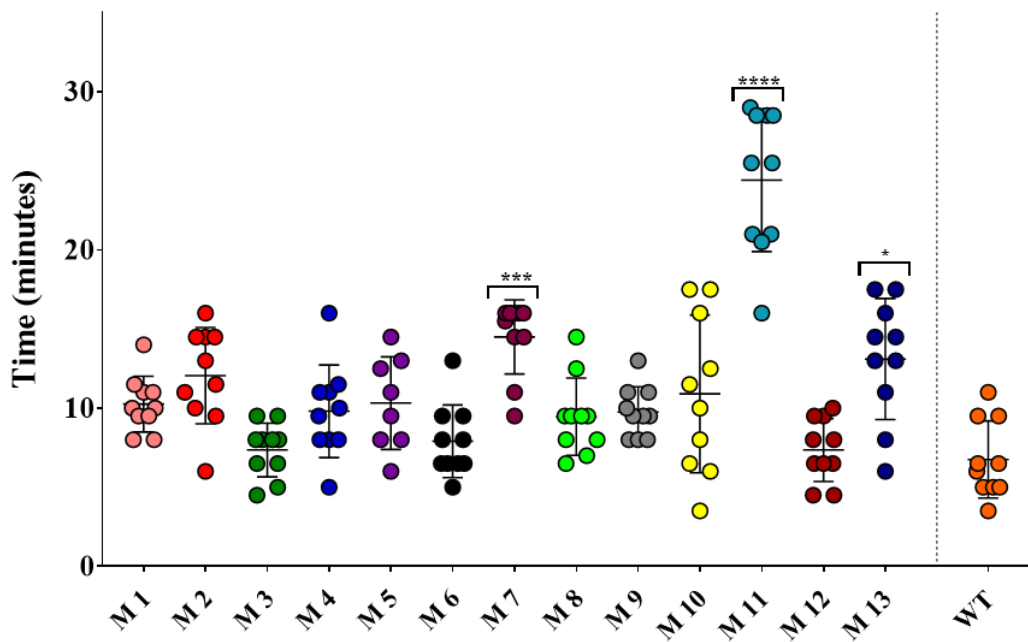


Fig. 51. RodC single-point mutant self-assembly kinetics – Growth phase half-time.

Statistical analysis: non-parametric Kruskal-Wallis test plus *post-hoc* Dunn test for multiple comparisons (circles=data, mean \pm SEM; n = 10, **** p<0.0001, *** p<0.0001, **p < 0.01, *p < 0.05).

RESULTS & DISCUSSION

As shown in figures Fig. 49, Fig. 50 and Fig. 51, most of the mutants show a significantly longer or moderately longer lag-phase compared to the wild-type but hardly any effect on the growth phase, indicating that in general, primary nucleation but not secondary nucleation, elongation or fragmentation are influenced. The only mutants that show a significant effect on the growth-phase relative to the WT (7 ± 2 min) are M11 (24 ± 4 min) and to a lower extent M7 (15 ± 2 min). While for M7 both primary and secondary nucleation /elongation are affected, for M11 only the growth phase (secondary nucleation/elongation) is influenced.

Although some of the mutants show a low variability in the lag-phase between different replicates, many mutants show high variability (M1, M2, M7, M10, M12 and M13). Even though there is not a strict correlation between the lag phase duration and its variability, mutants with a longer lag phase tend to show a highly variable lag phase. This suggests that, like for WT RodC at 40 °C (Fig. 41), primary nucleation is a stochastic phenomenon that implies crossing a high energy barrier. Statistically, mutations M3 (132 ± 27 min), M5 (77 ± 7 min), M6 (93 ± 16 min), M8 (116 ± 7 min) and M11 (74 ± 6 min) have a non-significant or very modest effect on the lag-phase duration relative the wild-type protein (63 ± 3 min). This indicates that these residues are not important for primary nucleation and fiber formation.

In term of their influence on the lag phase, the rest of the mutations can be divided in two groups that show medium-sized ($\sim 200 - 300$ min) or high effects (≤ 380 min) on the lag-phase duration. Mutations M1 (186 ± 44 min), M7 (277 ± 57 min), M9 (181 ± 18 min) and M10 (210 ± 55 min) show a medium sized effect, while mutations M4 (432 ± 23 min), M12 (394 ± 31 min) and M13 (437 ± 63 min) show a very long lag phase over 6-fold that of the WT protein. The M2 mutant (379 ± 115) is a special case with a very long but also very inhomogeneous lag phase (highest standard deviation by far).

Mutants M8, M13, and to a lower extent M10, show more complex kinetics than the rest of the proteins. Indeed, after the fast growth phase, there is another very slow phase. This slow phase does not seem to arise from an autocatalytic phenomenon like secondary nucleation, but could rather be related to the elongation of the fibrils.

The duration of the lag-phase superimposed to the sequence and NMR derived secondary structure of RodC is displayed in Fig. 52. Among the mutations with highest effect, M2 (L82G, C3-C4 loop) and M12 ((L146G, C7-C8 loop) are located in flexible loop regions, while M4 (L96G, β -strand 1) and M13 (I149G, β -strand 5, next to cysteine C8) are located in β -strands of the monomer. Mutations M4 (L96G) and M3 (I95G) were done on 2 neighboring residues

RESULTS & DISCUSSION

of the same β -strand. That mutation M3 does not have an important influence on the fibrillation kinetics, together with the fact that the 1D $^1\text{H-NMR}$ spectra indicate that both mutants have a similar structure to the WT, suggests that the retardation effect induced by mutation M4 is not due to a destabilization of the monomer structure. For mutation M13, we cannot state whether the possible destabilization of the β -sheet plays a role in the observed retardation of fibrillation.

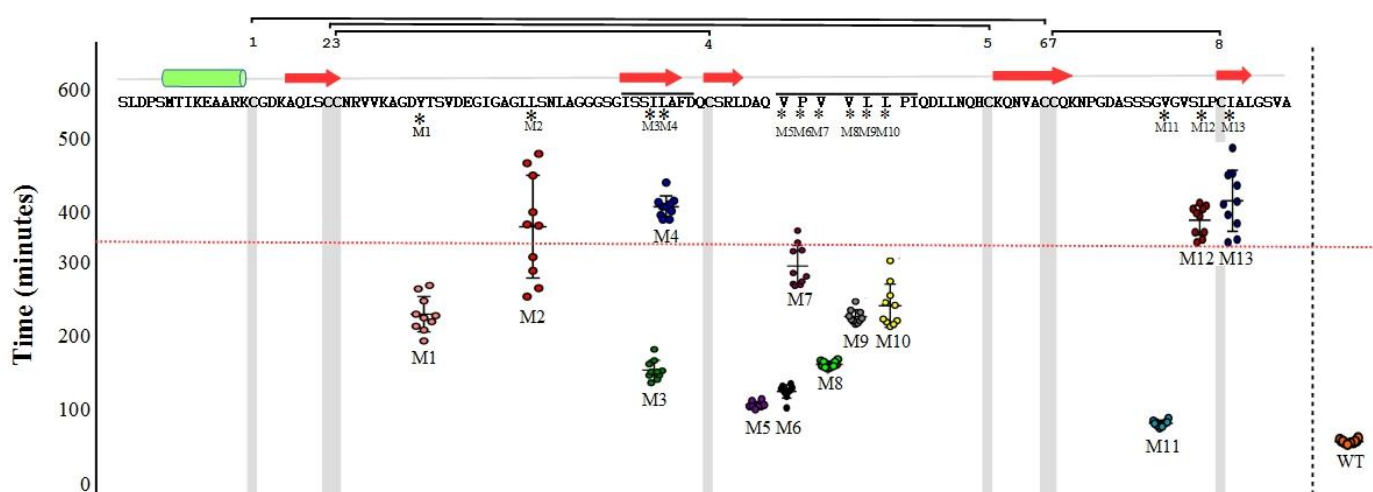


Fig. 52. RodC single-point mutants' kinetics – Lag phase and secondary structure.

The α -helices are shown as green cylinders and the β -strands as red arrows. The cysteine residues are numbered and highlighted in grey and the amyloidogenic regions are indicated with a horizontal dark-grey line. The dashed red line is drawn to best visualize the mutations with a higher effect on the lag phase (M2, M4, M12 and M13). Note that the lag-phase data and the sequence are not strictly aligned. The exact position of the mutation can be observed on the sequence.

3.2.4.5 RodC quadruple mutant kinetics

To further analyze the importance of the residues highlighted by the single point mutational analysis, we designed and characterized a quadruple mutant (QM: I95G-M3, L96G-M4, V144G-M11, L146G-M12) combining two mutations with the highest effect on the lag-phase (M4 and M12) and we designed peptides including these regions to test whether the peptides could form amyloid fibers. Mutations M2 and M13 were not included into the QM mutant due to their high variability (M2) or because of their complex kinetics and proximity of a cysteine (M13) but we synthesized peptides to characterized the corresponding regions. Mutation M3 (I95G), next to M4 and M11 (V144G) were introduced instead. Of note, mutant M11 did not

RESULTS & DISCUSSION

show an effect on the lag phase but had a significantly slower growth phase and higher final fluorescence intensity (which could be related to different ThT binding site).

The folding of the QM mutant was controlled by 2D ^1H - ^{15}N NMR spectra on the ^{15}N labeled protein to better characterize the effect of mutations on the structure of the monomer (Fig. 53).

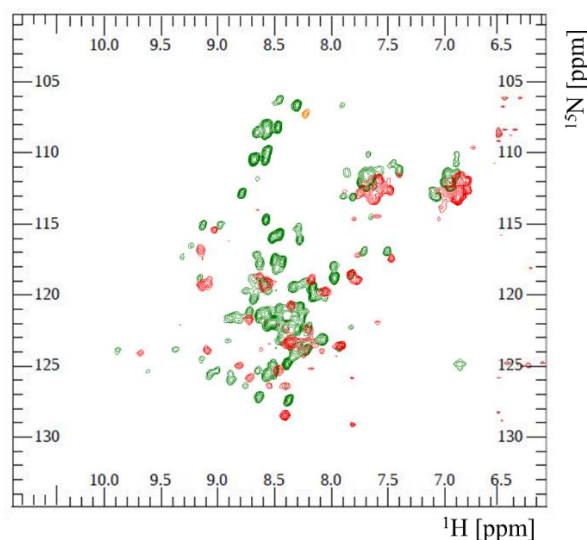


Fig. 53. RodC quadruple point mutants' SOFAST- ^{15}N HMQC experiments.

The spectrum of the mutant (red) was recorded at 25 °C and the spectrum of the WT protein (green) at 45°C. The WT protein spectrum was collected at a higher temperature because at 25 °C, WT RodC gives poor quality spectra with exchange-broadened signals.

Even though the spectra of the QM mutant and WT protein were collected at different temperatures that result in chemical shift differences, and allowing for differences in the spectra due to local perturbations of resonances of amide groups close in space to the mutated positions, the superimposition of the spectra of the mutant and the WT protein clearly indicates that the quadruple point mutant is folded and has retained the native structure of RodC.

The self-assembly kinetics of the QM mutant were performed using the same conditions used for the single-point mutants (fig. 54).

RESULTS & DISCUSSION

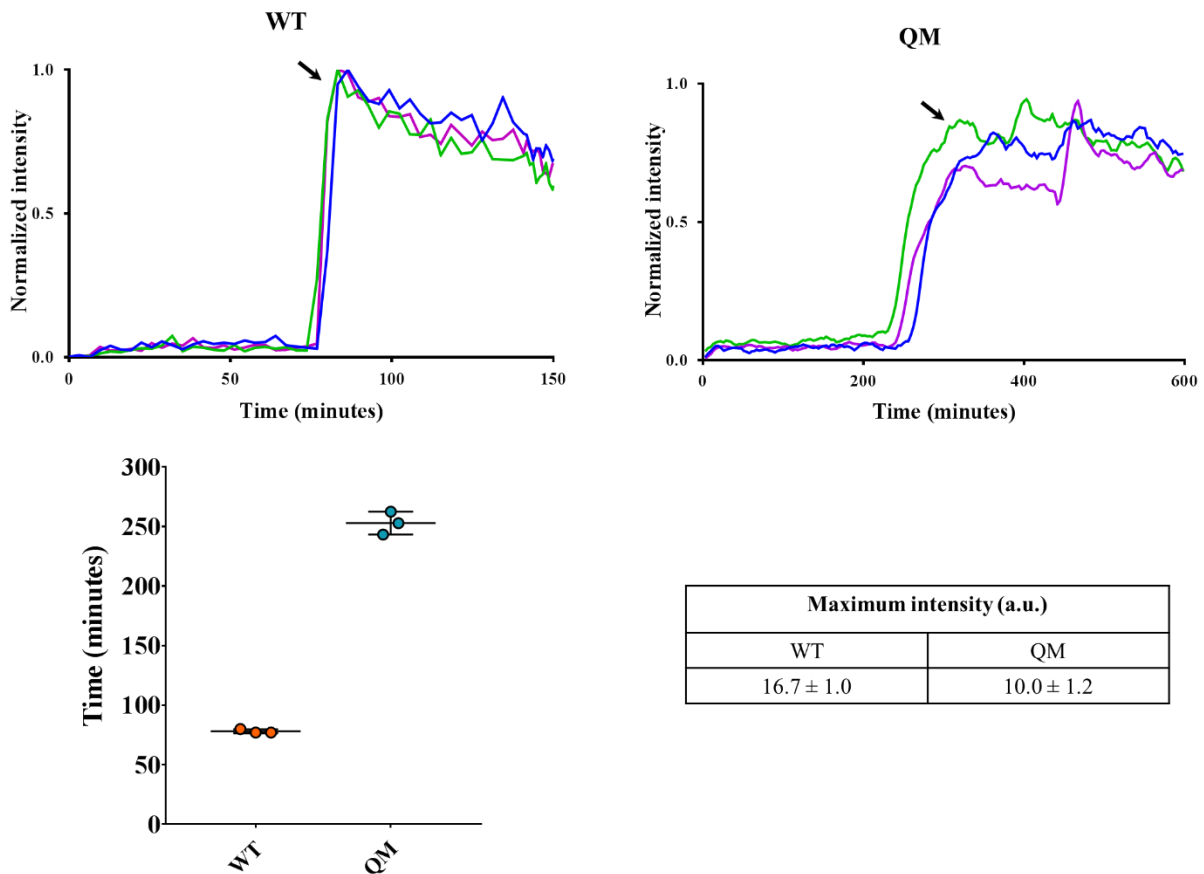


Fig. 54. RodC quadruple-point mutant self-assembly kinetics.

Top, kinetic traces. Bottom, Lag phase time. Statistical analysis: non-parametric Kruskal-Wallis test plus *post-hoc* Dunn test for multiple comparisons (circles=data, means \pm SEM; $n = 3$). Three replicates were recorded for the QM and WT proteins. The maximum fluorescence intensities are indicated in the table.

The quadruple-mutant QM shows a longer lag-phase (253 ± 8 min) than the wild type protein (78 ± 1 min). However, the four mutations do not show an additive effect (see Fig. 50).

3.2.4.6 RodC-derived peptides fibrillation

To further investigate whether the regions highlighted by the effect of mutations on fibrillation kinetics, have an intrinsic capability to form amyloid fibers, we designed 4 different peptides along the sequence. The peptides were synthesized with a formylated N- terminus and an amidated C-terminus to avoid introducing repelling charges upon β -stacking charges in the peptides and to keep as much as possible the resemblance of the ends with those of the peptidic bond.

RESULTS & DISCUSSION

The peptides M2P (⁷⁹AGLLSNLA⁸⁶), M4P (⁹²ISSILAFD⁹⁹), M7P (¹¹⁰VVLLPI¹¹⁵) and M12P (¹⁴⁰SGVGVSLP¹⁴⁷) were studied. The number in the name of the peptide stands for the mutation to which the peptide is related (highlighted in bold). Peptides M4P and M7P correspond to predicted amyloidogenic regions. Peptide M12P corresponds to the C7-C8 region, that has been shown important for fibrillation of RodA and of *N. crassa* EAS protein. While mutation M13 (I149G) showed an important effect on the kinetics and is very close to mutation M12 (L146G), the former residue was not included in the peptide to avoid including a cysteine (C148) in the peptide.

First, we tried kinetic experiments with the peptides at 200 µg/ml in water and 40 µM ThT at 50 °C and vortexing at 720 rpm for 3h. In these conditions, we only saw an increase of fluorescence intensity for the peptide M2P (data not shown).

To see whether the peptides could self-assemble into amyloids, peptides were vortexed as described above and visualized by TEM (Fig. 55) or dried on a mica surface (like RodC and the QM mutant) and analyzed by AFM.

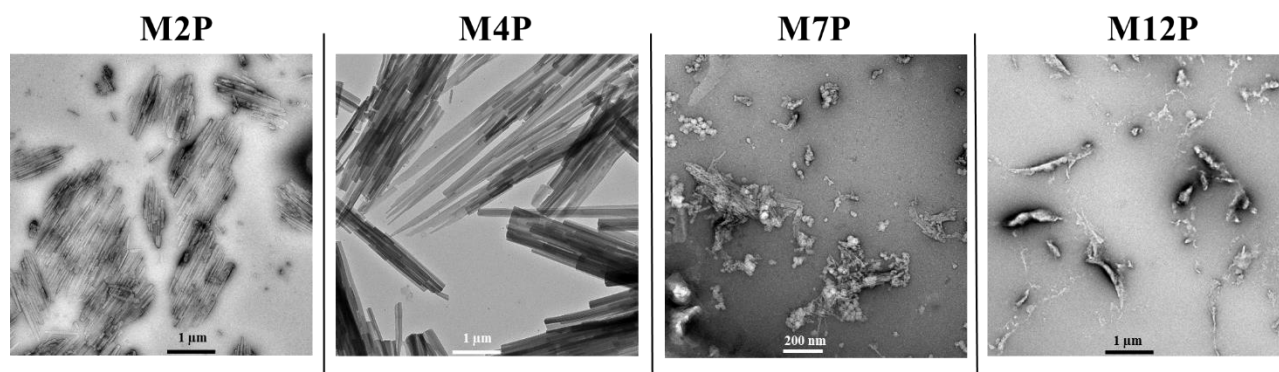


Fig. 55. RodC-derived peptides seen by TEM.

A four-µL droplet of sample (400 µg/mL) was placed on a glow discharged (2 mA, 1 min) carbon coated copper TEM grid and incubated for 2 min at room temperature prior to staining with 2% uranyl acetate.

The M2P and M4P peptides form crystals upon desiccation under TEM conditions. Interestingly, the M4P crystals displayed a diffuse diffraction pattern with two rings at ~5 and ~10 Å. Although it was not possible to accurately measure the reflections, the later are in agreement with the cross-β reflections and suggest that the M4P forms assemblies with an underlying amyloid structure. Peptide M7P formed some long thick fiber assemblies (not

RESULTS & DISCUSSION

shown) and many short disorganized rodlets (≤ 200 nm) (Fig. 55, bottom). Finally, the peptide M12P formed amorphous aggregates only.

Despite trying several conditions, none of the peptides formed rodlets or amyloid fibers (not shown) upon drying on mica, in contrast to the observations made for peptides issued from the amyloidogenic regions highlighted by the mutational analysis in the case of RodA (Valsecchi *et al.*, 2019b; M. Sunde, I. Guijarro, unpublished results). Only amorphous aggregates and domains most likely formed upon drying could be observed for peptides M2P, M4P and M7P.

To summarize the results, in the C5-C6 region, mutagenesis of ¹¹⁰V (M7), ¹¹²L (M9) and ¹¹³L (M10) show an increase of at least three-fold in the lag phase time and the corresponding peptide M7P (¹¹⁰VVLLPI¹¹⁵) is able to form short rodlets as observed by TEM. In the C3-C4 region we probed two different sequences. Mutation of ⁸²L (M2) significantly retards the lag phase and the corresponding peptide M2P (⁷⁹AGLLSNLA⁸⁶) binds ThT. However, no TEM or AFM evidence indicates that the M2P peptide encompassing this region is amyloidogenic. Residue ⁹⁶L, located in strand 2 of the β -barrel also significantly retards the lag phase and the corresponding peptide M4P (⁹²ISSILAFD⁹⁹) forms crystals that can be visualized by TEM and that show a diffraction that corresponds to the cross- β structure, indicating an underlying amyloid structure in the crystals. Finally, mutation of residues ¹⁴⁶L (M12) and ¹⁴⁹I (M13), located close to cysteine C8 (¹⁴⁸C) similarly lengthen the lag phase but the M12P peptide corresponding to the C7-C8 region upstream C8 (¹⁴⁰SGVGVSLP¹⁴⁷) is not amyloidogenic as stated from ThT binding, TEM and AFM. For the later residues, we cannot conclude whether mutations of ¹⁴⁶L/¹⁴⁹I retard primary nucleation because they are involved in the cross- β structure or just because they are important in the rate limiting step of primary nucleation.

The combined results with single point mutants, the quadruple mutant and the peptides, suggest that the region close to ⁹⁶L in the C3-C4 and C4-C5 are important for RodC amyloidogenesis and might be involved in the cross- β spine of the amyloids, while we cannot conclude if the regions in the vicinity of ⁸²L in the C3-C4 region and of cysteine C8 are involved in the cross- β core.

3.2.5 Effects of major fungal cell wall components on RodC self-assembly

To the best of our knowledge, nothing is known about the mechanism of self-assembly of hydrophobins on spores, and only scarce information is available on the components of the cell wall that interact with hydrophobins. For RodA, it has been described in the literature that the

RESULTS & DISCUSSION

protein may interact with melanin and perhaps $\alpha(1,3)$ -glucan (Valsecchi *et al.*, 2018). Some unpublished results in the laboratory have strongly suggested that melanin may be the actual RodA partner on the spores. RodC, like RodA and RodB, is located in the cell wall of *A. fumigatus* conidia. Its presence on the cell wall has been shown by proteomics and with anti-flag-tag antibodies on a mutant of the *rodC* gene coding for a flag-tag (Valsecchi *et al.*, 2018; Valsecchi *et al.*, 2019b). To see if some major cell wall component (CWC) could template the self-assembly of RodC, we performed self-assembly kinetics assays in the presence of the *A. fumigatus* conidia major cell-wall components (CWC), namely, α -(1,3) glucan, β -(1,3) glucan (alkali insoluble fraction), chitin and a synthetic analog of DHN-melanin (insoluble) prepared as described in Materials and Methods (Fig. 56). We also used laminarin, a soluble β -(1,3) glucan with β -(1,6) branches available commercially and, as a negative control, glucose. Experiments were conducted using standard conditions for RodC self-assembly kinetics followed by ThT fluorescence in the presence of increasing amounts of polysaccharides, glucose and synthetic melanin. The concentrations used for all polysaccharides, were 300, 500 and 750 $\mu\text{g/mL}$. For melanin, we used lower concentrations ($\leq 150 \mu\text{g/mL}$) because the high absorbance of this black pigment drastically diminishes the ThT fluorescence above 150 $\mu\text{g/mL}$ concentrations.

RESULTS & DISCUSSION

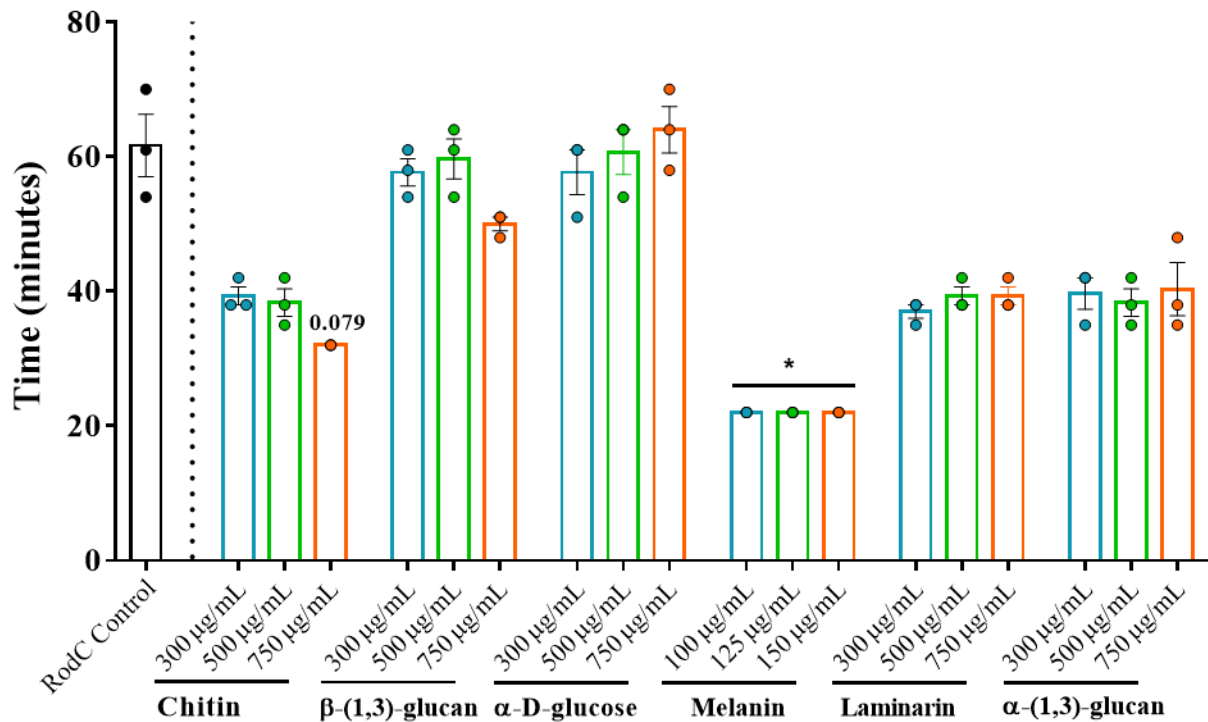


Fig. 56. Effect of different major fungal cell wall components on the lag phase of RodC fibrillation kinetics.

Three replicates were acquired for each condition. RodC data alone is displayed in black. Statistical analysis: non-parametric Kruskal-Wallis test plus *post-hoc* Dunn test for multiple comparisons (circles=data, means \pm SEM; n = 3, *p < 0.05).

A moderate decrease of the lag phase (with no statistically significant difference for $\alpha=0.05$) is observed when RodC self-assembles in the presence of chitin, laminarin or α -(1,3)-glucan. The effect of the later polysaccharides is quite similar, except for chitin at the highest tested concentration (750 $\mu\text{g/mL}$), which displayed a more important effect. A much higher effect is shown by melanin, which accelerates primary nucleation at lower concentrations as indicated by the decrease in the lag phase time. As observed for single point mutants, the growth phase and associated dominating microscopic phenomena (secondary nucleation, elongation) are not influenced by the presence of the compounds.

3.2.5.1 Effect of synthetic melanin on RodC self-assembly

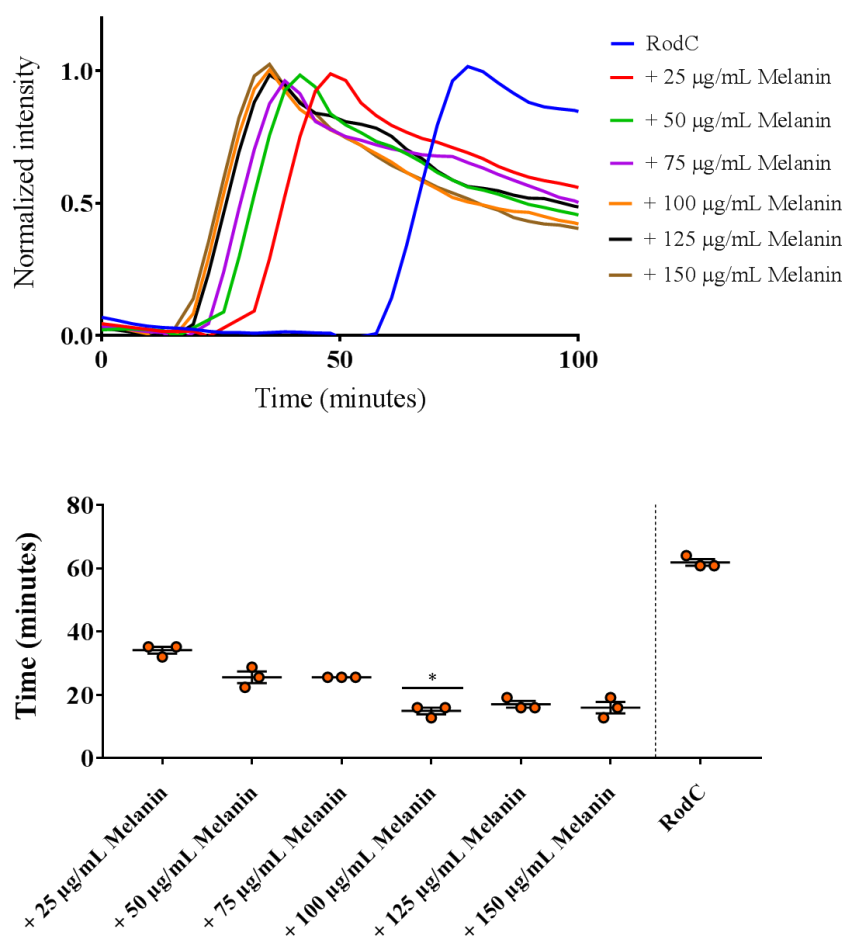


Fig. 57. RodC fibrillation kinetics in the presence of increasing concentrations of melanin.

Top, mean of three kinetic traces; bottom, lag phase time. Statistical analysis: non-parametric Kruskal-Wallis test plus Dunn test for multiple comparisons *post-hoc* (circles=data, mean \pm SEM; $n = 3$, $*p < 0.05$).

At the melanin concentrations initially tested, the effect of melanin was concentration independent. To check if the effect of melanin is concentration-dependent at lower concentrations, we performed the experiment with synthetic melanin at concentrations ranging from 25 to 150 $\mu\text{g/mL}$ (Fig. 57). The kinetic traces and the associated lag-phase times clearly indicate that the effect of melanin increases with concentration and saturates at 100 $\mu\text{g/mL}$. Hence, synthetic melanin favors primary nucleation of RodC, a phenomenon that could be important for RodC amyloidogenesis on the spores.

Conclusion & Perspectives

4 Conclusions & perspectives

4.1 Conclusions

We have shown that the three hydrophobins RodA-C from *A. fumigatus* self-assemble into true amyloids and require an HHI/AWI, like the hydrophobins EAS, DewA and MPG1 from other fungi. Analysis of the chemical shifts of RodB, RodC and its close homolog RodA, coupled to the analysis of the secondary structure topology and the nOe patterns, have indicated that RodB and RodC show the typical fold of hydrophobins with a rigid β -barrel (or half β -barrel) core highly constricted by disulfide bonds surrounded by different secondary structures and disordered inter-cysteine loop regions.

Thermal transitions in the presence of different surfaces (silicon or quartz) and an air-water interface resulted in different conformational changes and assembly for the 6 hydrophobins, indicating that the nature of the surface is important in determining the auto-association process and the nature of the assemblies formed. This could also be observed in other instances: (i) SRCD spectra of monomeric RodB at 25 °C in calcium fluoride and quartz cells were different (not shown) and suggest that RodB monomers readily interact with CaF₂; (ii) rodlets formed by RodA and RodB are better ordered and form layers on the hydrophobic surface HOPG relative to hydrophilic mica, while RodC does not self-assemble on HOPG but forms fibers and rodlets upon drying on mica. The surface activity of these proteins may reflect their different biological role and the conditions upon which they self-assemble.

RodA-C amyloidogenesis kinetics *in vitro* show a counterintuitive dependence on concentration for a high order intermolecular assembly process: an increase in concentration increases the lag phase and the growth-phase times. Analysis of the concentration dependence of the rates and of the availability of the AWI indicates that surface saturation is at the origin of this auto-inhibition. The relative magnitude of the effect of concentration on the lag-phase and growth phase suggests that surface saturation has a higher influence on primary nucleation than on secondary nucleation, elongation and perhaps, lateral association of the rodlets. An auto-inhibition effect has also been reported for DewA (Morris, Kwan and Sunde, 2013). In the case of DewA, however, the inhibition mechanism is different. In solution, DewA populates two distinct assembly-competent conformers with the same disulfide pattern. One of the conformers forms an off-pathway dimer at high concentrations, thus lowering the rate of fiber

formation. As observed here for RodA-C, it has been shown for MPG1, a hydrophobin that also requires an AWI for self-assembly, that surface saturation is also implicated in defining the kinetics of rodlet formation at the air-solution interface but does not lead to auto-inhibition (Pham *et al.*, 2016). MPG1 shows atypical kinetics with a very fast lag phase (not visible) in which assembly-competent nuclei are formed very quickly and a growth phase rate that is monomer concentration independent. This concentration independence can be explained by surface saturation limiting the maximal number of growth-competent fibrils that is reached very quickly after the start of the reaction.

In contrast to MPG1, RodA-C show a visible lag phase and a very fast growth phase dominated by an autocatalytic process in which secondary nucleation must play an important role. The lag phase time for RodC is much longer than for RodA and RodB and needs higher temperatures due to a high transition barrier necessary to form detectable nuclei. The lag phase duration of RodC is also more variable, becomes more variable at lower temperatures and there is a correlation between the duration of the lag phase and its duration for the single point mutants of RodC studied here. This variability reveals a highly stochastic process for primary nucleation of RodC which might be related to the heterogeneity of its self-assemblies that we observed on AFM (Fig. 29), FTIR of different rodlet preparations (Fig. 6 of the manuscript) or ssNMR spectra (Fig. 35). Interestingly, synthetic melanin, an analog of DHN melanin present at the surface of the spores, favors primary nucleation and may possibly template rodlet formation. It will be interesting to observe the self-assemblies on AFM plaques coated with melanin.

Despite many studies on the mechanism of amyloidogenesis of hydrophobins, the information on the amyloidogenic determinants and the residues implicated is scarce. The point-mutational analysis of RodC and the characterization of the peptides suggest that the residues in the β -sheet close to cysteine C4 and in the disordered C4-C5 region are important for RodC amyloidogenesis and might be involved in the cross- β spine of the fibers. This study also shows that other residues in the C3-C4 region and close to cysteine C8 are important for fiber formation but the results do not allow us to state whether these residues could be implicated in the cross- β core. For RodA, the mutational analysis indicated that residues in the C7-C8 and C4-C5 disordered regions are implicated in the cross- β spine of the rodlets (Valsecchi *et al.*, 2019b; I. Guijarro personal communication). The mutational analysis of RodB has not yet been performed, but a peptide corresponding to the C7-C8 spontaneously self-assembles (M. Sunde, unpublished) into amyloid fibers that can be visualized by TEM.

Despite the high sequence similarity of RodA-C, these proteins show different amyloidogenic predicted regions and the amyloidogenic determinants revealed experimentally for RodA and RodC differ. In the case of EAS, the same mutational strategy highlighted the importance of the hydrophobic C7-C8 region and showed that the replacement of the amyloidogenic region by the sequence of the Class II NC2 hydrophobin that does not form fibers, completely prevented fibrillation of the protein (Macindoe *et al.*, 2012). Furthermore, hydrogen-deuterium exchange experiments on SC3 highlighted the role of the C3-C4 region for adhesion to hydrophobic surfaces and suggested its implication on rodlet formation (Wang *et al.*, 2004) but no information is available on other regions of the protein. The few studied cases suggest that the amyloidogenic determinants of each hydrophobin might be specific and that the size and the structure of the cross- β core can be different but highlight the importance of exposed hydrophobic residues in disordered regions of the monomeric proteins. In this respect, it is interesting to note that the monomer to rodlet transition observed by ATR-FTIR for the six hydrophobins shows a shift from disordered (1640 cm^{-1}) to straight intramolecular β -sheets ($\leq 1630\text{ cm}^{-1}$) typical of the cross- β structure. This is in agreement with the mutational analysis of RodA, RodC and EAS that suggests that this methodology is helpful to detect residues involved in the cross- β core of the amyloids. The sequential assignment of RodA rodlets' resonances in ssNMR spectra is underway, but preliminary analysis of the secondary chemical shifts demonstrates that the residues in the C7-C8 and C4-C5 regions put forward by mutagenesis are indeed involved in β -sheets in the rodlet state.

4.2 Perspectives

Several data are needed to complete the comparative analysis of RodA-C and the importance of major cell wall components on their self-assembly. First, it would be interesting to obtain the structures of the monomeric forms of RodB and RodC. While for RodB this should not pose a problem (I. Guijarro, personal communication), the chemical exchange phenomenon observed for RodC renders signal assignment and hence structure calculations very difficult. Nevertheless, it should be possible to calculate its structure from the ^{15}N and ^{13}C edited NOE data that I collected using the ARIA software helped with manual assignments. Second, the dependence of fibrillation kinetics on concentration and temperature of RodA and RodB should be completed. Third, as done for RodC, the effect of major cell wall components on the kinetics of self-assembly of RodA and RodB should be performed and fourth, the assembly of the three hydrophobins on surfaces covered by major cell wall components should be studied by AFM.

The latter has already been done for RodA (I. Valsecchi, V. Duprès, F. Lafont, V. Aimanianda and I. Guijarro), with very interesting results that indicate that melanin is the partner of RodA on the fungal cell wall.

Our results, together with future high-resolution studies, e.g. cryo-EM/ssNMR, of the assembled rodlets should shed light on the roles they play in fungal biology and may lead to the use of these hydrophobins in biotechnological applications. In collaboration with A. Loquet and his team, the laboratory is currently focusing on RodA and will also work on RodB by ssNMR.

Bibliography

5 Bibliography

1. Aimanianda, V. *et al.* (2009) “Surface hydrophobin prevents immune recognition of airborne fungal spores,” *Nature*, 460(7259), pp. 1117–1121. doi: 10.1038/nature08264.
2. Arosio, P., Knowles, T. P. J. and Linse, S. (2015) “On the lag phase in amyloid fibril formation,” *Physical Chemistry Chemical Physics*. The Royal Society of Chemistry, 17(12), pp. 7606–7618. doi: 10.1039/c4cp05563b.
3. Baker, M. J. *et al.* (2014) “Using Fourier transform IR spectroscopy to analyze biological materials,” *Nature Protocols*. NIH Public Access, 9(8), pp. 1771–1791. doi: 10.1038/nprot.2014.110.
4. Baldwin, A. J. *et al.* (2011) “Metastability of native proteins and the phenomenon of amyloid formation,” *Journal of the American Chemical Society*. American Chemical Society, 133(36), pp. 14160–14163. doi: 10.1021/ja2017703.
5. Bayry, J. *et al.* (2012) “Hydrophobins--unique fungal proteins.,” *PLoS pathogens*. Public Library of Science, 8(5), p. e1002700. doi: 10.1371/journal.ppat.1002700.
6. Bayry, J. *et al.* (2014) “Surface structure characterization of *Aspergillus fumigatus* conidia mutated in the melanin synthesis pathway and their human cellular immune response,” *Infection and Immunity*, 82(8), pp. 3141–3153. doi: 10.1128/IAI.01726-14.
7. Berger, B. W. and Sallada, N. D. (2019) “Hydrophobins: Multifunctional biosurfactants for interface engineering,” *Journal of Biological Engineering*. BioMed Central, 13(1), p. 10. doi: 10.1186/s13036-018-0136-1.
8. Berjanskii, M. V. and Wishart, D. S. (2005) “A simple method to predict protein flexibility using secondary chemical shifts,” *Journal of the American Chemical Society*. American Chemical Society, 127(43), pp. 14970–14971. doi: 10.1021/ja054842f.
9. Biancalana, M. and Koide, S. (2010) “Molecular mechanism of Thioflavin-T binding to

BIBLIOGRAPHY

- amyloid fibrils.,” *Biochimica et biophysica acta*. NIH Public Access, 1804(7), pp. 1405–12.
doi: 10.1016/j.bbapap.2010.04.001.
10. Boeuf, S. *et al.* (2012) “Engineering hydrophobin DewA to generate surfaces that enhance adhesion of human but not bacterial cells,” *Acta Biomaterialia*. Elsevier, 8(3), pp. 1037–1047.
doi: 10.1016/j.actbio.2011.11.022.
11. Bongomin, F. *et al.* (2017) “Global and multi-national prevalence of fungal diseases—estimate precision,” *Journal of Fungi*. Multidisciplinary Digital Publishing Institute, p. 57.
doi: 10.3390/jof3040057.
12. Brown, G. D. *et al.* (2012) “Hidden killers: Human fungal infections,” *Science Translational Medicine*. American Association for the Advancement of Science, 4(165rv13), p. 165rv13.
doi: 10.1126/scitranslmed.3004404.
13. Brown, T. (2006) “Organizing for the future: Labour’s renewal strategies, popular education and radical history,” *Studies in Continuing Education*. Nature Publishing Group, 28(1), pp. 33–48. doi: 10.1038/nri1745.
14. Buell, A. K. *et al.* (2012) “Detailed analysis of the energy barriers for amyloid fibril growth,” *Angewandte Chemie - International Edition*. John Wiley & Sons, Ltd, 51(21), pp. 5247–5251.
doi: 10.1002/anie.201108040.
15. Buell, A. K. *et al.* (2014) “Solution conditions determine the relative importance of nucleation and growth processes in α -synuclein aggregation,” *Proceedings of the National Academy of Sciences of the United States of America*. National Academy of Sciences, 111(21), pp. 7671–7676. doi: 10.1073/pnas.1315346111.
16. Cadena, J., Thompson, G. R. and Patterson, T. F. (2016) “Invasive Aspergillosis: Current Strategies for Diagnosis and Management,” *Infectious Disease Clinics of North America*. Elsevier, pp. 125–142. doi: 10.1016/j.idc.2015.10.015.
17. Carrion, S. d. J. *et al.* (2013) “The RodA Hydrophobin on *Aspergillus fumigatus* Spores Masks

BIBLIOGRAPHY

- Dectin-1- and Dectin-2-Dependent Responses and Enhances Fungal Survival In Vivo,” *The Journal of Immunology*, 191(5), pp. 2581–2588. doi: 10.4049/jimmunol.1300748.
18. Chiti & Dobson (2017) “Amyloid Formation, Protein Homeostasis, and Human Disease: A Summary of Progress Over the Last Decade,” *Annual Review of Biochemistry*. pp. 1–42. doi: 10.1146/annurev-biochem-061516-045115.
19. Chiti, F. *et al.* (1999) “Designing conditions for in vitro formation of amyloid protofilaments and fibrils,” *Proceedings of the National Academy of Sciences of the United States of America*. National Academy of Sciences, 96(7), pp. 3590–3594. doi: 10.1073/pnas.96.7.3590.
20. Chiti, F. and Dobson, C. M. (2006) “Protein Misfolding, Functional Amyloid, and Human Disease,” *Annual Review of Biochemistry*. Annual Reviews, 75(1), pp. 333–366. doi: 10.1146/annurev.biochem.75.101304.123901.
21. Cohen, S. I. A. *et al.* (2013) “Proliferation of amyloid- β 42 aggregates occurs through a secondary nucleation mechanism,” *Proceedings of the National Academy of Sciences of the United States of America*, 110(24), pp. 9758–9763. doi: 10.1073/pnas.1218402110.
22. Croft, C. A. *et al.* (2016) “Interactions of *Aspergillus fumigatus* conidia with airway epithelial cells: A critical review,” *Frontiers in Microbiology*. Frontiers, p. 472. doi: 10.3389/fmicb.2016.00472.
23. Dean, R. *et al.* (2012) “The Top 10 fungal pathogens in molecular plant pathology.” *Molecular plant pathology*. John Wiley & Sons, Ltd (10.1111), 13(4), pp. 414–30. doi: 10.1111/j.1364-3703.2011.00783.x.
24. Delaglio, F. *et al.* (1995) “NMRPipe: A multidimensional spectral processing system based on UNIX pipes,” *Journal of Biomolecular NMR*. ESCOM Science Publishers B.V., Leiden/Kluwer Academic Publishers, 6(3), pp. 277–293. doi: 10.1007/BF00197809.
25. Dempsey, G. P. and Beever, R. E. (1979) “Electron microscopy of the rodlet layer of *Neurospora crassa* conidia,” *Journal of Bacteriology*. American Society for Microbiology

BIBLIOGRAPHY

- (ASM), 140(3), pp. 1050–1062. Available at: <http://www.ncbi.nlm.nih.gov/pubmed/93107>
(Accessed: October 8, 2019).
26. Dobson, C. M. (1999) “Protein misfolding, evolution and disease,” *Trends in Biochemical Sciences*. Elsevier Current Trends, pp. 329–332. doi: 10.1016/S0968-0004(99)01445-0.
27. Dobson, C. M. (2017) *The amyloid phenomenon and its links with human disease*, Cold Spring Harbor Perspectives in Biology. Cold Spring Harbor Laboratory Press. doi: 10.1101/cshperspect.a023648.
28. Dufrêne, Y. F. (2008) “Towards nanomicrobiology using atomic force microscopy.,” *Nature Reviews Microbiology*, 6(9), pp. 674–680. doi: 10.1038/nrmicro1948.
29. Eanes, E. D. and Glenner, G. G. (1968) “X-ray diffraction studies on amyloid filaments.,” *The journal of histochemistry and cytochemistry: official journal of the Histochemistry Society*. SAGE Publications Sage UK: London, England, 16(11), pp. 673–677. doi: 10.1177/16.11.673.
30. Eisenberg, D. and Jucker, M. (2012) “The amyloid state of proteins in human diseases,” *Cell*. Cell Press, pp. 1188–1203. doi: 10.1016/j.cell.2012.02.022.
31. Eisenman, H. C. and Casadevall, A. (2012) “Synthesis and assembly of fungal melanin,” *Applied Microbiology and Biotechnology*. NIH Public Access, pp. 931–940. doi: 10.1007/s00253-011-3777-2.
32. Fausto, A., Rodrigues, M. L. and Coelho, C. (2019) “The still underestimated problem of fungal diseases worldwide,” *Frontiers in Microbiology*. Frontiers Media SA, p. 214. doi: 10.3389/fmicb.2019.00214.
33. Fitzpatrick, A. W. P. *et al.* (2013) “Atomic structure and hierarchical assembly of a cross-amyloid fibril,” *Proceedings of the National Academy of Sciences*. National Academy of Sciences, 110(14), pp. 5468–5473. doi: 10.1073/pnas.1219476110.
34. Fitzpatrick, A. W. and Saibil, H. R. (2019) *Cryo-EM of amyloid fibrils and cellular aggregates*, *Current Opinion in Structural Biology*. Elsevier Current Trends. doi:

BIBLIOGRAPHY

- 10.1016/j.sbi.2019.05.003.
35. Fontaine, T. (2017) *Sphingolipids from the human fungal pathogen Aspergillus fumigatus*, *Biochimie*. Elsevier. doi: 10.1016/j.biochi.2017.06.012.
36. Fowler, D. M. *et al.* (2005) “Functional Amyloid Formation within Mammalian Tissue,” *PLoS Biology*. Edited by J. Weissman. Public Library of Science, 4(1), p. e6. doi: 10.1371/journal.pbio.0040006.
37. Friedreich, N. and Kekulé, A. (1859) “Zur Amyloidfrage,” *Archiv für Pathologische Anatomie und Physiologie und für Klinische Medicin*. Springer-Verlag, 16(1–2), pp. 50–65. doi: 10.1007/BF01945246.
38. Gade Malmos, K. *et al.* (2017) “ThT 101: a primer on the use of thioflavin T to investigate amyloid formation,” *Amyloid*, 24(1), pp. 1–16. doi: 10.1080/13506129.2017.1304905.
39. Gaynes, R. (2017) “The discovery of penicillin—new insights after more than 75 years of clinical use,” *Emerging Infectious Diseases*, 23(5), pp. 849–853. doi: 10.3201/eid2305.161556.
40. Gazit, E. (2002) “A possible role for π -stacking in the self-assembly of amyloid fibrils,” *FASEB Journal*. Federation of American Societies for Experimental Biology, pp. 77–83. doi: 10.1096/fj.01-0442hyp.
41. Gow, N. A. R., Latgé, J.-P. and Munro, C. A. (2017) “The Fungal Cell Wall: Structure, Biosynthesis, and Function,” *Microbiology Spectrum*. asm Pub2Web, 5(3). doi: 10.1128/microbiolspec.funk-0035-2016.
42. Gras, S. L., Waddington, L. J. and Goldie, K. N. (2011) “Transmission electron microscopy of amyloid fibrils,” *Methods in Molecular Biology*. Humana Press, Totowa, NJ, 752, pp. 197–214. doi: 10.1007/978-1-60327-223-0_13.
43. Gravagnuolo, A. M. *et al.* (2016) “Class i Hydrophobin Vmh2 Adopts Atypical Mechanisms to Self-Assemble into Functional Amyloid Fibrils,” *Biomacromolecules*, 17(3), pp. 954–964.

BIBLIOGRAPHY

- doi: 10.1021/acs.biomac.5b01632.
44. Gustot, A. *et al.* (2015) “Amyloid fibrils are the molecular trigger of inflammation in Parkinson’s disease,” *Biochemical Journal*. Portland Press, 471(3), pp. 323–333. doi: 10.1042/BJ20150617.
45. Harrison, M. J. (2005) “SIGNALING IN THE ARBUSCULAR MYCORRHIZAL SYMBIOSIS,” *Annual Review of Microbiology*. Annual Reviews, 59(1), pp. 19–42. doi: 10.1146/annurev.micro.58.030603.123749.
46. Hawksworth, D. L. and Lücking, R. (2017) “Fungal Diversity Revisited: 2.2 to 3.8 Million Species,” in *The Fungal Kingdom*. American Society of Microbiology, pp. 79–95. doi: 10.1128/microbiolspec.funk-0052-2016.
47. Hess, W. M., Sassen, M. M. A. and Remsen, C. C. (1968) “Surface Characteristics of *Penicillium* Conidia,” *Mycologia*. Taylor & Francis, 60(2), p. 290. doi: 10.2307/3757159.
48. Hess, W. M. W. and Stocks, D. D. L. (1969) “Surface characteristics of *Aspergillus* conidia,” *Mycologia*. Taylor & Francis, 61(3), pp. 560–571. doi: 10.2307/3757245.
49. Iñaki Guijarro, J. *et al.* (1998) “Amyloid fibril formation by an SH3 domain,” *Proceedings of the National Academy of Sciences of the United States of America*. National Academy of Sciences, 95(8), pp. 4224–4228. doi: 10.1073/pnas.95.8.4224.
50. Jensen, B. G. *et al.* (2010) “Hydrophobins from *Aspergillus* species cannot be clearly divided into two classes,” *BMC Research Notes*, p. 344. doi: 10.1186/1756-0500-3-344.
51. Juárez, J., Taboada, P. and Mosquera, V. (2009) “Existence of different structural intermediates on the fibrillation pathway of human serum albumin,” *Biophysical Journal*. Cell Press, 96(6), pp. 2353–2370. doi: 10.1016/j.bpj.2008.12.3901.
52. Kendrick, B. (2001) “Fungi: Ecological Importance and Impact on Humans,” in *eLS*. Chichester, UK: John Wiley & Sons, Ltd. doi: 10.1038/npg.els.0000369.
53. Knowles, T. P. *et al.* (2007) “Role of intermolecular forces in defining material properties of

BIBLIOGRAPHY

- protein nanofibrils,” *Science*. American Association for the Advancement of Science, 318(5858), pp. 1900–1903. doi: 10.1126/science.1150057.
54. Kordts, M. *et al.* (2018) “Structure Formation in Class I and Class II Hydrophobins at the Air–Water Interface under Multiple Compression/Expansion Cycles,” *ChemistryOpen*. John Wiley & Sons, Ltd, 7(12), pp. 1005–1013. doi: 10.1002/open.201800176.
55. Krappmann, S. (2016) “How to invade a susceptible host: cellular aspects of aspergillosis,” *Current Opinion in Microbiology*. Elsevier Current Trends, pp. 136–146. doi: 10.1016/j.mib.2016.10.002.
56. Kwan, A. H. Y. *et al.* (2006) “Structural basis for rodlet assembly in fungal hydrophobins,” *Proceedings of the National Academy of Sciences*, 103(10), pp. 3621–3626. doi: 10.1073/pnas.0505704103.
57. Kwon-Chung, K. J. and Sugui, J. A. (2013) “*Aspergillus fumigatus*—What Makes the Species a Ubiquitous Human Fungal Pathogen?,” *PLoS Pathogens*. Public Library of Science, 9(12), p. e1003743. doi: 10.1371/journal.ppat.1003743.
58. Kyte, J. and Doolittle, R. F. (1982) “A simple method for displaying the hydropathic character of a protein,” *Journal of Molecular Biology*. Academic Press, 157(1), pp. 105–132. doi: 10.1016/0022-2836(82)90515-0.
59. Landreh, M. *et al.* (2016) “The formation, function and regulation of amyloids: insights from structural biology,” *Journal of Internal Medicine*, pp. 164–176. doi: 10.1111/joim.12500.
60. Langfelder, K. *et al.* (2003) “Biosynthesis of fungal melanins and their importance for human pathogenic fungi,” *Fungal Genetics and Biology*. Academic Press, pp. 143–158. doi: 10.1016/S1087-1845(02)00526-1.
61. Latgé, J.-P., Beauvais, A. and Chamilos, G. (2017) “The Cell Wall of the Human Fungal Pathogen *Aspergillus fumigatus*: Biosynthesis, Organization, Immune Response, and Virulence,” *Annual Review of Microbiology*. Annual Reviews, 71(1), pp. 99–116. doi:

BIBLIOGRAPHY

- 10.1146/annurev-micro-030117-020406.
62. Latgé, J.-P. P. (1999) “Aspergillus fumigatus and aspergillosis,” *Clinical microbiology reviews*. American Society for Microbiology Journals, 12(2), pp. 310–350. doi: 10.1128/CMR.12.2.310.
63. Latgé, J. -P. (2017) “30 years of battling the cell wall,” in *Medical Mycology*. Narnia, pp. 4–9. doi: 10.1093/mmy/myw076.
64. Latgé, J. -P. and Beauvais, A. (2014) “Functional duality of the cell wall,” *Current Opinion in Microbiology*. Elsevier Current Trends, pp. 111–117. doi: 10.1016/j.mib.2014.05.009.
65. Littlejohn, K. A., Hooley, P. and Cox, P. W. (2012) “Bioinformatics predicts diverse Aspergillus hydrophobins with novel properties,” *Food Hydrocolloids*, 27(2), pp. 503–516. doi: 10.1016/j.foodhyd.2011.08.018.
66. Lo, V. C. *et al.* (2014) “Fungal Hydrophobin Proteins Produce Self-Assembling Protein Films with Diverse Structure and Chemical Stability,” *Nanomaterials*. Multidisciplinary Digital Publishing Institute, 4(3), pp. 827–843. doi: 10.3390/nano4030827.
67. Lonescu-Zanetti, C. *et al.* (1999) “Monitoring the assembly of Ig light-chain amyloid fibrils by atomic force microscopy,” *Proceedings of the National Academy of Sciences of the United States of America*. National Academy of Sciences, 96(23), pp. 13175–13179. doi: 10.1073/pnas.96.23.13175.
68. Loquet, A. *et al.* (2018) “3D structure determination of amyloid fibrils using solid-state NMR spectroscopy,” *Methods*. doi: 10.1016/j.ymeth.2018.03.014.
69. Lugones, L. G. *et al.* (1996) “An abundant hydrophobin (ABH1) forms hydrophobic rodlet layers in *Agaricus bisporus* fruiting bodies,” *Microbiology*, 142(5), pp. 1321–1329. doi: 10.1099/13500872-142-5-1321.
70. Macindoe, I. *et al.* (2012) “Self-assembly of functional, amphipathic amyloid monolayers by the fungal hydrophobin EAS,” *Proceedings of the National Academy of Sciences of the United*

BIBLIOGRAPHY

- States of America*, 109(14), pp. E804–E811. doi: 10.1073/pnas.1114052109.
71. Maji, S. K. *et al.* (2009) “Functional Amyloids As Natural Storage of Peptide Hormones in Pituitary Secretory Granules,” *Science*, 325(5938), pp. 328–332. doi: 10.1126/science.1173155.
72. Mankar, S. *et al.* (2011) “Nanomaterials: amyloids reflect their brighter side,” *Nano Reviews*. Taylor & Francis, 2(1), p. 6032. doi: 10.3402/nano.v2i0.6032.
73. de Marco, A. (2009) “Strategies for successful recombinant expression of disulfide bond-dependent proteins in *Escherichia coli*,” *Microbial Cell Factories*, p. 26. doi: 10.1186/1475-2859-8-26.
74. Margalit, A. and Kavanagh, K. (2015) “The innate immune response to *Aspergillus fumigatus* at the alveolar surface,” *FEMS Microbiology Reviews*. Edited by G. Braus. Narnia, pp. 670–687. doi: 10.1093/femsre/fuv018.
75. Meisl, G. *et al.* (2016) *Molecular mechanisms of protein aggregation from global fitting of kinetic models*, *Nature Protocols*. Nature Research. doi: 10.1038/nprot.2016.010.
76. Micsonai, A. *et al.* (2015) “Accurate secondary structure prediction and fold recognition for circular dichroism spectroscopy,” *Proceedings of the National Academy of Sciences of the United States of America*, 112(24), pp. E3095-103. doi: 10.1073/pnas.1500851112.
77. Money, N. P. (2001) “Biomechanics of Invasive Hyphal Growth,” in *Biology of the Fungal Cell*. Berlin, Heidelberg: Springer Berlin Heidelberg, pp. 3–17. doi: 10.1007/978-3-662-06101-5_1.
78. Morris, V. K. *et al.* (2011) “Recruitment of class I hydrophobins to the air:Water interface initiates a multi-step process of functional amyloid formation,” *Journal of Biological Chemistry*. American Society for Biochemistry and Molecular Biology, 286(18), pp. 15955–15963. doi: 10.1074/jbc.M110.214197.
79. Morris, V. K., Kwan, A. H. and Sunde, M. (2013) “Analysis of the structure and

BIBLIOGRAPHY

- conformational states of DewA gives insight into the assembly of the fungal hydrophobins,” *Journal of Molecular Biology*. Academic Press, 425(2), pp. 244–256. doi: 10.1016/j.jmb.2012.10.021.
80. Nelson, R. *et al.* (2005) “Structure of the cross- β spine of amyloid-like fibrils,” *Nature*. NIH Public Access, 435(7043), pp. 773–778. doi: 10.1038/nature03680.
81. Otzen, D. and Riek, R. (2019) “Functional Amyloids,” *Cold Spring Harbor Perspectives in Biology*, p. a033860. doi: 10.1101/cshperspect.a033860.
82. Pace, C. N. *et al.* (1995) “How to measure and predict the molar absorption coefficient of a protein,” *Protein Science*. John Wiley & Sons, Ltd, 4(11), pp. 2411–2423. doi: 10.1002/pro.5560041120.
83. Paris, S. *et al.* (2003) “Conidial hydrophobins of *Aspergillus fumigatus*,” *Applied and Environmental Microbiology*. American Society for Microbiology, 69(3), pp. 1581–1588. doi: 10.1128/AEM.69.3.1581-1588.2003.
84. Pham, C. L. L. *et al.* (2016) “Self-assembly of MPG1, a hydrophobin protein from the rice blast fungus that forms functional amyloid coatings, occurs by a surface-driven mechanism,” *Scientific Reports*, 6(April), p. 25288. doi: 10.1038/srep25288.
85. Pham, C. L. L. *et al.* (2018) “Probing Structural Changes during Self-assembly of Surface-Active Hydrophobin Proteins that Form Functional Amyloids in Fungi,” *Journal of Molecular Biology*, 430(20), pp. 3784–3801. doi: 10.1016/j.jmb.2018.07.025.
86. Pham, C. L. L., Kwan, A. H. and Sunde, M. (2014) “Functional amyloid: widespread in Nature, diverse in purpose,” *Essays In Biochemistry*. Portland Press Limited, 56, pp. 207–219. doi: 10.1042/bse0560207.
87. Pille, A. *et al.* (2015) “ ^1H , ^{13}C and ^{15}N resonance assignments of the RodA hydrophobin from the opportunistic pathogen *Aspergillus fumigatus*,” *Biomolecular NMR Assignments*, 9(1), pp. 113–118. doi: 10.1007/s12104-014-9555-1.

BIBLIOGRAPHY

88. Prusiner, S. B. (1998) “Nobel Lecture: Prions,” *Proceedings of the National Academy of Sciences*. National Academy of Sciences, 95(23), pp. 13363–13383. doi: 10.1073/pnas.95.23.13363.
89. Radamaker, L. *et al.* (2019) “Cryo-EM structure of a light chain-derived amyloid fibril from a patient with systemic AL amyloidosis,” *Nature Communications*. Nature Publishing Group, 10(1), p. 1103. doi: 10.1038/s41467-019-09032-0.
90. Röder, C. *et al.* (2019) “Atomic structure of PI3-kinase SH3 amyloid fibrils by cryo-electron microscopy,” *Nature Communications*. Nature Publishing Group, 10(1), p. 3754. doi: 10.1038/s41467-019-11320-8.
91. Sarroukh, R. *et al.* (2013) “ATR-FTIR: A ‘rejuvenated’ tool to investigate amyloid proteins,” *Biochimica et Biophysica Acta - Biomembranes*, 1828(10), pp. 2328–2338. doi: 10.1016/j.bbamem.2013.04.012.
92. Sawaya, M. R. *et al.* (2007) “Atomic structures of amyloid cross- β spines reveal varied steric zippers,” *Nature*. Nature Publishing Group, 447(7143), pp. 453–457. doi: 10.1038/nature05695.
93. Scheele, B. C. *et al.* (2019) “Amphibian fungal panzootic causes catastrophic and ongoing loss of biodiversity,” *Science*, 363(6434), pp. 1459–1463. doi: 10.1126/science.aav0379.
94. De Simone, A. *et al.* (2012) “Intrinsic disorder modulates protein self-assembly and aggregation,” *Proceedings of the National Academy of Sciences*. National Academy of Sciences, 109(18), pp. 6951–6956. doi: 10.1073/pnas.1118048109.
95. Sipe, J. D. (1992) “Amyloidosis and the acute phase response.,” *Folia histochemica et cytobiologica / Polish Academy of Sciences, Polish Histochemical and Cytochemical Society*. Annual Reviews 4139 El Camino Way, P.O. Box 10139, Palo Alto, CA 94303-0139, USA, pp. 171–173. doi: 10.1146/annurev.bi.61.070192.004503.
96. Speth, C. *et al.* (2019) “Galactosaminogalactan (GAG) and its multiple roles in *Aspergillus*

BIBLIOGRAPHY

- pathogenesis,” *Virulence*. Taylor & Francis, pp. 1–8. doi: 10.1080/21505594.2019.1568174.
97. Stefani, M. and Dobson, C. M. (2003) “Protein aggregation and aggregate toxicity: New insights into protein folding, misfolding diseases and biological evolution,” *Journal of Molecular Medicine*. Springer-Verlag, pp. 678–699. doi: 10.1007/s00109-003-0464-5.
98. Sunde, M., Pham, C. L. L. and Kwan, A. H. (2017) “Molecular Characteristics and Biological Functions of Surface-Active and Surfactant Proteins,” *Annual Review of Biochemistry*. Annual Reviews, 86(1), pp. 585–608. doi: 10.1146/annurev-biochem-061516-044847.
99. Thau, N. *et al.* (1994) “rodletless mutants of *Aspergillus fumigatus*,” *Infection and immunity*. American Society for Microbiology Journals, 62(10), pp. 4380–8. Available at: <http://www.ncbi.nlm.nih.gov/pubmed/7927699> (Accessed: October 8, 2019).
100. Thompson, J. D., Higgins, D. G. and Gibson, T. J. (1994) “CLUSTAL W: Improving the sensitivity of progressive multiple sequence alignment through sequence weighting, position-specific gap penalties and weight matrix choice,” *Nucleic Acids Research*, 22(22), pp. 4673–4680. doi: 10.1093/nar/22.22.4673.
101. Törnquist, M. *et al.* (2018) “Secondary nucleation in amyloid formation,” *Chemical Communications*. Royal Society of Chemistry, 54(63), pp. 8667–8684. doi: 10.1039/c8cc02204f.
102. Tsolis, A. C. *et al.* (2013) “A Consensus Method for the Prediction of ‘Aggregation-Prone’ Peptides in Globular Proteins,” *PLoS ONE*. Public Library of Science, 8(1). doi: 10.1371/journal.pone.0054175.
103. Tudela, J. L. R. and Denning, D. W. (2017) “Recovery from serious fungal infections should be realisable for everyone,” *The Lancet Infectious Diseases*. Elsevier, 17(11), pp. 1111–1113. doi: 10.1016/s1473-3099(17)30319-5.
104. Tycko, R. (2015) “Amyloid Polymorphism: Structural Basis and Neurobiological Relevance,” *Neuron*. NIH Public Access, pp. 632–645. doi: 10.1016/j.neuron.2015.03.017.

BIBLIOGRAPHY

105. Vahabi, S., Nazemi Salman, B. and Javanmard, A. (2013) "Atomic force microscopy application in biological research: a review study.," *Iranian journal of medical sciences*. Shiraz University of Medical Sciences, 38(2), pp. 76–83. Available at: <http://www.ncbi.nlm.nih.gov/pubmed/23825885> (Accessed: September 2, 2019).
106. Valsecchi, I. *et al.* (2018) "Role of Hydrophobins in *Aspergillus fumigatus*," *Journal of Fungi*. Multidisciplinary Digital Publishing Institute, 4(1), p. 2. doi: 10.3390/jof4010002.
107. Valsecchi, I., Dupres, V., *et al.* (2019a) "The puzzling construction of the conidial outer layer of *Aspergillus fumigatus*," *Cellular Microbiology*. John Wiley & Sons, Ltd (10.1111), 21(5), p. e12994. doi: 10.1111/cmi.12994.
108. Valsecchi, I., Lai, J. I., *et al.* (2019b) "Assembly and disassembly of *Aspergillus fumigatus* conidial rodlets," *The Cell Surface*. Elsevier, 5, p. 100023. doi: 10.1016/j.tcs.2019.100023.
109. de Vocht, M. L. *et al.* (2002) "Self-assembly of the hydrophobin SC3 proceeds via two structural intermediates," *Protein Science*. Wiley-Blackwell, 11(5), pp. 1199–1205. doi: 10.1110/ps.4540102.
110. De Vocht, M. L. *et al.* (2000) "Structural and functional role of the disulfide bridges in the hydrophobin SC3," *Journal of Biological Chemistry*. American Society for Biochemistry and Molecular Biology, 275(37), pp. 28428–28432. doi: 10.1074/jbc.M000691200.
111. Vranken, W. F. *et al.* (2005) "The CCPN data model for NMR spectroscopy: Development of a software pipeline," *Proteins: Structure, Function and Genetics*. John Wiley & Sons, Ltd, 59(4), pp. 687–696. doi: 10.1002/prot.20449.
112. Wallace, B. a (2009) "Protein characterisation by synchrotron radiation circular dichroism spectroscopy.," *Quarterly reviews of biophysics*, 42(4), pp. 317–370. doi: 10.1017/S003358351000003X.
113. Wang, J. (2004) "The complex kinetics of protein folding in wide temperature ranges,"

BIBLIOGRAPHY

- Biophysical Journal*. The Biophysical Society, 87(4), pp. 2164–2171. doi: 10.1529/biophysj.104.042812.
114. Wang, X. *et al.* (2004) “Probing the self-assembly and the accompanying structural changes of hydrophobin SC3 on a hydrophobic surface by spectrometry,” *Biophysical Journal*, 87(3), pp. 1919–1928. doi: 10.1529/biophysj.104.041616.
115. Wessels, J. *et al.* (1991) “Hydrophobin Genes Involved in Formation of Aerial Hyphae and Fruit Bodies in *Schizophyllum*,” *The Plant cell*. American Society of Plant Biologists, 3(8), pp. 793–799. doi: 10.1105/tpc.3.8.793.
116. Wessels, J. G. H. (2000) “Hydrophobins, unique fungal proteins,” *Mycologist*. Edited by J. Heitman. Public Library of Science, 14(4), pp. 153–159. doi: 10.1016/S0269-915X(00)80030-0.
117. Wessels, J. J. G. H. J. *et al.* (1991) “Hydrophobin Genes Involved in Formation of Aerial Hyphae and Fruit Bodies in *Schizophyllum*,” *The Plant Cell*. American Society of Plant Biologists, 3(8), p. 793. doi: 10.1105/tpc.3.8.793.
118. Willger, S., Grahl, N. and Cramer, R. A. (2009) “*Aspergillus fumigatus* metabolism: Clues to mechanisms of in vivo fungal growth and virulence,” *Medical Mycology*. NIH Public Access, pp. S72-9. doi: 10.1080/13693780802455313.
119. Winandy, L., Schlebusch, O. and Fischer, R. (2019) “Fungal hydrophobins render stones impermeable for water but keep them permeable for vapor,” *Scientific Reports*. Nature Publishing Group, 9(1), p. 6264. doi: 10.1038/s41598-019-42705-w.
120. Wösten, H. A. B. (2001) “Hydrophobins: Multipurpose Proteins,” *Annual Review of Microbiology*. Annual Reviews 4139 El Camino Way, P.O. Box 10139, Palo Alto, CA 94303-0139, USA, 55(1), pp. 625–646. doi: 10.1146/annurev.micro.55.1.625.
121. Xue, C. *et al.* (2017) “Thioflavin T as an amyloid dye: fibril quantification, optimal concentration and effect on aggregation,” *Royal Society open science*. The Royal Society,

BIBLIOGRAPHY

4(1), p. 160696. doi: 10.1098/rsos.160696.

122. Zykwinska, A. *et al.* (2014) “Spontaneous self-assembly of SC3 hydrophobins into nanorods in aqueous solution,” *Biochimica et Biophysica Acta - Proteins and Proteomics*. Elsevier, 1844(7), pp. 1231–1237. doi: 10.1016/j.bbapap.2014.04.003.